SIGNAL PROCESSING APPLICATIONS FOR FIBER OPTIC LINKS

A Dissertation
Presented to
The Academic Faculty

by

Jerrod Scott Langston

In Partial Fulfillment
of the Requirements for the Degree
Doctor of Philosophy in
Electrical and Computer Engineering

Georgia Institute of Technology
December 2019

SIGNAL PROCESSING APPLICATIONS FOR FIBER OPTIC LINKS

Approved by:

Dr. Stephen E. Ralph, Advisor
School of Electrical and Computer Engineering
Georgia Institute of Technology

Dr. John R. Barry
School of Electrical and Computer Engineering
Georgia Institute of Technology

Dr. Matthieu Bloch
School of Electrical and Computer Engineering
Georgia Institute of Technology

Dr. Wenjing Liao
School of Mathematics
Georgia Institute of Technology

Dr. Richard DeSalvo
L3Harris Technologies

Date Approved: November 4, 2019

To my wife

ACKNOWLEDGEMENTS

Though this document has my name on the front page, this work comes out of the support, collaboration, investment, and patience of many individuals I am extremely grateful for.

First for Prof. Ralph, who first introduced me to the world of optics and photonics, an engaging field that was the unknown answer to what I was looking when coming to Georgia Tech. This world of optics is deep and wide, and over the course of six years, he has helped me see its breadth and detail, and yet there is so much more. I am thankful for his investment of time and resources into my education and research, and for prodding for the underpinning answers to questions that are important and yet so easily dismissed.

Second for my reading and defense committee: Prof. Matthieu Bloch, Dr. Richard DeSalvo, Prof. John R. Barry, and Prof. Wenjing Liao. I am grateful for the guidance in the later steps of this program. Particularly Prof. Bloch for insight into the broader scope of communications and Dr. DeSalvo into the practice and application of optics outside academia.

Third for my peers, who not only supported in the work and research, but also as friends: Jie Pan, Sriharsha Kota, Stuart Hughes, Daniel Haupt, Michael Pratt, Jon James, Daniel Lippiatt, Gareeyasee Saha, Christian Bottenfield, Daniel Garon, Alirio Melgar, and Hyung Joon Cho. I'm particularly thankful for Pierre Isautier who first "showed me the ropes" and subsequently Siddharth Varughese for many technical discussions. And Justin Lavrencik: though our research almost never crossed, our conversations, whether academic or not, often did.

Fourth for those in industry that further revealed the application and significance of this field of research as well as expertise in its practice. In this regard, I am particularly thankful for Sorin Tibuleac, Charles Middleton, Andy Stark, Micah Jenkins, Kristina Bagnell, Tony Klee, Thomas Richter, Ben Yang, and Mohammad Alfiad.

Finally, for my wife and best friend, Brittany Langston, who supported me through this all with much patience and forbearance. Without her, I truly would not have reached this point.

TABLE OF CONTENTS

ACKNOWLEDGEMENTS **iv**
LIST OF TABLES **viii**
LIST OF FIGURES **ix**
LIST OF ACRONYMS **xiv**
SUMMARY **xviii**
CHAPTER 1. INTRODUCTION **1**
1.1 Motivation **1**
1.2 Objective and Outline **1**
CHAPTER 2. BACKGROUND INFORMATION **4**
2.1 Modulation Formats and Shaping **4**
2.1.1 Single-carrier Formats 4
2.1.2 Multicarrier Formats 4
2.1.3 Time-domain Hybrid Modulation Formats 5
2.1.4 Probabilistic Shaping 6
2.1.5 Geometric Shaping 7
2.2 Fiber Optic Communication Links **7**
2.2.1 Fiber Transport Links 7
2.2.2 V-band RF Photonic Links 8
2.2.3 W-band RF Photonic Links 9
2.3 Fiber Link Impairments **10**
2.3.1 Linear Fiber Propagation Impairments 10
2.3.2 Receiver Noise 12
2.3.3 Non-resonant Nonlinear Processes 14
2.3.4 Laser Phase Noise 15
2.3.5 Electronics 16
2.4 DSP in Coherent Fiber Optic Links **17**
2.4.1 Matched Filtering 17
2.4.2 CD Compensation and Estimation 17
2.4.3 Timing Recovery 21
2.4.4 Polarization Demultiplexing 23
2.4.5 Frequency Offset Correction 25
2.4.6 Carrier Phase Recovery 26
2.4.7 Residual Equalization 27
2.5 Waveform Characterization **27**
2.5.1 Coherent Single-Carrier QAM and PSK Classification 27
2.5.2 Hybrid Format Classification 28
2.5.3 OFDM Classification 28
2.6 Cyclostationary Processing **29**
2.7 Cyclostationary Processors in Fiber Optic Links **29**
2.8 Cyclostationary Processing Applied to Fiber Optic Links **30**
CHAPTER 3. SINGLE-CARRIER BLIND CLASSIFICATION **32**
3.1 Cyclostationarity-Based Classification **32**

3.1.1 Higher-order cumulants 32
3.1.2 Architecture 33
3.1.3 Experimental Results 34
3.2 Adaptive Rate Classification 36
3.2.1 Architecture 36
3.2.2 Experimental Setup 48
3.2.3 Experimental Results 50
3.2.4 Comparison to Other Architectures 59
3.3 Nonlinear Compensator 60
3.3.1 Procedure 61
3.3.2 Experimental Results 63
CHAPTER 4. MULTI-CARRIER BLIND CLASSIFICATION 65
4.1 Architecture 65
4.1.1 Spectral Monitoring 66
4.1.2 Cyclostationarity Test 68
4.1.3 Constellation Classification 73
4.1.4 Demodulation 73
4.2 Experimental Setup 73
4.3 Experimental Results 74
CHAPTER 5. HIGH-SPEED FIBER-WIRELESS TRANSMISSION 78
5.1 V-band Fiber-Wireless 78
5.1.1 Experimental Setup 78
5.1.2 Experimental Results 78
5.2 W-band Fiber-Wireless 79
5.2.1 Experimental Setup 79
5.2.2 Experimental Results 80
5.2.3 Discussion 84
CHAPTER 6. OPTICAL CYCLOSTATIONARY PROCESSOR 85
6.1 Optical Conjugate Multiplication Theory 85
6.1.1 Conjugate multiplication via Coherent Receiver 85
6.1.2 Conjugate multiplication via Cascaded ModulaTors 87
6.1.3 Conjugate Multiplication Via Four-Wave Mixing 87
6.2 OCSP with Direct Detection 89
6.2.1 Architecture and Operation 89
6.2.2 Experimental Results 91
6.2.3 Discussion 91
6.3 OCSP With Coherent Detection 92
6.3.1 Architecture and Operation 92
6.3.2 Experimental Results 96
6.3.3 Discussion 104
CHAPTER 7. CONCLUSIONS 105
7.1 Future research topics 106

LIST OF TABLES

Table 1	Normalized cyclic spectra evaluated at the baud rate of different pulse shapes	40
Table 2	Experimental setup parameters for adaptive rate classification	49
Table 3	Confusion matrix after back-to-back transmission	53
Table 4	Confusion matrix after 90-km transmission	55
Table 5	Confusion matrix after 810-km transmission	56
Table 6	Modulation parameters of OFDM waveforms	82
Table 7	Signal parameters for FDM 16QAM SCF evaluation	100
Table 8	Signal parameters for 5G waveform SCF evaluation	102

LIST OF FIGURES

Fig. 1	Block diagram of OFDM generation and demodulation.	5
Fig. 2	Structure of hybrid QAM comprised of QPSK(1)-8QAM(1).	6
Fig. 3	Example distribution of probabilistically shaped 64QAM, which has a spectral efficiency of 5.5.	6
Fig. 4	Block diagram of long-haul fiber optic test-bed	8
Fig. 5	Block diagram of fiber optic demodulation architecture	17
Fig. 6	Cyclostationarity-based QAM format classification architecture	34
Fig. 7	HOCC-based classification thresholds and accuracy for 0-km	35
Fig. 8	HOCC-based classification thresholds and accuracy for 180-km	35
Fig. 9	Block diagram of the classification architecture. Blue blocks correspond to DSP demodulation blocks, whereas purple blocks correspond to parameter estimation blocks. Inputs and outputs are complex.	37
Fig. 10	Theoretical normalized cyclic spectra evaluated at the baud rate of different pulse shapes, with cyclic frequency normalized to the baud rate. RC and RRC pulse shapes shown have a roll-off factor of 0.3.	41
Fig. 11	Constellations investigated: (a) square-64QAM ($\boldsymbol{p = 4}$), (b) hex-64QAM ($\boldsymbol{p = 12}$), and (c) circle-64QAM ($\boldsymbol{p = 8}$). Voronoi boundaries shown in red, corresponding to the optimal decision boundaries in an AWGN channel.	45
Fig. 12	a) Example of *k*-means clustering with different number of clusters for a simulated 16QAM constellation and (b) associated classification criterions normalized to 1. The CH index peaks at the correct cluster size, unlike the other cluster variance parameters.	47
Fig. 13	Block diagram of experimental setup with recirculating loop. Red traces are optical and blue traces are electrical.	49
Fig. 14	Experimental pulse shape roll-off estimation of 32-Gbd DP-64QAM after 90-km transmission. (a) RC and (b) RRC transmitted pulse shaping. Dotted traces correspond to the	51

median estimate for 50-GHz channel filtering and solid traces for 100-GHz channel filtering. Estimate points also shown. All traces are at 20-dB OSNR.

Fig. 15 Classification accuracy of rotational symmetry order for various formats and constellation shapes after back-to-back transmission. All formats and shapes perfectly classified, except for hex-64QAM. 52

Fig. 16 Performance of TD-HMF classification after back-to-back transmission. 52

Fig. 17 Classification error (with 95% confidence Wilson score intervals) for back-to-back transmission of 32-Gbd QAM formats, from large waveform set experiment. 54

Fig. 18 Performance of TD-HMF classification after 90-km transmission. QPSK is nearly 1 for OSNRs greater than 12-dB. 55

Fig. 19 Performance of QAM classification after 810-km transmission. 56

Fig. 20 Performance of constellation shape estimation of DP-64QAM after back-to-back (solid traces) and 90-km (dashed traces) transmission, characterized by the median of the mean square error of the constellation estimate. The median is calculated from 10 constellation estimates. 58

Fig. 21 Performance of bit rate estimation after 90-km transmission. Dotted traces correspond to transmitted bit rate and solid traces correspond to estimated bit rate. The transmitted bit rate is constant with respect to OSNR. 59

Fig. 22 Block diagram of receiver-side DSP with equalizer that includes a complex least-mean square Hammerstein equalizer. 62

Fig. 23 Block diagram of nonlinearity compensator with joint I-Q linearization including even and odd terms. 62

Fig. 24 16-Gbd DP-64QAM output constellation after linear equalization (left) and NLC (right), where OSNR = 39 dB. 64

Fig. 25 BER performance of 16-Gbd DP-64QAM with nonlinear compensator 64

Fig. 26 High-level block diagram of blind OFDM demodulator. 66

Fig. 27	Output of spectral monitoring block for 3-Gbd OFDM at a 3-GHz IF	68
Fig. 28	Block diagram of CS test	68
Fig. 29	Synthesis of an CP-OFDM symbol	69
Fig. 30	Ideal projections of the CAF of CP-OFDM without preambles	70
Fig. 31	Structure of OFDM-CP (a) frame and (b) preamble	71
Fig. 32	Ideal projections of the CAF of CP-OFDM with preambles	72
Fig. 33	Experimental setup of wireless photonic link to demonstrate OFDM classification capabilities.	74
Fig. 34	Probability of correct classification of the number of subcarriers for 3-Gbd QPSK-OFDM with a CP length of 8 symbols	75
Fig. 35	Probability of correct classification of the cyclic prefix length of 3-Gbd QPSK CP-OFDM waveform with $N = 256$	75
Fig. 36	Probability of correct classification of the baud rate of 3-Gbd QPSK CP-OFDM waveform with $N = 256$ and $N_{CP} = 8$	76
Fig. 37	Probability of correct classification of the preamble duty cycle of 3-Gbd QPSK CP-OFDM waveform with $N = 256$, $N_{CP} = 8$, and Schmidl preamble	77
Fig. 38	Block diagram of single-polarization V-band photonic wireless link for OFDM transmission. Red elements are optical components and blue elements are electrical components.	78
Fig. 39	Performance of bit-loaded 21-Gbd OFDM, for 76.915-Gbps transmission.	79
Fig. 40	Experimental of W-band fiber-wireless transmission, with electrical downconversion.	80
Fig. 41	Measured (a) spectrum and (b) constellation after W-band fiber-wireless transmission of 24-Gbd QPSK.	81
Fig. 42	Measured (a) spectrum and (b) constellation after W-band fiber-wireless transmission of 16-Gbd 16QAM.	81
Fig. 43	26-Gbd OFDM QPSK with net data rate of 43.3-Gbps. a) EVM for each subcarrier and b) aggregate constellation.	83

Fig. 44	16-Gbd OFDM QPSK with net data rate of 57.8-Gbps. a) EVM for each subcarrier and b) aggregate constellation.	83
Fig. 45	26-Gbd bit-loaded OFDM with net data rate of 73.5-Gbps. a) EVM for each subcarrier and b) aggregate constellation.26-Gbd bit-loaded OFDM with net data rate of 73.5-Gbps. a) EVM for each subcarrier and b) aggregate constellation.	84
Fig. 46	General structure of a CSP. The CSP implemented in this work has blue blocks performed digitally, red performed optically, and red-blue a combination of the two.	85
Fig. 47	Single-polarization coherent receiver with intermediate fields and current.	86
Fig. 48	Cartoon showing the interacting fields of interest when FWM.	89
Fig. 49	Block diagram of OCSP-DD.	89
Fig. 50	Experimentally measured optical spectra at output of HNLF.	90
Fig. 51	CS processor output averaged and mapped to generate the square of the SCF. Input signal: 50-Mbd QPSK on a 50-MHz carrier.	91
Fig. 52	Block diagram of OCSP-CD.	93
Fig. 53	Measured spectra at different locations in the OCSP-CD. a) Generated tones at output of PM, b) filter PM output used as LO for coherent detection, c) combined modulated signals, d) EDFA tap before input to HNLF, e) FWM term selected by OBPF, and f) digitized signal.	95
Fig. 54	Structure of signals modulated onto OCSP-CD optical carriers	96
Fig. 55	Two-tone output (measuring the fundamental mixing tone)	97
Fig. 56	Measured PSD and phase of 15Gbd 16QAM with RRC 0.5-roll-off pulse shaping, with different number of averaged waveforms	98
Fig. 57	Measured cyclic spectrum at the baud rate of 15Gbd 16QAM with RRC 0.5-roll-off pulse shaping, with different number of averaged waveforms	98
Fig. 58	Measured cyclic spectrum of 15Gbd 16QAM with RRC 0.5-roll-off pulse shaping, with different number of averaged waveforms (with cyclic frequency of 14.766-GHz)	99

Fig. 59	Measured SCF of 15Gbd 16QAM with RRC 0.5-roll-off pulse shaping	99
Fig. 60	Measured SCF of FDM 16QAM signals	101
Fig. 61	Measured SCF of 5G signals with time-stretching	102
Fig. 62	Average magnitude of SCF, displaying peaks at zero cyclic frequency and baud rate cyclic frequency	103
Fig. 63	RRC regression of measured cyclic spectrum	104

LIST OF ACRONYMS

ABC	Automatic bias controller
ADC	Analog-to-digital converter
ASE	Amplified spontaneous emission
AWG	Arbitrary waveform generator (or arrayed waveguide)
AWGN	Additive white Gaussian noise
B2B	Back-to-back
BER	Bit error ratio
CAF	Cyclic autocorrelation function
CD	Chromatic dispersion (or coherent detection)
CFO	Carrier frequency offset
CH	Calinski-Harabasz
CMA	Constant modulus algorithm
CP	Cyclic prefix
CPR	Carrier phase recovery
CS	Cyclostationary
CSP	Cyclostationary processor
DAC	Digital-to-analog converter
DD	Decision-directed (or direct detection)
DFB	Distributed-feedback
DFE	Decision feedback equalizer
DFT	Discrete Fourier transform
DMT	Discrete multi-tone

DP	Dual polarization
DSB	Double side-band
DSP	Digital signal processing
ECL	External cavity laser
EDFA	Erbium doped fiber amplifier
ENOB	Effective number of bits
EVM	Error vector magnitude
FD	Frequency domain
FDM	Frequency division multiplexing
FFT	Fast Fourier transform
FIR	Finite impulse response
FM	Frequency modulation
FWM	Four wave mixing
GMM	Gaussian mixture model
HNLF	Highly nonlinear fiber
HOC	Higher-order cumulants
HOCC	Higher-order cyclic cumulants
ICA	Independent component analysis
IF	Intermediate frequency
ISI	Inter-symbol interference
LMS	Least-mean square
LO	Local oscillator
MIMO	Multiple-input multiple-output
MMA	Multiple-modulus algorithm
MSE	Mean-square error

MZM	Mach-Zehnder modulator
NLC	Nonlinear compensator
OBPF	Optical bandpass filter
OCSP	Optical cyclostationary processor
OFDM	Orthogonal frequency division multiplexing
OSNR	Optical signal-to-noise ratio
PAM	Pulse amplitude modulation
PAPR	Peak-to-average-power ratio
PC	Polarization controller
PCA	Principal component analysis
PD	Photodiode (or photodetector)
PM	Polarization maintaining (or phase modulator)
PMD	Polarization mode dispersion
PS	Probabilistic shaping
PSD	Power spectral density
QAM	Quadrature amplitude modulation
QPSK	Quadrature phase shift keying
RBF	Radial basis function
RC	Raised cosine
RF	Radio frequency
RRC	Root raised cosine
SCF	Spectral correlation function
SDM	Spacial division multiplexing
SE	Spectral efficiency
SINAD	Signal-to-interference-noise-and-distortion

SNR	Signal-to-noise ratio
SPM	Self-phase modulation
SSB	Single side-band
SSMF	Standard single-mode fiber
SVM	Support vector machine
TD-HMF	Time-domain hybrid modulation format
TIA	Transimpedance amplifier
VOA	Variable optical attenuator (or amplifier)
VODL	Variable optical delay line
WDM	Wavelength division multiplexing
WSS	Wavelength selective switch
XPM (CPM)	Cross-phase modulation

SUMMARY

The objective of the research is to utilize photonic technology for high bandwidth cyclostationary processing and high data rate fiber-wireless transmission, and to develop blind receiver signal processing for flexible optical networks.

CHAPTER 1. INTRODUCTION

1.1 Motivation

Due to increasing data demands, the achievable capacity of long-haul and metro fiber networks is ever increasing with 400-Gb/s per wavelength being currently deployed and 600-Gb/s and further a topic of present research. In addition to these higher data rates, reconfigurable optical networks are becoming more flexible and transparent to modulation parameters, to address dynamic network impairments and variable bandwidth requirements.

With the emergence of reconfigurable networks, a means of communicating the changing modulation parameters must be employed. Smart receivers are capable of bypassing this communication and determining the parameters adaptively. But as long-haul links encroach on the fiber capacity limits, more complex modulation schemes are utilized and, thus, require increasingly robust receivers. Most smart receivers depend on digital signal processing and machine learning techniques, photonic signal processing can offer an alternative approach with higher-bandwidth processing capabilities.

1.2 Objective and Outline

This dissertation focuses on the use of signal processing, both digital and optical, for robust signal identification and adaptive impairment correction in coherent optical links. The objective of this research is multi-pronged. First, to develop and validate a blind architecture for the classification of practical coherent waveforms for 100G to 400G links, which requires the consideration of 64QAM formats, time-domain hybrid modulation formats, probabilistic shaping, and constellation shaping. Second, to develop and validate

a blind architecture for OFDM waveforms transmitted over fiber-wireless links. Third, to demonstrate and investigate the utilization of hybrid fiber-wireless systems for high-bandwidth wireless transmission and low loss fiber remoting, using single- and multi-carrier modulation formats. Fourth, develop and validate an optical cyclostationary processor using nonlinear optical signal processing to evaluate the spectral correlation function of wide bandwidth waveforms.

An outline of the dissertation is described as follows. Chapter 2 covers background information on general digital communication schemes, fiber optic communication links, theory of fiber link impairments, conventional coherent demodulation DSP, state of the art blind waveform classification methods, and cyclostationary processing in the digital and optical domain.

Chapter 3 presents blind waveform classification architectures for single-carrier modulation formats transmitted over coherent optical links. The first architecture utilizes higher-order cyclic cumulants for the classification of high-baud rate QPSK, 16QAM, and 64QAM over coherent links, whereas the latter is a highly flexible architecture that enables characterization of adaptive rate formats comprised of constellation shaping, probabilistic shaping, and time-division hybrid modulation formats transmitted over coherent links. Also, presented is a nonlinear compensator to correct for compression of higher-order modulation formats in coherent links with increased nonlinearities.

Chapter 4 presents a cyclostationarity-based architecture for OFDM waveform characterization and its experimental demonstration for OFDM signals over a K_a-band

fiber-wireless link. Chapter 5 discusses experimental results of high-speed wireless transmission over V- and W-band links utilizing hybrid fiber-wireless technology.

Chapter 6 presents a novel optical cyclostationary processor for evaluating the spectral correlation function of wide-bandwidth waveform, exploiting conjugate multiplication via four wave mixing. Two architectures are experimentally demonstrated with direct- and coherent-detection, respectively, and operation is validated for various mixtures of waveforms and modulation parameters. Chapter 7 provides a conclusion of the work presented here and suggests research areas to be pursued in the future.

CHAPTER 2. BACKGROUND INFORMATION

2.1 Modulation Formats and Shaping

Modulation is the process of mapping a sequence of data to a signal suitable for transmission over a channel. Here we consider digital modulation formats where the sequence of data is comprised of bits. The modulated waveform should match the characteristics of the communication channel (e.g. frequency response) for optimal data transmission.

2.1.1 Single-carrier Formats

Single-carrier formats are the most straightforward modulation schemes, wherein (primarily) the amplitude or phase is modulated directly onto the carrier. In pulse amplitude modulation (PAM), digital information is represented as a stream of pulses with different amplitudes [1]. In many applications (particularly for fiber-optic links) double-sideband (DSB) PAM is employed due to simplicity, but single-sideband (SSB) PAM can be implemented in order to utilize the channel bandwidth more efficiently (one-half that of DSB-PAM). Quadrature amplitude modulation (QAM) doubles the spectral efficiency of DSB-PAM by modulating two information streams on two orthogonal carriers, $\cos 2\pi f_c t$ and $\sin 2\pi f_c t$, and is the most commonly employed format in long-haul fiber-optic links. Phase shift keying (PSK) represents symbols by the phase of the carrier.

2.1.2 Multicarrier Formats

Multicarrier formats attempt to more closely match the characteristics of the channel by considering the communication channel as a number of sub-channels. The capacity of the overall channel is the combined capacity of the individual sub-channels, as

the bandwidth of the sub-channels approaches zero. By optimizing the waveform transmitted over each sub-channel, the data rate of the overall waveform can be maximized. Water-filling [2] addresses this optimization by transmitting the highest power within the highest SNR sub-channels, and the lowest SNR within the lowest SNR sub-channel.

Orthogonal frequency division multiplexing (OFDM) is the most widely used multicarrier format [3]. Data symbols (e.g. QAM symbols) are mapped to orthogonal subcarriers via the discrete Fourier transform (DFT). By selecting the number of subcarriers, different amounts of intersymbol interference (ISI) can be accounted for (e.g. large amounts of channel dispersion can be accounted for with a larger number of subcarriers, and thus longer OFDM symbols). A cyclic prefix is typically appended between OFDM symbols, which acts as a guard for ISI between symbols.

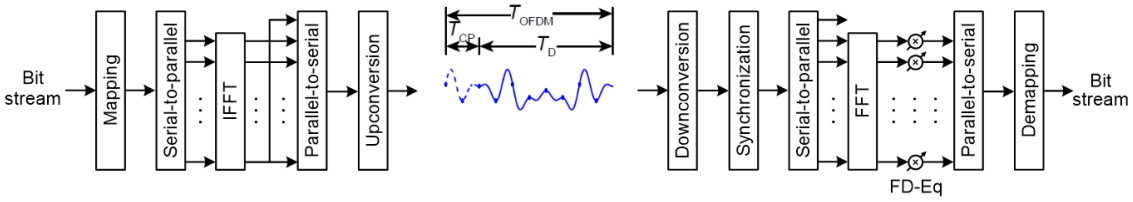

Fig. 1. Block diagram of OFDM generation and demodulation.

Discrete multi-tone (DMT) is another popular multicarrier format that is effectively a subset of OFDM [4]. DMT ensures real-valued transmitted signals by forcing the input symbols to symmetric subcarrier pairs to be complex conjugates of each other. Achievable data rates are half that of OFDM under the same bandwidth constraints.

2.1.3 Time-domain Hybrid Modulation Formats

Time-domain hybrid modulation formats (TD-HMFs) are a subset of single-carrier QAM formats, wherein different symbols within a frame are allocated from different alphabets (e.g. QPSK1-8QAM2 has a frame size of three, with one symbol represented by

the QPSK alphabet and two symbols represented by the 8QAM alphabet) [5]. While each symbol has an integer spectral efficiency (SE), the average SE is non-integer and thus offers more flexibility in optimizing the single-carrier performance, without modifying the signal bandwidth. This method is analogous to bit-loading in multicarrier formats.

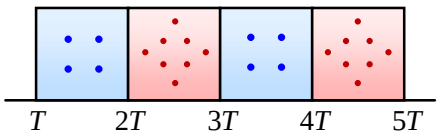

Fig. 2. Structure of hybrid QAM comprised of QPSK(1)-8QAM(1).

2.1.4 Probabilistic Shaping

Probabilistic shaping (i.e. non-uniform signalling) is another means of approaching the channel capacity (similar to TD-HMF or bit-loading) wherein different symbols within a constellation alphabet occur with a non-uniform probability distribution [6]. The probability of a symbol occurring follows a Maxwell-Boltzmann distribution in order to maximize the signal entropy, when optimizing the trade-off between average signal energy and bit rate. Probabilistic shaping has been demonstrated in the optical networking community [7] and is of high interest for increased link capacity in long-haul networks.

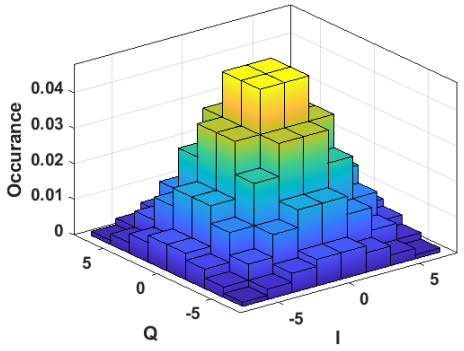

Fig. 3. Example distribution of probabilistically shaped 64QAM, which has a spectral efficiency of 5.5.

2.1.5 Geometric Shaping

Another means of addressing channel impairments is geometric shaping wherein the constellation shape is distorted [8]. Constellation shapes can be optimized to various criterions, e.g., El-Rahman and Cartledge [9] optimized QAM constellations by maximizing the mutual information (MI) for DP-16QAM and DP-QPSK, whereas Zhang et al. [10] minimized the analytical BER for 2D- and 4D-8QAM formats. Hybrid geometric and probabilistic shaping has even been demonstrated to approach the Shannon limit for long-haul fiber links [11]. Constellations can also be distorted to account for channel impairments other than AWGN, including phase noise [12]. In some practical systems with limited DAC resolution geometric shaping suffers compared to square-QAM formats [13].

2.2 Fiber Optic Communication Links

There are various forms of fiber optic-based communication link. For the sake of this proposal, a distinction will be made between fiber transport and RF photonic links.

2.2.1 Fiber Transport Links

Fiber transport can be divided into different regimes corresponding to the distance of transmission and capacity; common regimes are: metro access, metro interoffice, and long-haul [14]. Metro access extend up to a few kilometers from central offices to businesses and homes. Metro interoffice extends up to several tens of kilometers between offices within a city or region. Long-haul corresponds to distances spanning hundreds to thousands of kilometers between central offices across regions: this includes terrestrial and submarine links. Though metro is a burgeoning field due to strong interest in intra and inter data center applications (low-latency), this proposal focuses primarily on long-haul applications (high-spectral efficiency).

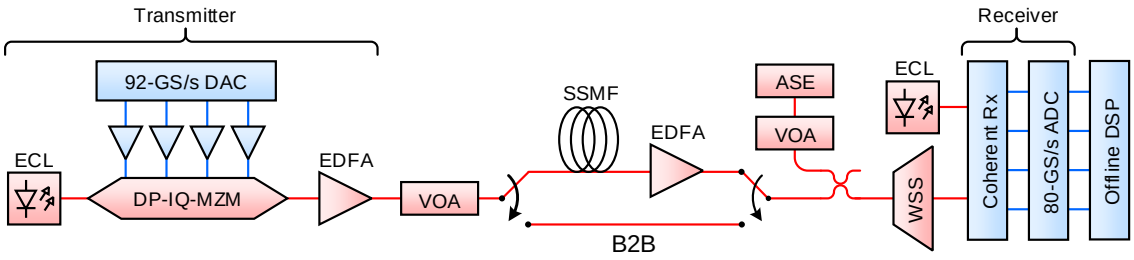

Fig. 4. Block diagram of long-haul fiber optic test-bed. Red elements are optical and blue elements are electrical/digital.

Long-haul links are designed for maximum capacity transmission and thus multiplex information on multiple dimensions, namely time, quadrature, polarization, and wavelength. Such a link entails coherent reception, and a simplified architecture (single-wavelength) of such a link is shown in Fig. 4. Many research efforts are also on space division multiplexing (SDM), wherein information is multiplexed on different fiber modes or cores, but such a scheme is not deployed in actual networks due to expensive, specialty fiber and components [15]. The state-of-the-art (in terms of data rate per single-carrier) publication for long-haul links utilized digital bandwidth interleaving of multiple DACs to yield 240-GS/s with 100-GHz of bandwidth. Chen et al. [16] achieved 1.61-Tb/s per carrier using entropy loading (2 bands of 33.5-Gbd DP-64QAM, 2 bands of 23.1-Gbd DP-64QAM, and 2 bands of 31.5-Gbd DP-QPSK) with the aforementioned DACs. Schuh et al. [17] achieved 1.2-Tb/s per carrier using simpler modulation: 100-Gbd DP-64QAM.

2.2.2 V-band RF Photonic Links

The V-band is the standard microwave band that ranges from 40- to 75-GHz and though it exhibits a large attenuation of 10-dB/km due to the oxygen peak, it is a good candidate for short distance, high-speed wireless communication. Hybrid photonic links enable long distance fiber transmission paired with short distance wireless transmission,

with high bandwidth frequency conversion capabilities. The papers listed in this section are state-of-the-art systems with increasing data rates, all with V-band wireless transmission and some length of fiber transmission.

Li et al. [18] demonstrated a real-time architecture for the transmission of 24-Gbps 16QAM-OFDM over 20-km SMF and 4-m air; the architecture employs photonic upconversion and electrical downconversion to and from a 57-GHz carrier. Chiang et al. [19] demonstrated 29.3-Gbps 16QAM-OFDM over 4-km SMF and 3-m air; the transmission employed photonic upconversion to a 62-GHz carrier and power detector down-conversion. Li et al. [20] demonstrated 2×2 MIMO, 10-Gbd 64QAM (120-Gbps) over 80-km SMF and 1-m air; the architecture utilized photonic upconversion to a 57-GHz carrier and digital downconversion using a 160-GS/s ADC. Jenkins et al. [21] demonstrated 18-Gbd DP-16QAM (144-Gbps) over 25-km SMF and 2.5-m air using photonic upconversion to a 63-GHz carrier and electrical downconversion.

2.2.3 W-band RF Photonic Links

The W-band is another microwave band of interest for high bandwidth communication and ranges from 75- to 110-GHz (exhibiting a water peak in the atmospheric attenuation near 110-GHz). Zhang et al. [24] experimentally demonstrated frequency division multiplexed (3 channels), 2×2 MIMO, 10-Gbd DP-QPSK over 80-km SMF and 2-m air for a net data rate of 120-Gbps. Li et al. [25] demonstrated 2×2 MIMO, 39-Gbd DP-QPSK transmission over 80-km SMF and 2-m air for a net data rate of 146-Gbps on 100-GHz RF carriers. Yu et al. [26] demonstrated 4×4 MIMO, 27-Gbd PDM-16QAM transmission over 2-m air for a net data rate of 432-Gbps on 94-GHz RF carriers. For the papers listed, polarization division multiplexing occurs in the optical domain and

not necessarily in the wireless domain: different polarization components are mapped to different antennas via optical polarization-diversity up-converters. Li et al [27] demonstrated 18-Gbd 16QAM-OFDM transmission over 2 spans of 20-km SMF for a net data rate of 72-Gbps on a 95-GHz.

2.3 Fiber Link Impairments

Before considering techniques employed in receiver DSP for demodulation, the types of impairments incurred in fiber transport must be considered as physical models educate DSP algorithm choices, and in the words of Haykin, "Signal processing is at its best when it successfully combines the unique ability of mathematics to generalize with both the insight and prior information gained from the underlying physics of the problem at hand" [22]. The first impairments considered are those due to fiber propagation, whereas latter impairments considered are from network and system hardware.

2.3.1 Linear Fiber Propagation Impairments

2.3.1.1 Loss

The primary sources of intrinsic loss in silica fiber are from material resonances and Raleigh scattering. In the conventional band (C-band), ultraviolet resonance is negligible whereas infrared (IR) resonances arising from the lattice vibration of silica and dopants results in absorptive resonances between 7 and 11-μm [23].

Rayleigh scattering occurs when radiated light excites and is reradiated by atomic dipoles with the silica fiber. Scattering centers are created in the fiber when structural irregularities are frozen into the fiber during manufacturing.

The output power of an optical fiber is described as:

$$P_{\text{out}} = P_{\text{in}} e^{-\alpha L} \tag{1}$$

where α is the fiber attenuation in units of 1/km and L is the propagation length in km. Conventionally, the attenuation of a fiber is provided in units of dB/km resulting in the loss being described as:

$$P_{\text{out}} = P_{\text{in}} 10^{-\frac{\alpha_{\text{dB}} L}{10}} \tag{2}$$

where $\alpha_{\text{dB}} \approx 4.343\alpha$ and is typically about 0.18-dB/km.

2.3.1.2 Chromatic Dispersion

Chromatic dispersion (CD) is the consequence of the phase constant β of a wave varying nonlinearly with frequency, resulting in different frequency components of a signal propagating at different velocities through a medium [23]. CD is comprised of two components: material dispersion due to the frequency dependent refractive index of silica and waveguide dispersion due to wavelength dependence of field propagation in a cylindrical waveguide. The phase constant of a wave can be approximated using a Taylor series expansion:

$$\beta(\omega) \approx \beta|_{\omega_0} + (\omega - \omega_0)\frac{d\beta}{d\omega}\bigg|_{\omega_0} + \frac{1}{2}(\omega - \omega_0)^2 \frac{d^2\beta}{d\omega^2}\bigg|_{\omega_0} \tag{3}$$

$$= \beta_0 + (\omega - \omega_0)\beta_1 + \frac{1}{2}(\omega - \omega_0)^2 \beta_2 \tag{4}$$

where β_1^{-1} is called the group velocity and β_2 is the group velocity dispersion parameter. The dispersion parameter (or CD slope) $D(\lambda)$ is a useful parameter when describing fiber and is:

$$D(\lambda) = \frac{d}{d\lambda}\frac{d\beta}{d\omega} = \frac{d\omega}{d\lambda}\frac{d^2\beta}{d\omega^2} = -\frac{2\pi c}{\lambda^2}\frac{d^2\beta}{d\omega^2} \tag{5}$$

2.3.1.3 Polarization Dispersion

As the name suggests, polarization dispersion is another impairment associated with different components of an optical field propagating at different speeds. Polarization mode dispersion (PMD) is a group delay between the polarization states of an optical field due to the birefringence of the fiber [23]. Due to birefringence being a nonideality in a cylindrical, optical fiber that varies over the length of a fiber caused by bends and deformations of the fiber, PMD is not a predictable impairment. Because of its nature, PMD must be considered from a statistical point-of-view. Over short fiber distances this impairment is negligible, but over many spans of fiber, PMD can penalize the performance of a communication link. In such cases, the PMD of the fiber can be characterized as being in a strongly coupled regime and is given as:

$$\overline{PMD_c} = \frac{\overline{\Delta\tau_{pc}}}{\sqrt{L}} = \frac{\Delta N_{eff}}{c}\sqrt{2L_c} \tag{6}$$

in units of ps/√km, where $\overline{\Delta\tau_{pc}}$ is the mean differential group delay between polarizations, L is the fiber length, ΔN_{eff} is effective group index difference, and L_c is the correlation distance. Note that the PMD delay scales with the square-root of distance.

2.3.2 Receiver Noise

There are two primary sources of noise in the systems after the coherent receiver: beat noise and noise [8]. Beat noise is generated by the mixing of the optical LO and optical noise; in an ideal coherent receiver, the signal-noise and noise-noise beat terms are cancelled. The physical origin of the optical noise is primarily amplified spontaneous emission (ASE) generated by optical amplifiers and it exhibits a noise variance proportional the product of the LO power and the noise spectral density:

$$\sigma^2_{\mathrm{LO,noise}} = 4\mathcal{R}^2 N_0 P_{\mathrm{LO}} B_e \tag{7}$$

where $\mathcal{R}$ is the photodetector responsivity, N_0 is the power-spectral density of the noise, P_{LO} is the optical LO power, and B_e is the power-equivalent bandwidth of the receiver.

Erbium-doped fiber amplifiers (EDFAs) and distributed Raman amplifiers are the most commonly used amplifiers in C-band links to overcome the transmission loss. The noise spectral density (per polarization) added by EDFAs distributed periodically along the fiber can be calculated as:

$$N_{\mathrm{ASE}} = N_A(e^{\alpha L_A} - 1)h\nu_s n_{\mathrm{sp}} \tag{8}$$

where N_A is the number of amplifiers, L_A is the fiber span length, α is the fiber loss, $h\nu_s$ is photon energy, and n_{sp} is the spontaneous emission factor. Ideal distributed Raman amplifiers continuously provide gain along the length of the fiber and generate a noise spectral density of:

$$N_{\mathrm{ASE}} = \alpha L h\nu_s K_T \tag{9}$$

Where L is the total transmission length, K_T is the photon occupancy factor.

$$K_T = 1 + \frac{1}{\exp\left[h(\nu_p - \nu_s)/k_B T\right] - 1} \tag{10}$$

where k_B is the Boltzmann constant, T is temperature, and ν_p is the optical frequency of the Raman pump.

The other main source of noise at the receiver is shot noise which manifests as an independent photocurrent noise at each photodiode and its variance is proportional to the detected optical power:

$$\sigma^2_{\mathrm{shot}} = 2e\mathcal{R}PB_e \tag{11}$$

where e is the elementary charge and P is the optical power. For amplified links, the shot noise is considered negligible compared to the LO-beat noise.

2.3.3 Non-resonant Nonlinear Processes

The next few impairments considered are nonlinear impairments associated with the propagation through the optical fiber (here we only consider non-resonant processes). Though optical fiber has a very low nonlinear refractive index and nonlinear processes are thus inefficient (most other materials have a nonlinear index two orders of magnitude larger [28]), the interaction length of optical communication links can be very long, nonlinear impairments should be taken into consideration. The governing mechanism between some of the processes is the intensity-dependent refractive index [23]:

$$n \approx n_0 + n_2'|E|^2 \tag{12}$$

where n_0 is the linear refractive index (~1.45 at 1550-nm in silica), n_2' is the nonlinear refractive index (~2.7×10^{-16} cm^2/W), and $|E|^2$ is the intensity of the optical field.

2.3.3.1 Self-Phase Modulation

The first nonlinear optical fiber process being considered in self-phase modulation (SPM) in which the frequency-domain content of a propagating pulse are distorted by the change in the refractive index induced by the pulse itself. For example, the phase modulation on an optical pulse due to SPM induces a chirp and is [23]:

$$\delta\phi(z,t) = n_2' k_0 |E_0(z,t)|^2 z \tag{13}$$

The combination of dispersion and SPM can be exploited for pulse compression and is the root of optical soliton propagation [29].

2.3.3.2 Cross-Phase Modulation

In WDM systems, the refractive index is no longer influenced by the intensity of a single wavelength, but multiple, resulting in what is termed cross-phase modulation (CPM or XPM). XPM results in nonlinear cross-talk between WDM channels. Because there are many channels impacting the refractive index, one might consider XPM more impactful than SPM, but for non-dispersion managed links with large channel spacing there is considerable walk-off due to CD resulting in a reduced nonlinearity impact [14].

2.3.3.3 Four-Wave Mixing

Four-wave mixing (FWM) is the non-resonant, nonlinear process by which the interaction of three fields generate a fourth. The frequency spacing of the interacting waves satisfy the relation $\omega_1 - \omega_3 = \omega_2 - \omega_1 = \omega_4 - \omega_2$ [23]. The interaction not only generates a fourth wave, but also provides gain to the signal at the corresponding frequency. In communication links, FWM is primarily a cross-talk mechanism for WDM systems. It's impact in a WDM link can be reduced increasing the channel spacing, increasing the dispersion, and using unequal channel spacings [14]. The first two recommendations induce walk-off between the channels reducing the FWM efficiency, whereas the latter results in FWM generation outside the signal bands.

2.3.4 Laser Phase Noise

In coherent links, distributed feedback (DFB) lasers are commonly employed and exhibit relatively stable power and wavelength operation. The primary impairment considered for DFBs is the relative phase and frequency offset and fluctuations between lasers sources (at the transmitter and receiver). To first-order, the FM noise of a semiconductor laser is white, which results in a phase-error variance of [30]:

$$\sigma_{\phi}^{2}(\tau) = 2\pi\tau\delta f \tag{14}$$

where τ is the time between measurements and δf is the 3-dB laser linewidth of the field spectrum, which is a Lorentzian shape:

$$S(f) = \frac{\delta f}{2\pi[f^2 + (\delta f)^2/2]} \tag{15}$$

2.3.5 Electronics

When considering impairments due to electronics there are a variety of contenders, but we will only discuss the fundamental impairments for coherent links. Analog-to-digital converters (ADCs) and digital-to-analog converters (DACs) have specified bit resolutions defined by the physical architecture, but due to the limitations of the circuitry either from noise or nonlinearities the converters have a maximum number of bits that can be represented confidently. Thus, a converter has a rated effective number of bits (ENOB), less than the architecture bit resolution. In communication link, a minimum ENOB is required to transmit higher-order modulation formats, especially when utilizing pulse shaping and equalization. ENOB can be related to the signal to noise and distortion (SINAD) ratio [31]:

$$\text{ENOB} = \log_2(\text{SINAD}) - \frac{1}{2}\log_2\left(\frac{3}{2}\right) \tag{16}$$

Another impairment that must be considered for coherent links is the linearity of the amplifiers utilized, whether the MZM drivers at the transmitter or the transimpedance amplifiers (TIAs) at the receiver. Higher-order modulation formats such as 64QAM require high linearity for reasonable BER performance, otherwise distortion compensation methods must be employed, whether digitally or electronically.

2.4 DSP in Coherent Fiber Optic Links

Waveforms captured by a coherent receiver require DSP to correct for any impairments incurred by fiber transport. The primary blocks in conventional demodulation DSP implement matched filtering, CD compensation, timing recovery, polarization demultiplexing, carrier recovery, and additional equalization [32, 33]. A block diagram of such an architecture is shown in Fig. 5.

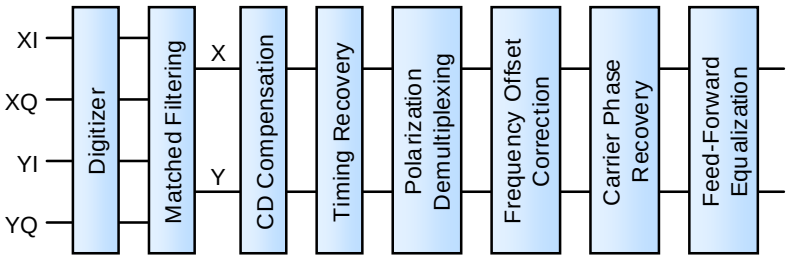

Fig. 5. Block diagram of fiber optic demodulation architecture.

2.4.1 Matched Filtering

A matched filter is the complex conjugate of the spectrum of the received waveform, and results in filtered signal with the maximum SNR [1]. The matched filter is commonly applied in the frequency domain. Matched filtering can suffer when the frequency separation between the transmitter and receiver LO is large, but in coherent optical links, the frequency offset is typically less than a percent of the signal bandwidth.

2.4.2 CD Compensation and Estimation

2.4.2.1 CD Compensation

For large transmission distances, the impact of CD on the received signal becomes significant and must be compensated for. Dispersion managed links account for this by including dispersion compensation modules or spans of dispersion compensating fiber [34]. This method requires additional hardware but yielded adequate performance before

the proliferation of DSP in coherent links. Taylor [35] proposed the use of DSP to compensate for dispersion in coherent detection links: something previously demonstrated for direct detect links, though limited due to the loss of phase information. This method has since been employed in deployed coherent links with the time-domain equalizer taps defined as:

$$a_k = \sqrt{\frac{jcT^2}{Dz\lambda^2}} \exp\left(-j\frac{\pi cT^2}{Dz\lambda^2}k\right) \tag{17}$$

where c is the speed of light, Dz is the accumulated CD, λ is the carrier wavelength, T is the sample period [36]. The required length of the equalizer is determined primarily by the accumulated CD and the signal baud rate:

$$N = 2 \cdot \left\lfloor \frac{|D|z\lambda^2}{2cT^2} \right\rfloor + 1 \tag{18}$$

When compensating for large amounts of accumulated CD frequency domain equalization (FD-EQ) is utilized with the quadratic-phase, all-pass response being described as:

$$G(\omega) = \exp\left(j\frac{Dz\lambda^2}{4\pi c}\omega^2\right) \tag{19}$$

To properly implement a linear convolution filter using a FD equalizer, which is inherently a circular convolution, overlap-and-save techniques must be utilized [37].

2.4.2.2 CD Estimation

Unlike the latter DSP blocks in the coherent demodulator, CD requires a simple, static equalizer with one degree of freedom that does not require adaptive updates. Thus, the amount of accumulated CD is typically estimated upon start-up of link and the CD compensator is set accordingly. The most common method of CD estimation requires the computing the cost function at the outputs of the CD equalization for a range of CD values:

the CD equalization that yields that minimizes the cost function is considered the correct equalizer. Because CD equalization is implemented in the frequency domain, CD estimation methods have been proposed to operate on either time- or frequency-domain samples.

Hauske et al. [38] proposed a frequency-domain cost function, $J[i]$, based on the auto-correlation, $U_{k,i}[n]$, of the equalized spectra:

$$J[i] = \sum_{k} \sum_{n} \left| U_{k,i}[n] \right|^2 \tag{20}$$

$$\begin{aligned} U_{k,i}[n] = \frac{1}{M} \sum_{m=-\frac{M}{2}+1}^{\frac{M}{2}} & \operatorname{sign}\left(\Re\left(\operatorname{circshift}\left(S_{\mathrm{out},k,i}[m], n \right) \right) \right) \cdot S^*_{\mathrm{out},k,i}[m] \\ & + j \operatorname{sign}\left(\Im\left(\operatorname{circshift}\left(S_{\mathrm{out},k,i}[m], n \right) \right) \right) \cdot S^*_{\mathrm{out},k,i}[m] \end{aligned} \tag{21}$$

where M is the size of the FFT, n is an integer less than M, and k is the FFT block index. The computational complexity of the auto-correlation is reduced by only considering the sign of the non-conjugate term. This method was demonstrated for DP-QPSK and exhibited an estimation error standard deviation of 100-ps/nm, with a maximum deviation of 400-ps/nm.

Hauske et al. [39] proposed another frequency-domain cost function based on the magnitude of the clock tone after equalization: by determining the CD that maximizes the magnitude of the clock tone, the CD can be estimated. The cost function is:

$$C(f_s, B) = \int_{-\frac{B}{2}}^{\frac{B}{2}} R(f - f_s) R^*(f + f_s) df \tag{22}$$

where $R(f)$ is the equalized spectrum, f_s is the baud rate, and B is the integration bandwidth around the clock tone. Theoretically, the magnitude of a clock tone with only CD-induced distortion is:

$$|C(f_s, B)| \approx \left|\frac{\sin(2\psi B f_s)}{4\psi f_s} S\left(\frac{B}{2} - f_s\right) S^*\left(\frac{B}{2} + f_s\right)\right| \tag{23}$$

where $\psi = -D\lambda^2\pi/c$ is related to the CD and $S(f)$ is the undistorted pulse shape. As expected, larger amounts of dispersion decrease the clock tone magnitude following the sinc function. The algorithm was demonstrated for OOK and DP-QSPK with an estimation error standard deviation of 75-ps/nm and a maximum error of 200-ps/nm.

Wang et al. [40] proposed a time-domain cost function, F_d, based on the standard deviation of the power difference between odd and even samples of the two-times oversampled output of the CD equalizer.

$$F_d = \frac{\text{std}(d_x) + \text{std}(d_y)}{2} \tag{24}$$

where d_x and d_y are the distances:

$$d_{x(y)} = \frac{\left|P_{x(y)}[2n] + P_{x(y)}[2n-1]\right|}{\sqrt{2}} \tag{25}$$

where P_x is the power of the equalizer output in the X-polarization. For low values of the cost function ($F_d < 0.58$) the relation between F_d and the accumulated CD is one-to-one, enabling the use of a look-up table to estimate the CD. If $F_d > 0.58$, the CD equalizer is incremented by 1000-ps/nm and F_d is re-evaluated: this is repeated until $F_d < 0.58$. Thus, the total accumulated CD will be estimated as:

$$CD = KS + L \tag{26}$$

where K is the number of iteration steps, S is the CD step (1000-ps/nm), and L is the CD estimated from the look-up table. This method was demonstrated for QPSK and 16QAM systems with different pulse shapes with an estimation error of about 25-ps/nm. It enables coarse sweeping of the accumulated CD at the cost of using an additional look-up table.

Diniz et al. [41] proposed a CD estimation algorithm that utilizes the timing recovery error signal. The cost function, $C(n)$, is related to the variance of the timing recovery error: when the variance is lowest then then CD equalization is optimized.

$$C(n) = \frac{2}{N}\sum_{i=1}^{M}\sum_{k=1}^{N/2}(\epsilon[k] - \tilde{\epsilon}[i])^2 \tag{27}$$

where $\epsilon[k]$ is the timing error

$$\epsilon[k] = x(k)[x(k) - x(k-1)] \tag{28}$$

and $\tilde{\epsilon}[i]$ is the mean timing error. The algorithm was demonstrated for DP-QPSK and DP-16QAM, with a maximum estimation error of 100- and 125-ps/nm, respectively.

Hauske et al. [42] proposed a CD estimation algorithm to estimate residual CD using the filter taps in the polarization demultiplexing filter taps. By quadratic fitting the unwrapped phase response of the butterfly filter the residual CD can be estimated. A limitation of the proposed algorithm is that the butterfly filter must have more memory (taps) than the memory of the fiber channel due to CD: for large amounts of CD this is infeasible.

2.4.3 Timing Recovery

Timing recovery is necessary in digital receivers in order to optimally sample the received signal at maximum eye opening. Some algorithms are data-aided, requiring an additional signal for timing synchronization, but non-data-aided “filter and square”

algorithms extract timing information from the square of the signal, and are commonly employed in single-carrier, coherent links [43]. The received waveform is first filtered and sampled at an integer multiple of the baud rate, and can be represented as:

$$x_k = \left| \sum_n a_n g\left(\frac{kT}{N} - nT - \epsilon T\right) + \tilde{n}\left(\frac{kT}{N}\right) \right|^2 \tag{29}$$

where a_n is the transmitted symbol, $g(t)$ is the convolution of the transmitter pulse shape and the receiver filter, T is the symbol period, ϵ is an unknown offset, and $\tilde{n}(t)$ is the received noise. Calculating the phase of the spectral component of the square of the signal at the baud rate, yields a timing offset estimate.

$$\hat{\epsilon}_m = -\frac{1}{2\pi} \arg\left(\sum_{k=mLN}^{(m+1)LN-1} x_k e^{-j2\pi k/N} \right) \tag{30}$$

Adjusting the sampling time with the calculated normalized phase for different blocks enables good timing recovery, even amid timing jitter. Because the phase must be extracted at the baud rate, the signal must be sampled at least two times the baud rate.

Another non-data aided timing recovery method commonly used for is the Gardner algorithm [44] wherein an error sample is estimated from a received signal sampled at two times the baud rate. The error sample (for a complex signal y) is computed as:

$$u_t(r) = y_I\left(r - \frac{1}{2}\right)[y_I(r) - y_I(r-1)] + y_Q\left(r - \frac{1}{2}\right)\left[y_Q(r) - y_Q(r-1)\right] \tag{31}$$

where r is the symbol index number. Sample timing is adjusted to minimize $u_t(r)$. The algorithm operates essentially on the square of the received signal and exhibits very low computational complexity.

2.4.4 Polarization Demultiplexing

A coherent receiver detects signals with arbitrary states of polarizations that vary over time. Under single-polarization transmission conditions, optimal signal demultiplexing can be achieved using maximum-ratio polarization combining [45], whereas under dual-polarization transmission conditions other methods must be employed. The most common method, particularly for DP-QPSK systems, is the constant modulus algorithm (CMA) developed by Godard [46] and demonstrated by Savory [47] in coherent optical links. The equalizer is a butterfly-structure filter with outputs described as:

$$x_{out}(k) = \boldsymbol{h}_{xx}^{T} \cdot \boldsymbol{x}_{in} + \boldsymbol{h}_{xy}^{T} \cdot \boldsymbol{y}_{in} \tag{32}$$

$$y_{out}(k) = \boldsymbol{h}_{yx}^{T} \cdot \boldsymbol{x}_{in} + \boldsymbol{h}_{yy}^{T} \cdot \boldsymbol{y}_{in} \tag{33}$$

The filter taps are updated to force the output to have a constant envelope on both polarizations and is achieved using the update equations:

$$\boldsymbol{h}_{xx} \rightarrow \boldsymbol{h}_{xx} + \mu(1 - |x_{out}|^2) x_{out} \boldsymbol{x}_{in}^{*} \tag{34}$$

$$\boldsymbol{h}_{xy} \rightarrow \boldsymbol{h}_{xy} + \mu(1 - |x_{out}|^2) x_{out} \boldsymbol{y}_{in}^{*} \tag{35}$$

$$\boldsymbol{h}_{yx} \rightarrow \boldsymbol{h}_{yx} + \mu(1 - |y_{out}|^2) y_{out} \boldsymbol{x}_{in}^{*} \tag{36}$$

$$\boldsymbol{h}_{xx} \rightarrow \boldsymbol{h}_{xx} + \mu(1 - |y_{out}|^2) y_{out} \boldsymbol{y}_{in}^{*} \tag{37}$$

The multi-modulus algorithm (MMA) has been demonstrated as a decision-directed means of demultiplexing formats such as 16QAM and 64QAM in coherent links [48]. The filter updates are equivalent to the CMA filter updates, except that the errors are calculated relative to a decision radius.

A limitation of CMA and MMA is that the outputs of the algorithms can converge to the same input polarization when non-negligible amounts of polarization dispersion loss (PDL) is present in the optical link [49]. Various algorithms have been proposed as

modifications to the CMA algorithm to ensure convergence to unique polarizations. Liu et al. [50] proposed training a single-tap CMA for a single-polarization X, then computing the polarization orthogonal to X yielding an estimate for Y. After training, multi-tap CMA is used with the initial, center taps estimated from training. Xie and Chandrasekhar [51] proposed a two-stage algorithm wherein the first-stage is a modified single-tap equalizer that estimates X using CMA and computes Y as orthogonal to X. The second-stage is a conventional multi-tap CMA equalizer.

Non-CMA-based algorithms have also been demonstrated in the literature, with their primary benefits arising from avoiding the singularity issue and being better optimized for higher-order modulation formats.

Zhang et al. [52] proposed the use of (single-tap) independent component analysis (ICA) to separate the optical polarizations based on matching to circular Maxwellian distributions. Similar performance was achieved to CMA for QPSK (without convergence to a singularity), though the method can be modified to account for higher-order modulation formats by changing the matching distribution. The method can also be modified to include multiple taps. Xie et al. [53] similarly proposed an ICA-based algorithm, but the adaption is based on maximizing the marginal kurtosis and does not require modifications for use with higher-order modulation formats. Johannisson et al. [54] demonstrated that the initial convergence of ICA is faster than CMA for QPSK. It is also comparable in computational complexity requiring two phase extractions and eight more multiplications. The update equations are:

$$B_{k+1} = N_k B_k \tag{38}$$

$$N_{1,1} = 1 + \mu(1 - |x_{out}|^2) \tag{39}$$

$$N_{1,2} = \frac{\mu|a|}{2\sigma^2}\left(e^{j\phi_1}y_{out}^* - x_{out}e^{-j\phi_2}\right) - \mu x_{out}y_{out}^* \tag{40}$$

$$N_{2,1} = \frac{\mu|a|}{2\sigma^2}\left(x_{out}^* e^{j\phi_2} - e^{-j\phi_1}y_{out}^*\right) - \mu x_{out}^* y_{out} \tag{41}$$

$$N_{2,2} = 1 + \mu(1 - |y_{out}|^2) \tag{42}$$

where B_k is the 2×2 inversion matrix, and a and σ are constants describing the matching normal distribution.

Stoke-space-based algorithms have also been demonstrated for singularity-immune and modulation format agnostic polarization demultiplexing. The Stokes-space transformation applied before polarization demultiplexing is:

$$\vec{S} = \begin{pmatrix} |E_X|^2 - |E_Y|^2 \\ 2\mathrm{Re}\{E_X E_Y^*\} \\ 2\mathrm{Im}\{E_X E_Y^*\} \end{pmatrix} \tag{43}$$

where E_X and E_Y are the complex electric fields on both polarizations.

Szafraniec et al. [55] proposed mapping received dual-polarization signals to Stokes-space and estimating the inversion matrix from the principal plane. The method presented only yields a single-tap butterfly filter and is not an adaptive algorithm, so it cannot track polarization fluctuations with time or compensate for any residual dispersion not accounted for by CD compensation. Though other Stokes-space methods have been proposed for adaptive inversion matrix updates [56,57], most methods are limited to single-tap implementations.

2.4.5 Frequency Offset Correction

After polarization demultiplexing, the phase offset between the transmitter and receiver LOs must be corrected. A distinction is made between frequency offset correction and carrier phase recovery (CPR), though both correct the phase offset. Frequency offset

correction accounts for the frequency difference between the LOs and exploits the four-fold symmetry of typical single-carrier modulation formats. The IF is determined by finding the peak in the Fourier transform of the signal to the fourth power [58], and correction is completed by downconverting the signal at the corresponding frequency.

2.4.6 Carrier Phase Recovery

CPR algorithms compensate for any residual carrier phase offset not accounted for by frequency offset correction. Viterbi-and-Viterbi carrier phase estimation is commonly applied for systems with *m*-PSK formats [**59**]. The phase estimate is related to the average phase of a symbol modified by a nonlinear transformation. In the case of QPSK, the nonlinear transformation is the fourth-power, due to the four-fold symmetry of a QPSK constellation, thus the phase estimate is calculated as:

$$\phi_n = \arg \sum_{k=1}^{N} x_{n+k}^4 \tag{44}$$

where N is the block size averaged over [32]. Though a rough estimate can be attained for QAM formats using the Viterbi-and-Viterbi method, decision directed algorithms, such as the "stop-and-go algorithm" [60], are necessary for higher accuracy.

Tarighat et al. [61] proposed an adaptive decision-directed phase recovery algorithm with single-tap LMS updates:

$$w_i = w_{i-1} + \mu y_i[\text{slicer}(\hat{s}_i) - w_{i-1} y_i] \tag{45}$$

where $\hat{s}_i = w_{i-1} y_i$ is the output of the equalizer and the slicer estimates the closest symbol. Decision errors can result in large phase updates, thus it is recommended that if a calculated phase offset results in an output with a different slicer output, do not change the phase offset to the calculated phase offset.

2.4.7 Residual Equalization

Before slicing or demapping, a final adaptive equalizer can be used to correct for any residual filtering effects. This is commonly implemented as a decision-directed, complex LMS equalizer described by Widrow [62]. The output at time k of the equalizer is described as:

$$y_k = \boldsymbol{X}_k^T \boldsymbol{W}_k \tag{46}$$

where the filter weights are updated according to:

$$\boldsymbol{W}_{k+1} = \boldsymbol{W}_k + 2\mu(d_k - y_k)\boldsymbol{X}_k^* \tag{47}$$

where d_k is the symbol decision.

2.5 Waveform Characterization

2.5.1 Coherent Single-Carrier QAM and PSK Classification

There is a plethora of single-carrier format identification papers in the literature, but here we will focus on single-carrier format identification for coherent links. Methods applied to coherent links typically operate either on the measured field parameters or the mapped Stokes parameters (representing the intensity and polarization). Khan et al. [63] applied deep neural network processing to the amplitude histograms at the output of CMA equalization to classify between 4-, 16-, and 64QAM, as well as estimate the OSNR.

Of the formats employing Stokes space parameters, Borkowski et al. [64] applied a variational Bayesian expectation maximization based Gaussian mixture model to mapped Stokes parameters for constellation estimation of formats ranging from BPSK to 16QAM. Isautier et al. [65] employed Stokes space processing paired with higher-order cumulants (HOCs) and spatial correlation to discriminate between M-PSK and M-QAM formats (up to 16QAM). Hao et al. [66] applied probabilistic neural networks to amplitude histograms

of Stokes parameters in order to classify M-PSK and M-QAM formats (up to 64QAM). A limitation of cluster-based classification in Stoke-space is the large number of clusters for higher-order modulation formats (e.g. DP-16QAM is represented by 60 clusters in Stokes-space).

2.5.2 Hybrid Format Classification

Extending the classification of single-carrier formats to include non-integer spectral efficiency, Isautier et al. [105] demonstrated a format recognition architecture for TD-HMFs, including 31.5-Gbd dual-polarization transmission of formats ranging from BPSK to 16QAM. The architecture included various DSP blocks that not only estimate general modulation and link parameters (baud rate and accumulated CD), but also parameters specific to TD-HMFs, particularly the frame length and pattern ratio. The format classification depended on HOCs for format classification. Xiang et al. [70] also demonstrated a format identification aided transceiver that addressed hybrid and set-partitioned formats, though it is data-aided and requires modulation format information encoded on pilot symbols used for CPR.

2.5.3 OFDM Classification

Al-Habashna et al. [67] presented an architecture for the classification of mobile WiMAX and 3GPP LTE using the cyclic autocorrelation function (CAF) in association with a binary decision tree. The features of interest derived from the CAF are the preamble, cyclic prefix, and reference signal (an element embedded in specific subcarriers and OFDM symbols for channel estimation and acquisition purposes). The method was demonstrated to be unaffected by phase, frequency, and timing offsets.

Sun et al. [68] presented a method for generic classification of OFDM modulation parameters based on the periodicity of the CP in the CAF. The parameters calculated from the method were the CP duration and the OFDM symbol period.

2.6 Cyclostationary Processing

The cyclic autocorrelation function (CAF) is defined as:

$$\mathcal{R}_x^{\alpha}(\tau) = \int_{-\infty}^{\infty} x\left(t + \frac{\tau}{2}\right) x^*\left(t - \frac{\tau}{2}\right) e^{-j2\pi\alpha\tau}\, dt \tag{48}$$

where $x(t)$ is the signal of interest and α is the cyclic frequency. The spectral correlation function (SCF) is the Fourier transform of the CAF, and can be written as:

$$\mathcal{S}_x^{\alpha}(\tau) = \int_{-\infty}^{\infty} \mathcal{R}_x^{\alpha}(\tau) e^{-j2\pi f\tau} d\tau \tag{49}$$

The first cyclic spectrum is the SCF evaluated at the symbol rate of the signal of interest, $\mathcal{S}_x^{\alpha=F_b}(f)$. The cyclic periodogram is used to estimate the SCF [71] and is calculated as:

$$\frac{1}{T} X_T\left(t, f + \frac{\alpha}{2}\right) X_T^*\left(t, f - \frac{\alpha}{2}\right) \tag{50}$$

where X_T is the Fourier transform of the signal of interested, evaluated over an interval T.

2.7 Cyclostationary Processors in Fiber Optic Links

Esman et al. [74] developed a wideband photonics-assisted cyclostationary processor (CSP). The processor uses frequency locked optical combs to downconvert and channelize the received electrical waveform with an IQ-receiver. By tuning the optical filters different subchannels can be accessed and captured using low speed balanced photodiodes (PDs). Though the system enables generating the SCF from a wideband signal using minimal digital computation the resolution of the SCF is limited by the number of generated optical comb lines. Furthermore, the multiplication of the received Fourier

coefficients is still implemented in the digital domain, not exploiting the high-bandwidth capabilities of optical fiber links.

Shalihah et al. [75] demonstrated the correlation of independent signals in the optical domain. First, a received signal was modulated onto a pulse train and a dispersive element spread the spectral components in the time-domain (i.e., different times correspond to different Fourier coefficients). This was similarly done for a known signal, after which both were combined and passed through a highly nonlinear fiber (HNLF) to implement the multiplication of the Fourier coefficients. The correct four wave mixing (FWM) term was selected by an optical bandpass filter (OBPF). The purpose of the setup was to determine how correlated two waveforms were and, thus, the OBPF output was compressed in the time domain using dispersion compensating fiber and detected by a PIN PD: strong peaks in the electrical waveform correspond to high correlation.

Sadler [76] presented a framework for and simulations of different CSPs that are able to calculate the cyclic spectrum and spectral correlation using acousto-optic cells and 1D and 2D detectors arrays, respectively.

2.8 Cyclostationary Processing Applied to Fiber Optic Links

The amount of literature dedicated to CS processing applied to fiber optic links is very small as it is typically discussed abstractly and for general communication waveforms. But CS processing has been investigated for some specific fiber optic link problems.

Ionescu et al. [77] presented CS-based tools for optical communication link monitoring. The work demonstrated novel methods of estimating the CD, OSNR, and pulse shape roll-off. They demonstrated that the cyclic spectrum exhibits a linear phase shift related to the accumulated CD and can be estimated at the receiver. Roll-off estimation was

attained by computing the ratio between the DC and symbol-rate peak in the cyclic autocorrelation function, though poorer performance was shown at lower roll-offs. The OSNR was estimated by relating the power of the cyclic spectrum to the power spectral density (PSD) using a known scaling factor, with performance degrading with lower noise levels. The work also presented a means of estimating the symbol-rate by finding the peak spectral tone in the SCF; this method is analogous to the method presented by Mazet and Loubaton [78] which estimates the symbol-rate by finding the peak in the CAF.

CHAPTER 3. SINGLE-CARRIER BLIND CLASSIFICATION

3.1 Cyclostationarity-Based Classification

The first classification architectures uses higher-order cyclostationarity (CS) statistics, namely the spectral correlation function (SCF) and higher-order cyclic cumulants (HOCCs), which enables the classification of important transmission parameters without the requirement to first perform an accurate timing recovery where optimal methods are often format dependent. These CS based methods also operate at arbitrary sample rates and without carrier frequency offset (CFO) correction or carrier phase recovery (CPR). Using CS statistics and HOCCs we experimentally demonstrate robust classification of dual-polarization QPSK, 16QAM, and 64QAM up to 40-Gbaud transmitted over various fiber distances.

3.1.1 Higher-order cumulants

HOCs have been employed for automatic format classification [80] since M-QAM formats have distinct fourth-order cumulants, and simple thresholds can be used to classify the different formats. This is typically done after timing recovery to that ensure the samples used are at maximum eye opening. To circumvent timing recovery in the classification process, we evaluate HOCCs at the cyclic frequency of the received waveform are used:

$$\hat{C}^{\alpha}_{x,4,2}(0) = \mathcal{F}\{|x(k)|^4\}|_{\alpha} - |\mathcal{F}\{x^2(k)\}|_{\alpha}|^2 - 2\mathcal{F}^2\{|x(k)|^2\}|_{\alpha} \tag{51}$$

$$\begin{aligned}\hat{C}^{\alpha}_{x,6,3}(0) = {} & \mathcal{F}\{|x(k)|^6\}|_{\alpha} - 9\mathcal{F}\{|x(k)|^4\}|_{\alpha} \cdot \mathcal{F}\{|x(k)|^2\}|_{\alpha} \\ & + 12|\mathcal{F}\{x^2(k)\}|_{\alpha}|^2 \cdot \mathcal{F}\{|x(k)|^2\}|_{\alpha} + 12\mathcal{F}^3\{|x(k)|^2\}|_{\alpha}\end{aligned} \tag{52}$$

We employ a normalized HOCC, weighted by the noise variance at different SNRs [81]:

$$\tilde{C}_{x,p,q}^{\alpha}(0) = \frac{\hat{C}_{x,p,q}^{\alpha}(0)}{\left[\hat{C}_{x,2,1}^{\alpha}(0) - 1/\mathrm{SNR}\right]^{p/2}} \tag{53}$$

3.1.2 Architecture

The proposed CS-based classification architecture, Fig. 6, first estimates the SCF using the cyclic periodogram described by Eq. 50. Subsequently, the baud rate is estimated from the SCF. Resampling is then applied to attain an integer number of samples per symbol, though not necessarily at maximum eye opening. The accumulated CD is then determined from the SCF and the now known baud rate as described by Eq. 3. Frequency domain CD equalization is then applied using the estimated parameter. Polarization demultiplexing must use a method that does not depend on proper sampling, hence, a Stokes space-based method is employed, wherein Stokes parameters are calculated on a sample-by-sample basis and the principal plane is estimated and used to invert polarization rotations.

Following polarization demultiplexing, the normalized HOCCs are estimated for use in modulation format classification, i.e. $\tilde{C}_{x,4,2}^{0}(0)$, $\tilde{C}_{x,4,2}^{1/T_b}(0)$, $\tilde{C}_{x,6,3}^{0}(0)$, $\tilde{C}_{x,6,3}^{1/T_b}(0)$. Principle component analysis is applied to the four normalized HOCCs, resulting in features 1, 2, 3, and 4. Using these features, a simple, linear threshold cannot be used to discriminate modulation format, thus a support vector machine (SVM) is employed to estimate the binary classifiers to discriminate between the modulation formats at various OSNRs and fiber transmission lengths. The threshold, or decision boundary, is created using a training set of data. To keep the classifier simple, the data is typically transformed into a higher dimension using kernel functions and separated using simple hyperplanes. When estimating the hyperplane, the distance between the closest data point and the

boundary is maximized to improve the performance of the classifier. To generalize the classifier, a small room for error, or slack, is included in the optimization process, resulting in a soft margin classifier. Here we use soft margin SVMs with radial basis function (RBF) kernels to classify the data.

The classification architecture first applies the threshold to discriminate between QPSK and higher-order M-QAM. If the format is not classified as QPSK, then a subsequent 16QAM versus 64QAM classifier is used.

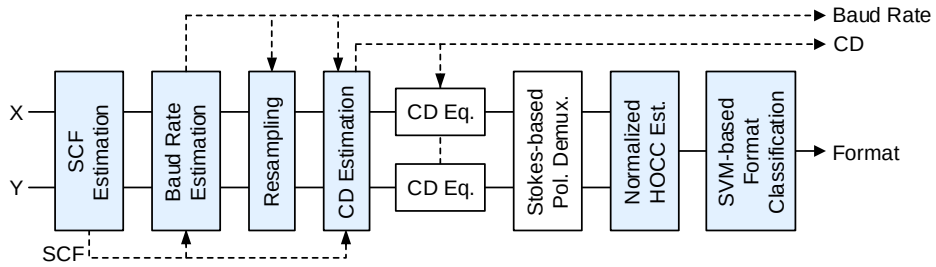

Fig. 6. Cyclostationarity-based QAM format classification architecture.

3.1.3 Experimental Results

A conventional dual-polarization, single-carrier fiber optic link (Fig. 4) is employed to experimentally validate the classifier architecture. Optical waveforms (including 20-, 32-, and 40-Gbd DP-QPSK, 16QAM, and 64QAM) were transmitted over 0-, 90-, and 180-km of SSMF.

Fig. 7 presents the results of the modulation format classification. Fig. 7a shows the results of a RBF kernel-based SVM applied to features 1 and 2 for waveforms after B2B transmission with an OSNR ranging from 9- to 40-dB. QPSK is shown to be readily discriminated yet 16QAM and 64QAM are occasionally tightly adjacent for these features. Fig. 7b shows the corresponding probability of correct classification using all features after B2B transmission. There is greater than 90% classification of QPSK and 16QAM

waveforms over the OSNRs captured (from 10- to 25-dB). 64QAM had perfect classification for OSNRs above 25-dB: at lower OSNRs discrimination is misclassified as 16QAM.

Fig. 8a shows features 1 and 2 for all fiber lengths investigated, along with the associated thresholds. Figure 3d shows the probability of correct classification for all fiber lengths using all features. Classification performance is similar to B2B transmission, though 16QAM exhibits slightly worse classification at some baud rates.

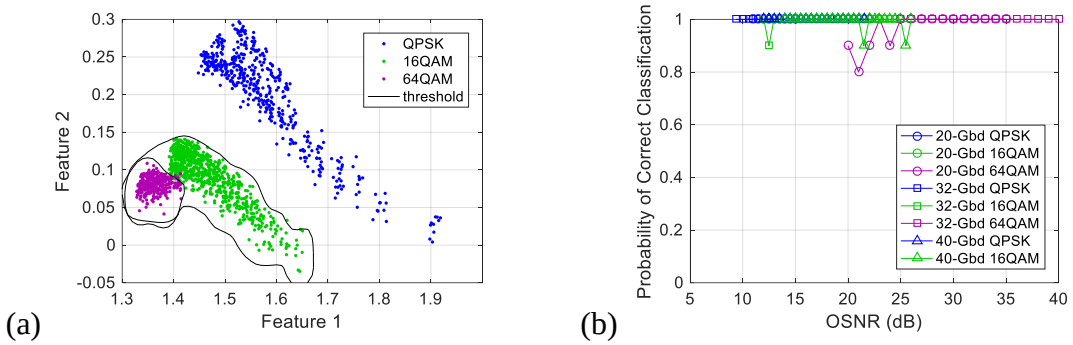

Fig. 7. HOCC classification and thresholds for back-to-back transmission. (a) Features 1 and 2 with thresholds determined by an RBF kernel SVM for various formats and baud rates. (b) Probability of correct classification based on classification using all features.

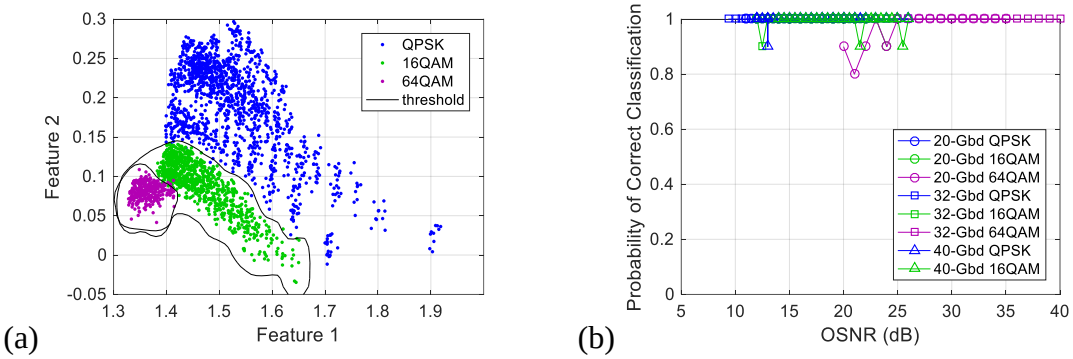

Fig. 8. HOCC classification and thresholds for back-to-back, 90-, and 180-km transmission. (a) Features 1 and 2 with thresholds determined by an RBF kernel SVM for various formats and baud rates. (b) Probability of correct classification based on classification using all features.

Though SVM is more computationally expensive than methods dependent on decision trees (employing constant decision thresholds), normal operation has a reduced complexity by using the thresholds determined with a one-time training. Furthermore, SVM enables a rich decision boundary, compared to constant or linear thresholds, important when discriminating between HOCCs for higher-order modulation formats.

Finally, this work demonstrates the ability to performer modulation classification with a significant reduction in the number of necessary conventional demodulation DSP blocks, which other architectures depend on. CD equalization and polarization demultiplexing are the only necessary blocks. The blocks unused in format classification are similarly noted: timing recovery, CFO correction, CPR, and feed-forward equalization (FFE).

3.2 Adaptive Rate Classification

Though the architecture in the previous section can classify square M-QAM formats to high accuracy over reasonable OSNRs, it is formats with simple constellation shapes and uniform symbol distributions, based on dependence on cumulants. To address this limitation, a blind adaptive rate architecture was developed to account for even more complex modulation schemes, which are increasingly more common in long-haul coherent links. The architecture can classify arbitrary constellation shapes and probabilistic shaping.

3.2.1 Architecture

The classification architecture presented here is based on the framework of a conventional DSP demodulation architecture. DSP and machine learning blocks are embedded to estimate relevant modulation and channel parameters, and certain DSP demodulation blocks are modified to account for the range of possible received waveforms.

Because of the similar architecture topologies, demodulation can be subsequently applied using the estimated parameters and produce equivalent BER performance to a conventional demodulation architecture. A block diagram of the proposed architecture is shown in Fig. 9. The order was chosen as listed due to the dependency of later blocks on parameters estimated by earlier blocks. The inputs to the architecture are the analog photocurrents of an optical coherent receiver, including in-phase and quadrature-phase components (represented as complex values) for both polarizations.

Cyclostationarity-based processing is applied to the digitized waveforms to estimate the baud rate, pulse shape roll-off, and accumulated CD. With these parameters known, conventional matched filtering, CD compensation, timing recovery, and polarization demultiplexing is applied. Frame size and rotational symmetry order estimation is performed with frequency offset correction before carrier phase recovery. Constellation clustering is applied before and after the decision-directed linear equalizer in order to accurately estimate the constellation size (format), constellation shape, and symbol distribution. The outputs of the architecture are the equalized symbols, with associated modulation parameters.

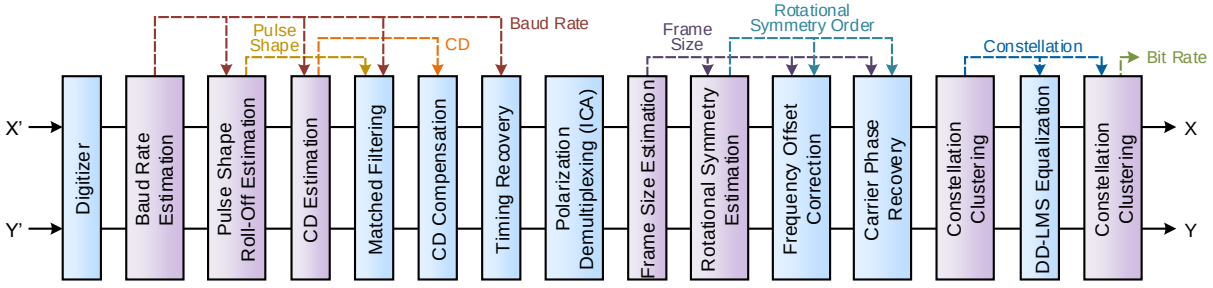

Fig. 9. Block diagram of the classification architecture. Blue blocks correspond to DSP demodulation blocks, whereas purple blocks correspond to parameter estimation blocks. Inputs and outputs are complex.

3.2.1.1 Cyclostationarity-based Processing

While the power spectral density (PSD) is useful for some waveform characterization applications (e.g., bandwidth, spectral shape, and SNR estimation), the spectral correlation function (SCF) and the cyclic spectrum yield additional information about a received waveform necessary for MFR.

The cyclic autocorrelation function (CAF) of an arbitrary signal $x(t)$ is the Fourier coefficients of the autocorrelation at the cyclic frequencies, α, and is defined as:

$$\mathcal{R}_x^{\alpha}(\tau) = \int_{-\infty}^{\infty} x\left(t + \frac{\tau}{2}\right) x^*\left(t - \frac{\tau}{2}\right) e^{-j2\pi\alpha t} dt \tag{54}$$

The SCF is the Fourier transform of the CAF:

$$\mathcal{S}_x^{\alpha}(f) = \mathcal{F}\{\mathcal{R}_x^{\alpha}(\tau)\} = \int_{-\infty}^{\infty} \mathcal{R}_x^{\alpha}(\tau) e^{-j2\pi f\tau} d\tau \tag{55}$$

It is multi-dimensional, with the independent variables being the frequency, f, and cyclic frequency. The SCF can be efficiently estimated as the cyclic periodogram over a time interval T, at time t:

$$\hat{\mathcal{S}}_{x,T}^{\alpha}(t,f) = \frac{1}{T} X_T\left(t, f + \frac{\alpha}{2}\right) \cdot X_T^*\left(t, f - \frac{\alpha}{2}\right) \tag{56}$$

where X_T is the Fourier transform of $x(t)$, measured over the interval $[t - T/2, t + T/2]$. The CAF measures correlation between time-samples at different cyclic frequencies, whereas the SCF measures the spectral density of the correlation.

Conventional (linear modulated) communication waveforms are 2nd-order cyclostationary and exhibit high correlation at the cyclic frequency corresponding to their symbol rate, $f_b = 1/T_b$.

The cyclic spectrum is the SCF evaluated at a particular cyclic frequency and is predominately non-zero for two cyclic frequencies: $\alpha = 0$ and $\alpha = f_b$. The cyclic spectrum at zero cyclic frequency corresponds to the PSD and the cyclic spectrum evaluated at the

signal baud rate is used for pulse shape roll-off and CD estimation. Signals that contain static frame headers (that do not change with each frame) are periodically correlated at integer multiples of the frame rate; these harmonics appear in the SCF at lower amplitudes than the cyclic spectra at $\alpha = 0$ and $\alpha = f_b$. For sufficiently high cyclic frequency resolution these harmonics can be clearly observed. For typical cases with lower resolution (e.g., baud rate and CD estimation) the content appears as a raised noise floor in the SCF. If the header is not repeated, the SCF is indiscernible from the SCF of a signal without a header, even if the header and payload are different modulation formats.

For classification purposes, the PSD can be employed to estimate pulse shape parameters, though performance suffers under closely-spaced channel conditions. On the other hand, the cyclic spectrum performs well even with closely spaced channels.

3.2.1.2 Baud Rate Estimation

Because the SCF is non-zero at two cyclic frequencies (0 and f_b), peak finding across non-zero cyclic frequencies is used for baud rate estimation. This method is effectively equivalent to that described by Mazet and Loubaton [78], though the cyclic periodogram (Eq. 50) is employed here because it is computationally efficient when the Fourier transform is evaluated as the fast Fourier transform.

When the signal baud rate is close to half the ADC sample rate, the ridge in the SCF can be small compared to the noise at lower cyclic frequencies, thus normalization may be applied to improve performance [78]. If the bandwidth (3-dB point) is estimated from the PSD of the received signal, the peak search can be applied to a range of cyclic frequencies around the signal bandwidth, to improve baud rate estimation performance, assuming the received waveform has not incurred excessive lowpass filtering.

3.2.1.3 Pulse Shape Estimation

The magnitude of the cyclic spectrum evaluated at the baud rate is unique for different pulse shapes and roll-off factors, β. The cyclic spectra of commonly used pulse shapes can be determined analytically and are shown in Table 1, where $\tilde{f} = f/f_b$ is frequency normalized to the baud rate. Fig. 10 shows theoretical cyclic spectra evaluated at the signal baud rate for different pulse shapes, demonstrating the range of spectra for practical communication links.

Fitting the analytical expressions to the measured cyclic spectrum is a means of estimating the pulse shape and associated roll-off. The Levenberg-Marquardt algorithm [97] is employed for this purpose as it can account for the nonlinear analytical expressions. It is an iterative algorithm that minimizes the least-squares error between the sample data, $\boldsymbol{y}$, and a predefined, nonlinear model curve, $f(x, \boldsymbol{b})$ with unknown parameter vector, $\boldsymbol{b}$. The parameter update is defined as:

$$\boldsymbol{b}_{\text{new}} = \boldsymbol{b}_{\text{old}} + (\boldsymbol{J}^T\boldsymbol{J})^{-1}\boldsymbol{J}^T[\boldsymbol{y} - f(\boldsymbol{x}, \boldsymbol{b})] \tag{57}$$

where $\boldsymbol{J}$ is the Jacobian of f, with the ith row being the gradient of $f(x_i, \boldsymbol{b})$.

Table 1 – Normalized Cyclic Spectra of Different Pulse Shapes at the Baud Rate

Pulse Shape	Cyclic Spectrum
RC	$\mathcal{S}_{RC}^{f_b}(\tilde{f}) = \begin{cases} \cos^2\left(\frac{\pi\tilde{f}}{\beta}\right) & \lvert\tilde{f}\rvert < \frac{\beta}{2} \\ 0 & \text{else} \end{cases}$
RRC	$\mathcal{S}_{\text{RRC}}^{f_b}(\tilde{f}) = \begin{cases} \cos\left(\frac{\pi\tilde{f}}{\beta}\right) & \lvert\tilde{f}\rvert < \frac{\beta}{2} \\ 0 & \text{else} \end{cases}$
Rectangular	$\mathcal{S}_{\text{Rect}}^{f_b}(\tilde{f}) = \frac{1}{1-16\tilde{f}^2}\cos^2(2\pi\tilde{f})$

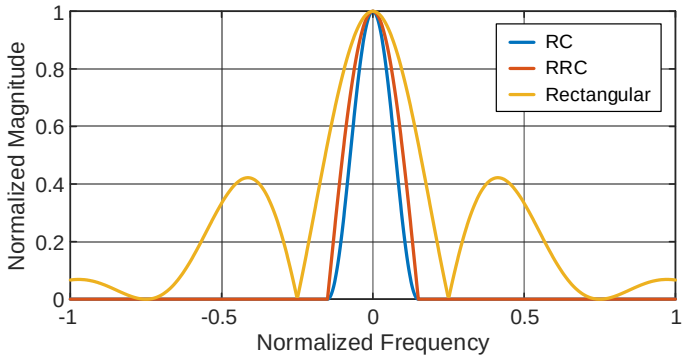

Fig. 10. Theoretical normalized cyclic spectra evaluated at the baud rate of different pulse shapes, with cyclic frequency normalized to the baud rate. RC and RRC pulse shapes shown have a roll-off factor of 0.3.

3.2.1.4 CD Estimation

The phase of the cyclic spectrum evaluated at the baud rate exhibits a linear phase shift with frequency corresponding to the accumulated CD [77]:

$$\mathcal{S}_x^{f_b}(f) = \exp\left(-j\frac{2\pi\lambda^2 DLf_b}{c}f\right) \tag{58}$$

where c is the speed of light, λ is the optical carrier wavelength, D is the fiber dispersion coefficient, and L is the fiber length. By applying a linear regression to the phase, with respect to frequency, the accumulated dispersion (DL) can be estimated. The regression must be applied over a frequency range determined by the pulse shape roll-off factor (i.e. frequencies for which the cyclic spectrum is above the noise floor).

It should be noted that performance of this method will degrade for ideal Nyquist (sinc) pulses and RC or RRC with very small roll-off factors, which all exhibit non-zero cyclic spectra over infinitesimal ranges. Practical systems do not exhibit such cyclic spectra, but in the unlikely scenario that this is the case, other CD estimation techniques can be utilized, namely the best-match search method [79].

3.2.1.5 Equalization and Timing Recovery

Equalization and timing recovery is applied on a per polarization basis, using the previously estimated modulation parameters. With knowledge of the pulse shape, matched filtering is applied to filter out-of-band noise and optimize the received SNR. CD compensation is then applied using overlap frequency domain filtering [37], from the estimated accumulated CD.

Timing recovery using the non-data-aided "filter-and-square" method [43] is applied to the filtered signal to achieve 1-sample-per-symbol at maximum eye opening.

3.2.1.6 Polarization Demultiplexing

Because the modulation format is unknown, an agnostic polarization demultiplexing method must be employed, in this case, an ICA-based method [54]. ICA is a means of separating a linearly combined mixture of statistically independent signal sources, and functions for a multitude of single-carrier modulation formats. As well as being agnostic to modulation format, an ICA-based method is immune to convergence to a singularity, contrary to the constant modulus algorithm. The resulting polarization demultiplexing filter contains multiple taps enabling significant ISI mitigation, before additional DSP.

3.2.1.7 Carrier Recovery

Carrier recovery is comprised of two distinct DSP blocks: frequency offset correction and CPR. In this architecture, frequency offset correction is similar to that described by Noe [58]. Here the intermediate frequency (IF) is determined by finding the peak in the Fourier transform of the signal to the power of the order of rotational symmetry, designated here as p. QPSK and square-QAM constellations have four-fold rotational

symmetry ($p = 4$), whereas other constellations may be of a higher order. Hex-QAM primarily exhibits 12th-order symmetry ($p = 12$), but also exhibits a peak in the Fourier transform for $p = 8$. Using only $p = 8$ or $p = 12$ for estimation will limit the range of laser frequency offsets ($\pm f_b/16$ and $\pm f_b/24$, respectively), but by accounting for both symmetry orders simultaneously the offset frequency can be resolved to a range of $\pm f_b/8$, which is sufficient for most laser frequency offsets. In rare circumstance that the frequency offset is greater than $f_b/8$, the frequency offset aliases can be tested for better classification performance.

Because the constellation shape, and thus p, are unknown at this point in the classification architecture, the Fourier transform is calculated for different values of p (4, 8, 12), and the p that yields the most prominent peak is typically considered the correct order of rotational symmetry.

Because different formats exhibit varying peak levels with OSNR, the method for estimating the rotational order is not simply determined by which peak is dominant. Instead a single-layer perceptron (a linear, binary classifier) [84] is employed to discriminate between 12th-order rotational symmetry and all other orders. The perceptron's input feature vectors are P_4, P_8, and P_{12} (the magnitudes of the peaks in the 4th-, 8th-, and 12th-order spectra, respectively). If the waveform is not classified as 12th-order, the order is considered whichever p yields the larger peak. Thus the classifier logic is described by algorithm listed below (where w is the weight vector determined by the perceptron learning algorithm).

Algorithm 1: Rotational Symmetry Order Estimation

Input: w_k and P_k, for $k = 4, 8, 12$

Output: Order of rotational symmetry

if $\text{sign}(w_4 P_4 + w_8 P_8 + w_{12} P_{12} + w_0) > 0$ **then**

$p = 12$

else if $P_8 > P_4$ **then**

$p = 8$

else

$p = 4$

end

Note, the perceptron requires one-time training to estimate the weights (independent of OSNR) and yields a very low complexity linear classifier.

Multiple peaks arise in the Fourier transform for TD-HMFs and the number of peaks is equal to the hybrid frame size, M (number of symbols per frame) [105]. The spectral locations of the peaks are $f_{\text{offset}} + f_b k/pM$, where f_{offset} is the true frequency offset and k is an integer between 0 and $M - 1$ (accounting for aliasing). The correct frequency offset is estimated by evaluating the Fourier transform of the waveform downsampled by a factor of M; this spectrum exhibits only one peak corresponding to the true frequency offset. Downsampling the signal reduces the laser frequency offset range by a factor of M, but geometric shaping and TD-HMFs are rarely used simultaneously. The signal is downconverted from the IF simply by multiplying it by a complex exponential with frequency $-f_{\text{offset}}$.

CPR is subsequently applied using the "stop-and-go algorithm" described by Picchi and Prati [60]. This decision-directed algorithm adaptively corrects for the residual phase noise not accounted for by the frequency offset correction. It uses knowledge of the signal constellation to estimate the phase error, but in this blind architecture, the constellation

shape is currently unknown, thus the constellation employed by the CPR is p-PSK (e.g. for a QPSK or square-QAM signal, CPR uses a QPSK constellation for the decision constellation). For classification purposes, rotational order-based CPR is sufficient, even for higher-order QAM. To attain better performance, in terms of BER, CPR should be subsequently applied to the received waveform with the decision constellation as the constellation estimated by the constellation clustering block, instead of the p-PSK constellation.

3.2.1.8 Constellation Classification

After CPR, the constellation clusters are estimated using the k-means algorithm and the classification is based on the Calinski-Harabasz (CH) Index [85]. Clustering is applied before decision-directed least-mean square (DD-LMS) equalization to attain an estimate of the decision constellation; clustering is then applied after equalization to attain a more accurate constellation shape and distribution estimate.

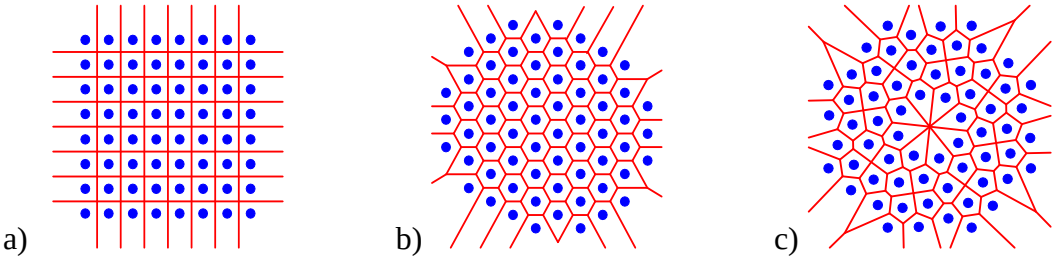

Fig. 11. Constellations investigated: (a) square-64QAM ($p = 4$), (b) hex-64QAM ($p = 12$), and (c) circle-64QAM ($p = 8$). Voronoi boundaries shown in red, corresponding to the optimal decision boundaries in an AWGN channel.

Fig. 11 shows the constellation shapes investigated here: square-, circle-, and hex-64QAM. Square-QAM is the most commonly employed constellation because it can easily be generated and is resilient to low DAC/ADC effective number of bits; whereas different

shapes are optimized for other link parameters: hex-QAM for an AWGN channel [86] and circle-QAM for binary-error correcting codes with PS [11].

3.2.1.9 Clustering

The k-means algorithm [87] is a simple clustering method that iterates over two different steps repeatedly (after cluster mean initialization). The first step assigns sample points to different clusters based on the minimum Euclidean distance to cluster means. The second step updates the cluster means as the centroid of the assigned clusters. The algorithm repeats until the means converge. In this architecture, the k-means algorithm is applied for different constellation sizes (2, 4, 8, 16, 32, and 64), with the cluster means initialized to square-QAM.

A multi-variate GMM with expectation-maximization algorithm-based updates [88] was also investigated for clustering, but it exhibits poor convergence for the constellation shapes and sizes of interest.

For TD-HMFs, clustering is applied separately to symbols from the same hybrid frame location, which have the same constellation, so that there is no overlap from different constellations during clustering. When waveforms contain both geometric and probabilistic shaping, the performance of clustering can suffer, but this combination of shaping is typically not employed. When only either geometric or probabilistic shaping is utilized, the classification performance of the architecture is much improved.

3.2.1.10 Format Classification

The constellation format is determined by evaluating the CH Index of the clustering outputs for the different constellation sizes. The CH Index is proportional to the between-cluster variance (SS_B) and inversely related to the within-cluster variance (SS_W):

$$\text{CH Index} = \frac{SS_B}{SS_W} \cdot \frac{N-M}{M-1} \tag{59}$$

where M is the constellation size and N is the number of symbols. If the constellation size is correct, the ratio of SS_B to SS_W will be maximized, thus the constellation size that yields the largest valued CH Index is considered correct. Fig. 12 shows an example of *k*-means clustering and classification criterions applied to a 16QAM constellation.

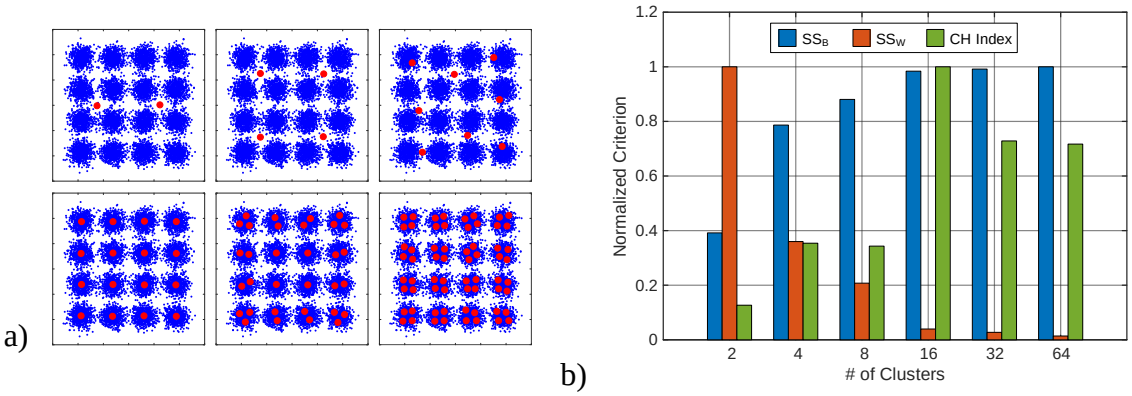

Fig. 12. a) Example of *k*-means clustering with different number of clusters for a simulated 16QAM constellation and (b) associated classification criterions normalized to 1. The CH index peaks at the correct cluster size, unlike the other cluster variance parameters.

3.2.1.11 Constellation Shape Estimation

The cluster means from the correct clustering are deemed the constellation for DD-LMS equalization [62], which is applied to the signal output from CPR, to correct for any residual channel filtering effects, not accounted for by polarization demultiplexing/filtering.

Clustering is applied a final time to the DD-LMS equalizer output to more accurately estimate the constellation shape.

3.2.1.12 Bit Rate Estimation

Because of the fine resolution of distribution matchers in systems with probabilistic shaping [7], estimating the exact coding rate is infeasible, thus, this architecture seeks to

simply estimate the net data rate of a received waveform. This is done by calculating the entropy, or self-information, of the received symbols, with the symbol decision boundaries defined as the Voronoi boundaries in Euclidean space from the previously estimated constellations. Entropy, in bits, is calculated as:

$$\mathrm{H}(X) = -\sum_{i=1}^{n} \mathrm{P}(x_i) \log_2 \mathrm{P}(x_i) \tag{60}$$

where X is a discrete random variable with possible values (symbols) $\{x_1, \dots, x_n\}$ [89]. The net data rate is then estimated as the product of the baud rate with the estimated information per symbol:

$$\text{Net Bit Rate} = -f_b \cdot \sum_{i=1}^{M} \frac{N_i}{N} \log_2 \frac{N_i}{N} \tag{61}$$

where N is the total number of symbols observed and N_i is the number of symbols in the ith cluster.

3.2.2 Experimental Setup

Fig. 13 shows the experimental setup (similar to Isautier et al. [105]). Waveforms are digitally generated by a 92-GS/s DAC (32-GHz bandwidth) and amplified by a quad driver before electro-optic conversion onto a 1550-nm optical carrier by a dual-polarization Mach-Zehnder modulator (DP-MZM). The optical signal is amplified by an erbium-doped fiber amplifier (EDFA) before back-to-back, fiber span (90-km SSMF at 0-dBm launch power), or long-haul (810-km SSMF at 0-dBm launch power) transmission. 810-km transmission was implemented by three passes through a recirculating loop comprised of three fiber spans. Data center interconnection, which has a maximum fiber distance of ~100-km, is the primary use case for high-baud rate 64QAM [83] and is thus the target

fiber distance for span transmission. ASE noise loading is applied after transmission and before optical filtering using a wavelength-selective switch (WSS), with 50-GHz channel spacing. The filtered optical signal is passed to a coherent receiver and subsequently digitized by an 80-GS/s real-time oscilloscope. Offline processing is applied to the captured waveforms within MATLAB.

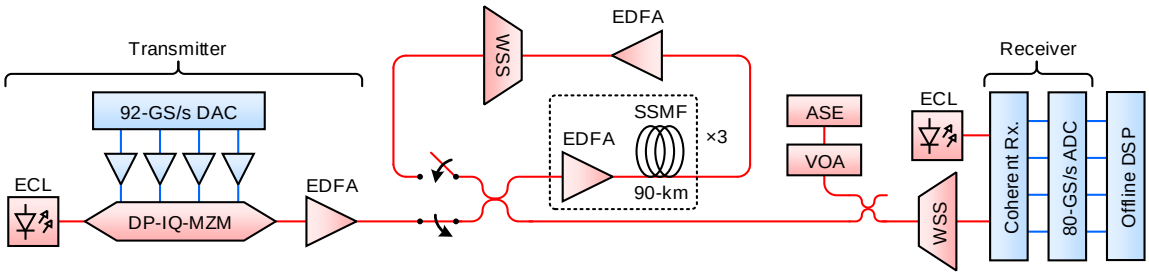

Fig. 13. Block diagram of experimental setup with recirculating loop. Red traces are optical and blue traces are electrical.

Waveforms are generated digitally with a variety of modulation parameters (all dual-polarization and at 32-Gbd), to validate the functionality of the classification architecture. The values of the experimental parameters are listed in Table 2.

Table 2 – Experimental Setup Parameters (*large waveform set).

Parameter	**Value**
Format	QPSK*, QPSK-8QAM, 8QAM*, 8QAM-16QAM, 16QAM*, 16QAM-32QAM, 32QAM*, 32QAM-64QAM, 64QAM*
Baud Rate	32-Gbd*
Fiber Distance	0-km*, 90-km, 810-km
Polarizations	2*
# of Waveforms Captured	10, 500*

Table 2 continued

# of Symbols for Estimation	30,000*
Pulse Shape	RC, RRC*
Pulse Shape Roll-off	0.05, 0.1*, 0.2, 0.3, 0.4, 0.5, 0.6, 0.7, 0.8, 0.9, 1.0
Constellation Shapes	Square*, Hex, Circle
H	5.5, 5.6, 5.7, 5.8, 5.9, 6.0
Classification Error Resolution	5×10^{-2}, 1×10^{-3}*

3.2.3 Experimental Results

The results shown in the following sections cover unique function blocks not already covered in the literature, thus baud rate, CD, and frame size estimation are not shown below. The performance of each function block is demonstrated with the proper parameters fixed in the preceding classification blocks so that results are not obfuscated by the operation of the preceding blocks.

3.2.3.1 Pulse Shape Estimation

Fig. 14 displays how well pulse shape roll-off estimation operates for 32-Gbd DP-64QAM after 90-km transmission at 20-dB OSNR. Results are shown for both 50- and 100-GHz WSS bandwidths. 20-dB was the lowest OSNR investigated, with higher OSNRs exhibiting the same performance.

Because roll-off estimation primarily depends on the spectral shape of the received waveform at frequencies near the baud rate, the estimation is best at lower roll-offs and worse at higher roll-offs, particularly in the presence of lowpass filtering. For 50-GHz WSS channel spacing, the roll-off is consistently underestimated for roll-offs larger than 0.4, whereas for 100-GHz WSS channel spacing, the roll-off is only underestimated for roll-

offs larger than 0.6, with estimates only deviating by ~0.1. For RC pulse shaping with a 0.05 roll-off factor the RRC estimate appears to overestimate the roll-off by a factor of 2, but this is due to using the incorrect shape fit. For all roll-off factors and shapes investigated, the estimation error is well within the bounds of demodulation of the QAM signals of interest [90].

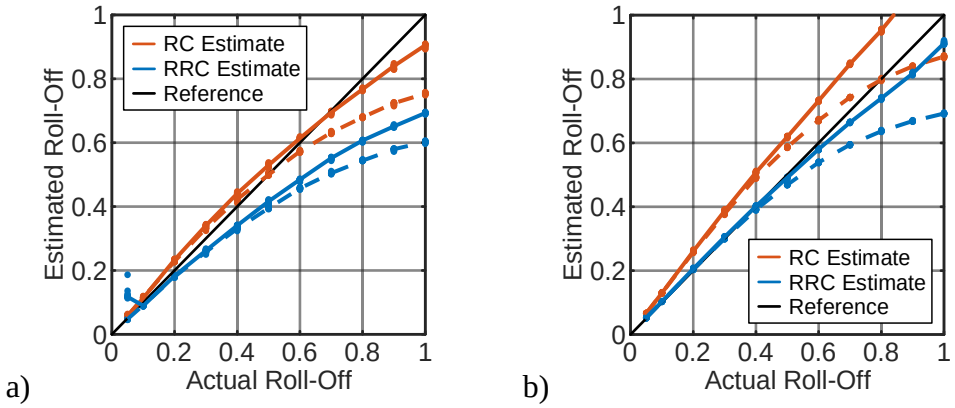

Fig. 14. Experimental pulse shape roll-off estimation of 32-Gbd DP-64QAM after 90-km transmission. (a) RC and (b) RRC transmitted pulse shaping. Dotted traces correspond to the median estimate for 50-GHz channel filtering and solid traces for 100-GHz channel filtering. Estimate points also shown. All traces are at 20-dB OSNR.

3.2.3.2 Rotational Symmetry Estimation

Fig. 15 shows the performance of rotational symmetry estimation for back-to-back transmission of conventional modulation formats, with and without geometric shaping. Except for hex-64QAM, the rotational symmetry order of all formats and constellation shapes is perfectly classified over the OSNRs investigated. Hex-64QAM has at least 90% classification accuracy over the OSNRs investigated and is only misclassified as 4th-order rotationally symmetric.

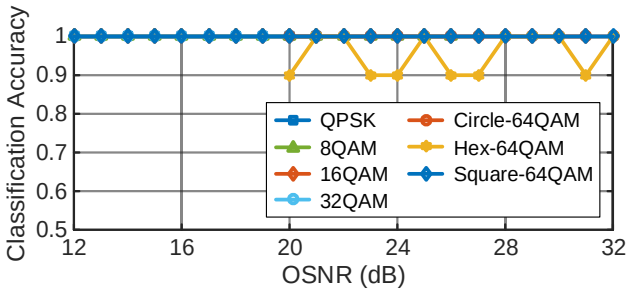

Fig. 15. Classification accuracy of rotational symmetry order for various formats and constellation shapes after back-to-back transmission. All formats and shapes perfectly classified, except for hex-64QAM.

3.2.3.3 Format Classification

Fig. 16 shows the performance of classifying dual-polarization TD-HMF waveforms at 32-Gbd in back-to-back transmission. Formats comprised of only QPSK or 8QAM achieve greater than 95% classification accuracy above 12-dB OSNR. Formats comprised of only 8-, 16-, or 32QAM achieved greater than 95% classification accuracy above 21-dB OSNR. Formats involving 64QAM achieved greater than 95% classification accuracy by 26-dB OSNR.

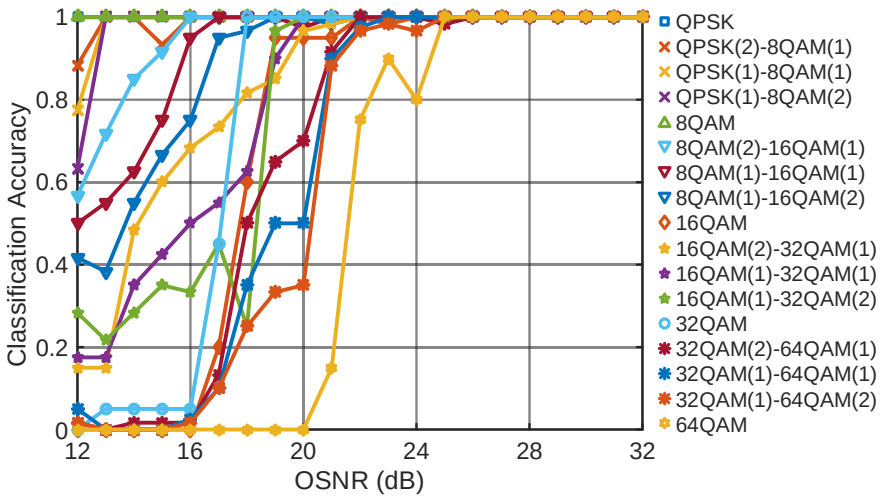

Fig. 16. Performance of TD-HMF classification after back-to-back transmission.

Table 3 is the confusion matrix for conventional and hybrid format classification in back-to-back transmission for OSNRs that yield theoretical BERs between 10^{-2} and 10^{-3}.

The matrix lists the probability of an actual constellation being correctly classified or incorrectly classified as another constellation; it includes symbols of the same constellation shape from both conventional QAM and hybrid QAM, which have the same classification performance. Greater than 97% accuracy is demonstrated for all format combinations. 64QAM has the lowest classification accuracy of 97.8% with majority of misclassification to 16QAM, the next lowest order square-QAM. 16QAM has the next lowest classification accuracy of 97.9% with majority misclassification to QPSK, the next lower order square-QAM.

Table 3 – Confusion matrix after back-to-back transmission

		Actual				
		QPSK	8QAM	16QAM	32QAM	64QAM
Predicted	QPSK	100.0%	0.4%	1.5%	0.0%	0.0%
	8QAM	0.0%	99.4%	0.3%	0.0%	0.3%
	16QAM	0.0%	0.2%	97.9%	0.5%	1.9%
	32QAM	0.0%	0.0%	0.3%	99.5%	0.0%
	64QAM	0.0%	0.0%	0.0%	0.0%	97.8%

Fig. 17 shows the classification error for 32-Gbd M-QAM formats after back-to-back transmission (using parameters in Table 2 for the large waveform set experiment). Error bars are from 95% confidence Wilson score intervals. The minimum achievable, non-zero classification error for this experiment is 10^{-3}. QPSK did not yield any classification errors for OSNRs at or above 10-dB OSNR and is thus not shown. 8QAM, 16QAM, and 32QAM did not yield any classification errors above 12-, 15-, and 21-dB OSNR, respectively. High classification accuracy is clearly achieved and confirms the results of

the small waveform set experiments. 64QAM achieved a minimum classification error of 0.023 at 27-dB OSNR due to the experimental noise floor not seen in the other formats.

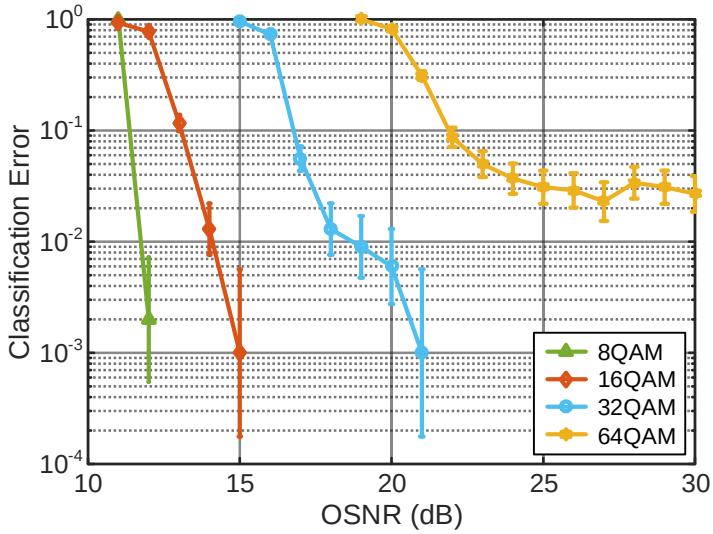

Fig. 17. Classification error (with 95% confidence Wilson score intervals) for back-to-back transmission of 32-Gbd QAM formats, from large waveform set experiment.

Fig. 18 shows the classification of hybrid formats after 90-km transmission, using a subset of the waveforms in the back-to-back transmission. Similar trends are exhibited, though 32- and 64QAM exhibit worsened classification, requiring 2- and 4-dB higher OSNRs, respectively, for the same classification probability (compared to back-to-back transmission).

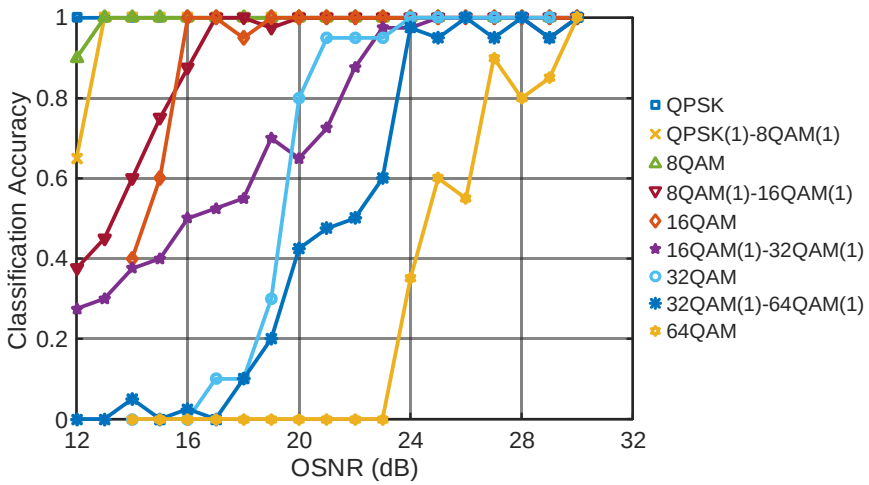

Fig. 18. Performance of TD-HMF classification after 90-km transmission. QPSK is nearly 1 for OSNRs greater than 12-dB.

Table 4 is the confusion matrix for conventional and hybrid format classification after 90-km transmission for OSNRs that yield theoretical BERs between 10^{-2} and 10^{-3}. The lower-order formats (QPSK, 8QAM, and 16QAM), exhibit greater than 99% classification rates, whereas 32QAM and 64QAM only exhibit greater than 91% and 70% accuracy, respectively. The increased misclassification shown in the confusion matrix arises due to link penalty, which is similarly seen in the measured BER when transitioning between back-to-back and 90-km transmission: the range of OSNRs in the confusion matrix do no account for this penalty. 32QAM and 64QAM are both most commonly misclassified as 16QAM.

Table 4 – Confusion matrix after 90-km transmission

		Actual				
		QPSK	8QAM	16QAM	32QAM	64QAM
Predicted	QPSK	100.0%	0.0%	0.0%	0.0%	0.0%
	8QAM	0.0%	100.0%	0.4%	1.5%	0.5%
	16QAM	0.0%	0.0%	99.2%	6.6%	28.9%
	32QAM	0.0%	0.0%	0.4%	91.9%	0.0%
	64QAM	0.0%	0.0%	0.0%	0.0%	70.6%

Fig. 19 shows the classification of conventional QAM formats after 810-km transmission in a recirculating loop (3 loops of 3 spans of 90-km of SSMF), to demonstrate long-haul capabilities of the architecture. Only formats with a spectral efficiency at or below 16QAM are used due to OSNR limitations in the experimental setup. Similar trends

are visible as in 90-km transmission, though an additional 2-dB OSNR is required for greater than 90% classification accuracy of 8- and 16QAM.

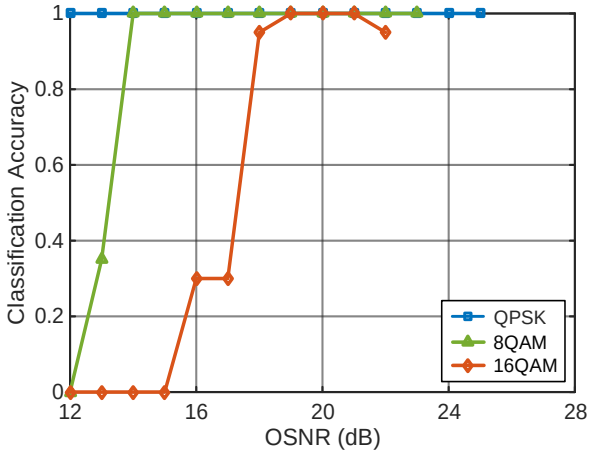

Fig. 19. Performance of QAM classification after 810-km transmission.

Table 5 is the confusion matrix of conventional QAM formats after 810-km transmission for OSNRs that yield theoretical BERs between 10^{-2} and 10^{-3}. Greater than 98% classification accuracy is achieved for all formats investigated.

Table 5 – Confusion matrix after 810-km transmission

		Actual		
		QPSK	8QAM	16QAM
Predicted	QPSK	100.0%	0.0%	0.0%
	8QAM	0.0%	100.0%	1.3%
	16QAM	0.0%	0.0%	98.7%
	32QAM	0.0%	0.0%	0.0%
	64QAM	0.0%	0.0%	0.0%

3.2.3.4 Constellation Shape Estimation

Fig. 20 displays how closely the estimated constellation shape matches the actual constellation shape for dual polarization square-, circle-, and hex-64QAM, in back-to-back and 90-km transmission. The traces correspond to the median of the mean square error of the constellation cluster means. With the average constellation power normalized to one, the mean square error (MSE) is analogous, but not equivalent, to the error vector magnitude (EVM). Because the cluster means average the AWGN on the demodulated waveforms, the MSE metric is much lower than the EVM of the same waveform. The error from clustering is approximately the same across the OSNRs investigated, with additional error at low OSNRs for square-QAM. For context, the theoretical MSE between circle- and hex-QAM is 0.011 and is the lowest off all constellation shapes investigated. Square-QAM has a consistently larger error than circle- or hex-QAM, due to the high peak-to-average power ratio (PAPR) of square-QAM. Similar errors are shown for back-to-back and 90-km transmission, with square-QAM exhibiting a larger error only at lower OSNRs. Though constellation shape estimation can very closely approximate the transmitted constellation, no assumptions are made about the possible, exact constellation structures. Improved demodulation performance can be achieved if a library of possible constellation shapes is known.

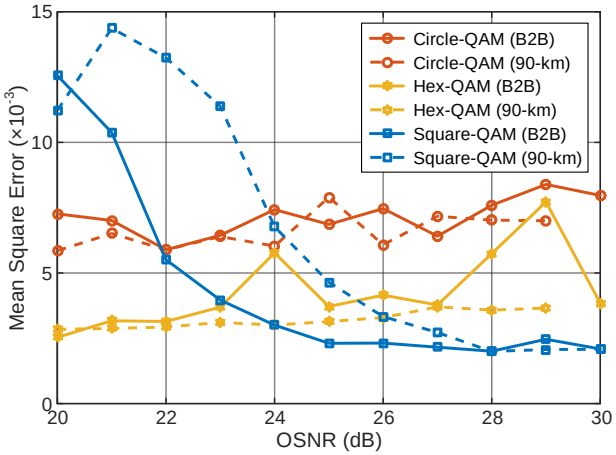

Fig. 20. Performance of constellation shape estimation of DP-64QAM after back-to-back (solid traces) and 90-km (dashed traces) transmission, characterized by the median of the mean square error of the constellation estimate. The median is calculated from 10 constellation estimates.

3.2.3.5 Bit Rate Estimation

Fig. 21 shows the accuracy of rate estimation for 32-Gbd DP-PS-64QAM, with bit rates ranging from 352- to 384-Gbps, after 90-km transmission. The constellation distributions are shaped using Maxwell-Boltzmann distributions with different bit rate versus average energy trade-offs [89]. Dotted traces correspond to actual transmitted bit rates, whereas solid traces are the estimated bit rates. Purple traces correspond to uniformly distributed DP-64QAM; all other colors correspond to increased shaping, and thus lower bit rates.

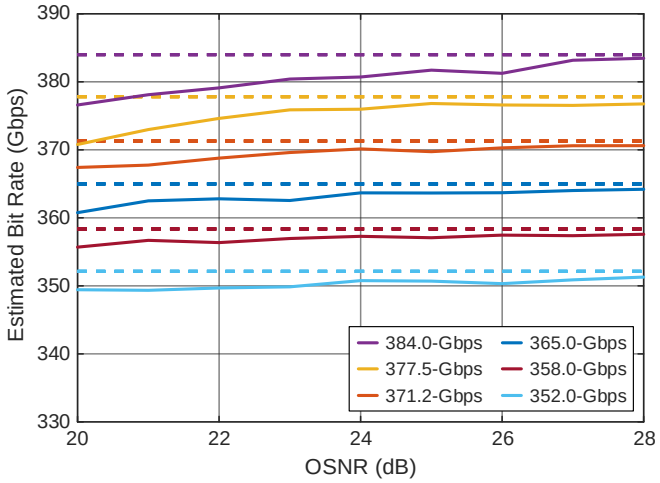

Fig. 21. Performance of bit rate estimation after 90-km transmission. Dotted traces correspond to transmitted bit rate and solid traces correspond to estimated bit rate. The transmitted bit rate is constant with respect to OSNR.

At OSNRs greater than 26-dB, rate estimation is relatively accurate, while lower OSNRs result in consistent underestimation of the bit rate due to information loss over the channel with increasing ASE. As the actual rate decreases, performance of rate estimation worsens, due to fewer symbols occurring at the periphery of the constellation, which negatively impacts the performance of constellation clustering. There is a negligible difference between back-to-back and 90-km transmission for bit rate estimation.

3.2.4 Comparison to Other Architectures

Hui et al. [80] demonstrated an HOCC-based modulation format identification using a binary decision tree, after compressed sensing. Simulations demonstrated greater than 99% accuracy above 10-dB OSNR for 28-Gbd 32QAM.

Hao et al. [66] presented an autonomous receiver for format recognition using probabilistic neural networks with input features derived from Stoke space parameters. Experimentally, it demonstrated perfect classification of 28-Gbd DP-QPSK and DP-16QAM at OSNRs of 12-dB and at least 19-dB, respectively. Comparably, the architecture

presented in this paper exhibited perfect classification of 32-Gbd DP-QPSK at 11-dB, and 95% classification accuracy of 32-Gbd DP-16QAM at 19-dB.

Isautier et al. [105] presented an architecture for the classification of TD-HMFs comprised of BPSK, QPSK, 8QAM, or 16QAM (all at ~31.5-Gbd). QPSK-8QAM formats were classified with at least 90% accuracy above 13-dB OSNR, and 8QAM-16QAM above 15-dB OSNR. The architecture presented in this paper demonstrated very similar performance for both types of hybrid formats (these are the only waveform types investigated in both papers).

There are a variety of autonomous receivers in the literature, with different classification purposes and employing different means, and a subset of these receivers have been addressed in this paper. Most seek to classify modulation formats with conventionally shaped, uniformly distributed constellations; though some of these receivers' algorithms would feasibly work under non-conventional shaping and non-uniform distribution conditions. Only a few publications have addressed the classification of TD-HMFs and even fewer have addressed the classification of probabilistically shaped formats.

3.3 Nonlinear Compensator

Higher spectral efficiency modulation formats including DP-32, 64QAM, and beyond are a candidate solution to increase capacity of WDM links, though they face increased implementation challenges; digital-to-analog and analog-to-digital converters (ADCs) require high effective number of bits (ENoB), while RF components, such as modulator drivers or receiver transimpedance amplifiers (TIAs), are required to be highly linear.

Equalization of nonlinearities has been applied to QAM signals [91] to compensate high power amplifier nonlinearities (primarily a transmitter-side solution). Predistortion of MZMs with finite extinction and branch asymmetry (prevalent in InP-based modulators) has been applied by mapping the transmitted signal to distorted constellations [92], by cascaded LMS-based equalizers [93], and by adjusting the reference constellation in demodulation [94]. Correction of fiber nonlinearities (e.g. SPM) has also been applied in post-processing whether through digital back propagation [95] or frequency-domain Volterra series nonlinear equalization [96].

Here we describe and demonstrate a simple receiver-side adaptive nonlinear compensator (NLC) to equalize arbitrary component nonlinearities, including those introduced by electronic amplifiers and MZMs. The method is independent of modulation format. We report experimental results of the algorithm performance for 16-Gbd DP-64QAM in back-to-back transmission and after 90-km transmission over SMF, with nonlinear penalties introduced primarily in the receiver's TIAs.

3.3.1 Procedure

The NLC is implemented after carrier phase recovery and is instantiated as a complex least-mean square (LMS) Hammerstein equalizer (Fig. 23) [62,102]. The memoryless polynomial description is a joint function of the I- and Q-channels, including even and odd terms, enabling an exhaustive compensator of the effects from various sources (likely dominated by signal compression). Letting $a_{i,q}$ be the scalar multiplier of the $x_I^i x_Q^q$ term, the output of the nonlinear block is:

$$y = a_{1,0}x_{\mathrm{I}} + ja_{0,1}x_{\mathrm{Q}} + a_{2,0}x_{\mathrm{I}}^2 + ja_{1,1}x_{\mathrm{I}}x_{\mathrm{Q}} + a_{0,2}x_{\mathrm{Q}}^2 + a_{3,0}x_{\mathrm{I}}^3 + ja_{2,1}x_{\mathrm{I}}^2x_{\mathrm{Q}} + a_{1,2}x_{\mathrm{I}}x_{\mathrm{Q}}^2 + \cdots \tag{62}$$

Coefficient optimization for the polynomial and FIR descriptions are based on the method of steepest descent and result in:

$$w^{(n+1)} = w^{(n)} + 2\mu_{\mathrm{L}}ey^* \tag{63}$$

$$a_{i,q}^{(n+1)} = a_{i,q}^{(n)} + \mu_{\mathrm{NL}}x_{\mathrm{I}}^i x_{\mathrm{Q}}^q \begin{cases} (e^*w^{\mathrm{T}} + ew^{\mathrm{H}}) & , q \text{ is even} \\ j(e^*w^{\mathrm{T}} - ew^{\mathrm{H}}) & , q \text{ is odd} \end{cases} \tag{64}$$

where μ_{L} and μ_{NL} are the linear and nonlinear convergence factors and n is the sample index.

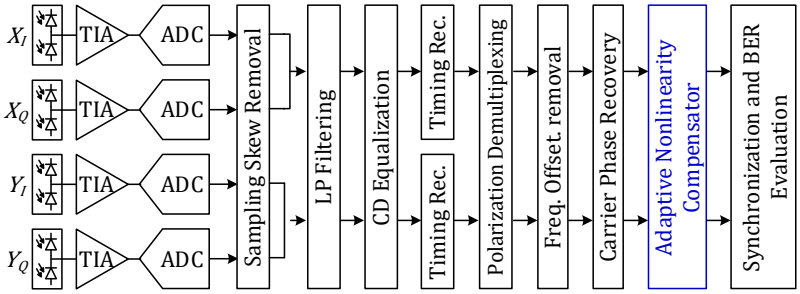

Fig. 22. Block diagram of receiver-side DSP with equalizer that includes a complex least-mean square Hammerstein equalizer.

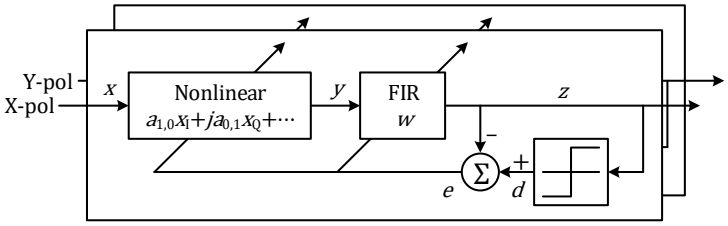

Fig. 23. Block diagram of nonlinearity compensator with joint I-Q linearization including even and odd terms.

3.3.2 Experimental Results

The experimental setup was similar to the one shown in Fig. 4, though with a 64-GS/s DAC. The NLC was applied to signals detected with the coherent optical receiver with TIAs. Within the Hammerstein NLC the polynomial included even and odd terms up to 7^{th}-order and the FIR filter contained 35 tap weights. Small nonlinear convergence factors were utilized; the slow update rate ensured stable performance. The updates rates are consistent with the slowly varying nonlinearities of the electronic amplifiers.

The NLC showed good performance improvement at relatively high OSNRs for back-to-back transmission. Equalized data from the coherent receiver with TIA yields a noise floor approaching that of the receiver without TIAs (minimal nonlinear penalty). Similar results were found for 90 km SMF transmission, though not displayed. Fig. 4 shows the equalized constellation when NLC is not and is applied: the latter is clearly squarer, though the noise distributions about the clusters are not uniform, likely yielding a slight penalty.

Fig. 25 shows BER vs. OSNR performance after back-to-back and 90-km transmission. The demodulation was performed over 10 discontinuous waveforms, each containing 100,000 samples/polarization (20,000 symbols/polarization). The coherent receiver without electrical amplification served as a reference with nonlinear distortion being quasi-negligible. Nonlinearities introduced by the TIAs of the second coherent receiver degraded the performance of the transmission. The performance of this post-compensator may not be optimum in a non-dispersion-managed link wherein chromatic dispersion (CD) compensation is implemented as a digital filter before the nonlinear equalizer. Ideally, an NLC would be placed immediately after the ADC (and compressive

TIA) to equalize the nonlinear and linear impairments in the opposite order they were introduced to the signal, the difficulty is in the update of the equalizer.

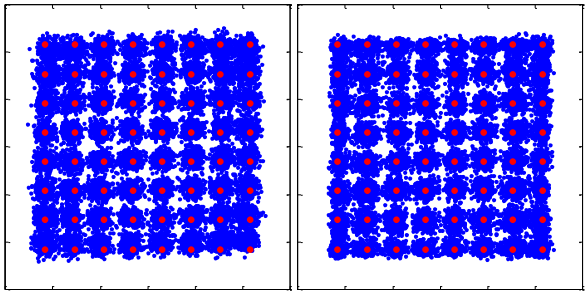

Fig. 24. 16-Gbd DP-64QAM output constellation after linear equalization (left) and NLC (right), where OSNR = 39 dB.

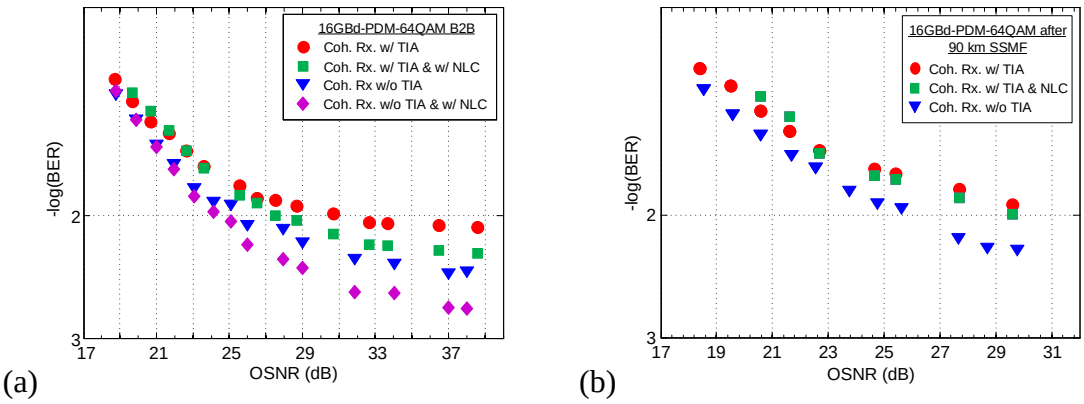

Fig. 25. Experimental BER performance of 16-Gbd DP-64QAM with nonlinear compensator after (a) back-to-back and (b) 90-km SSMF transmission. NLC comprised of 7th-order polynomial (even and odd terms) and 35 tap FIR filter.

CHAPTER 4. MULTI-CARRIER BLIND CLASSIFICATION

OFDM is employed extensively in wireless communication networks to reduce receiver side computational complexity, improve tolerance to fading, improve spectral efficiency, and ease synchronization; it is also being considered for 5G systems [103]. Traditionally, communication links operate with shared knowledge of modulation parameters, here we focus on developing a smart receiver that can identify and demodulate OFDM signals without a priori knowledge. Motivation for autonomous receivers lies in network monitoring and diagnostics and recovery from failures. Photonic-assisted wireless links exploit the low-loss characteristics of optical fiber and high-bandwidth photonic components to offer multi-octave, flexible signal generation and transport with large available instantaneous bandwidths [104]. These characteristics synergize well with the flexibility of OFDM waveform design.

This chapter presents a method for the identification of general OFDM symbol parameters and frame structures, with experimental validation after photonic-assisted wireless link transmission; single-carrier constellation shape identification techniques can be applied for further classification [105].

4.1 Architecture

Fig. 26 shows a high-level block diagram of the blind OFDM demodulator architecture, with black elements corresponding to a conventional demodulator and colored elements corresponding to blind classification DSP blocks. A spectral monitoring determines coarse estimates of the received waveform necessary for the cyclostationarity

(CS) test to accurately estimation the OFDM modulation parameters. A constellation classification block determines the order of the modulation format.

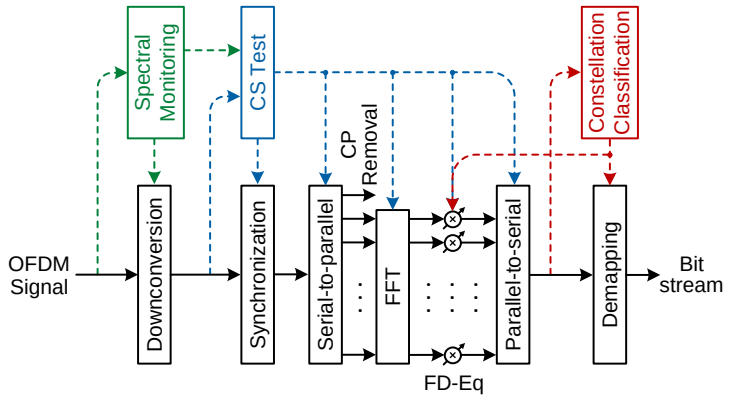

Fig. 26. High-level block diagram of blind OFDM demodulator.

4.1.1 Spectral Monitoring

The spectral monitoring block's purpose is to estimate the center frequency of the received waveform for digital downconversion and the bandwidth as an initial estimate of the signal baud rate. Initially, a naïve spectral monitoring block was developed. The block first determined if the received waveform was baseband or centered on an IF. This was achieved by determining the number of 3-dB points in the received spectra: if only two are present, it is considered to be at baseband, if four are present, it is considered to be on an IF. A "center-of-gravity" technique was utilized to estimate the center frequency. For an IF waveform only positive frequencies are considered and the IF is estimated as:

$$f_{\mathrm{IF}} = \frac{\sum_{f=0}^{f_s/2} f \cdot |R(f)|^2}{\sum_{f=0}^{f_s/2} |R(f)|^2} \tag{65}$$

where $R(f)$ is the received waveform spectra and f_s is the digitizer sample rate. For a baseband waveform the center frequency is estimated as:

$$f_{\mathrm{BB}} = \frac{\sum_{f=-f_s/2}^{f_s/2} f \cdot |R(f)|^2}{\sum_{f=-f_s/2}^{f_s/2} |R(f)|^2} \tag{66}$$

From this estimate, the 3-dB points in the PSD were determined, and the difference was considered the signal bandwidth. This method is sufficient for cases wherein the channel is generally flat, but performance suffers greatly under non-flat channel conditions, particularly when the slope of the channel has a steep average slope caused by one-sided bandwidth roll-offs of components. Thus, an alternative spectral monitoring block was developed that iteratively estimates the passband as a polynomial (in this case a line) and the corresponding relative 3-dB points. The method iterates until the 3-dB points converge, at which time the center frequency and bandwidth are estimated as the mean and different of the 3-dB points, respectively.

Fig. 27 shows an example output of the spectral monitoring block for a 3-Gbd OFDM on a 3-GHz IF. The blue trace corresponds to the signal PSD, note the 10-dB drop across the passband, which would result in a drastic underestimation following the naïve approach. The red trace corresponds to the linear fit of the passband after convergence; due to the PSD being on a log-scale the trace is curved. The black traces correspond to the 3-dB points and the center frequency. Frequency and bandwidth estimates have ~1% accuracy.

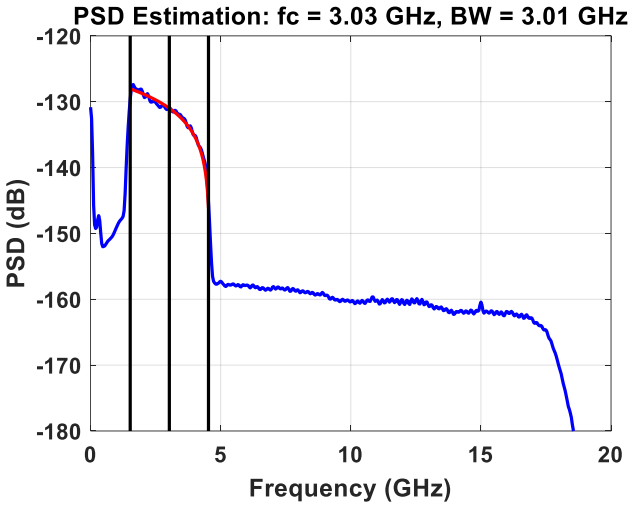

Fig. 27. Output of spectral monitoring block for 3-Gbd OFDM at a 3-GHz IF

4.1.2 Cyclostationarity Test

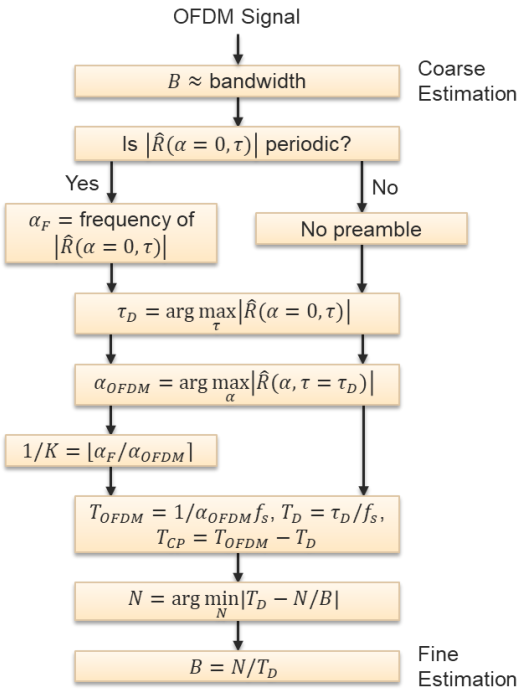

Fig. 28. Block diagram of CS test

The CS test comprises most of the computational load in the blind OFDM architecture and is discussed here. A block diagram of the CS test is shown in Fig. 28. The

cyclic autocorrelation function (CAF), or the second-order cyclic cumulant estimator, is the primary tool used in the CS test and is defined as:

$$\mathcal{R}(\alpha,\tau) = \frac{1}{T}\sum_{k=0}^{T-1} x(k+\tau)x^*(k)e^{-j2\pi\alpha k} \tag{67}$$

where α is the normalized cyclic frequency, τ is the delay, and T is the integration interval. Its magnitude is independent of frequency and phase offset and can thus be effective amid high phase noise. Traditionally the CAF is used to estimate the baud rate of a single-carrier signal, but it has also been shown that OFDM symbol parameters (i.e. T_{OFDM}, T_D, T_{CP}, and N) can be estimated with the CAF [68], starting with an estimate of the baud rate (e.g. the signal bandwidth), normalized data duration:

$$\tau_D = \arg\max|\mathcal{R}(\alpha = 0,\tau)| \tag{68}$$

and normalized OFDM symbol frequency:

$$\alpha_{OFDM} = \arg\max_{\alpha}|\mathcal{R}(\alpha,\tau_D)| \tag{69}$$

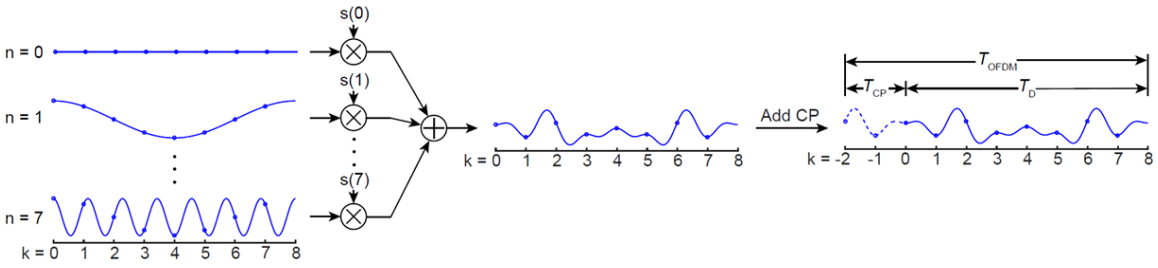

Fig. 29. Synthesis of an CP-OFDM symbol

The peak in the autocorrelation, $\mathcal{R}(\alpha = 0,\tau)$, arises due to the cyclic prefix (CP) repeating for every OFDM symbol. To visualize this, Fig. 29 shows the synthesis of a single OFDM symbol. QAM symbols are modulated onto sinusoids with unique

frequencies and then combine resulting in the OFDM data. The CP (last N_{CP} samples of the OFDM data) is then prepended to the OFDM data resulting in the OFDM symbol.

Fig. 30 is an ideal figure showing the projections of the CAF of traditional CP-OFDM. The top plot simply shows the autocorrelation with a peak at τ_D corresponding to the time-delay between repeated cyclic prefixes. The bottom plot shows where peaks occur in the CAF, at $\tau = \tau_D$ and $\alpha = k\alpha_{OFDM}$.

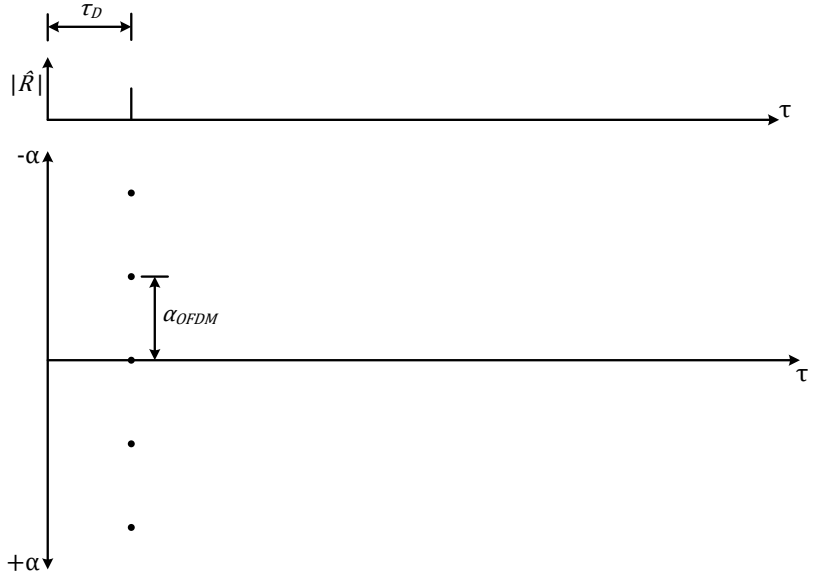

Fig. 30. Ideal projections of the CAF of CP-OFDM without preambles

To improve efficiency, the computational complexity of the CAF can be reduced by using the FFT. Also, the CAF at α=0 can be calculated over a limited range defined by:

$$\tau \in \left[\frac{kf_s N_{min}}{BW}, \frac{kf_s N_{max}}{BW}\right] \tag{70}$$

where N_{min} and N_{max} are the bounds of N.

It has also been shown when a preamble is included the CAF has a richer structure which can be used to discriminate between OFDM protocols (e.g. WiMax and LTE [67]).

In this section we discuss how not only OFDM symbol parameters, but also how frame parameters (i.e. preamble duty cycle) can be estimated using a similar approach.

Preambles are periodically prepended to a group of OFDM symbols, resulting in what we call a frame (Fig. 31a). Preambles are utilized for timing synchronization and channel equalization and can exhibit different structures depending on the application. Fig. 31b shows some possible preamble structures, all which contain internal repetition related to half the data duration.

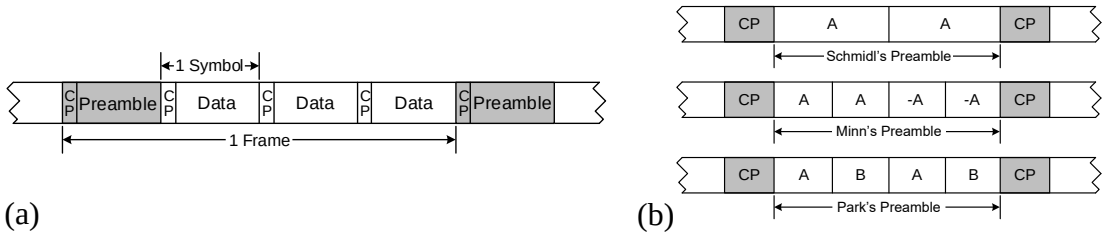

Fig. 31. Structure of OFDM-CP (a) frame and (b) preamble

Due to additional repetitions within an OFDM signal caused by the preamble structure, the autocorrelation of an OFDM signal with framing exhibits additional features and can be seen in Fig. 32. Not only are the peaks from OFDM without preambles present, but many more peaks as well. Peaks due to the preamble occur at:

$$\tau = K\tau_{OFDM}m \pm \frac{\tau_D}{2} \tag{71}$$

$$\alpha = \frac{\alpha_{OFDM}}{K}n \tag{72}$$

where $\frac{1}{K}$ is the inverse of the preamble duty-cycle and m and n are integers.

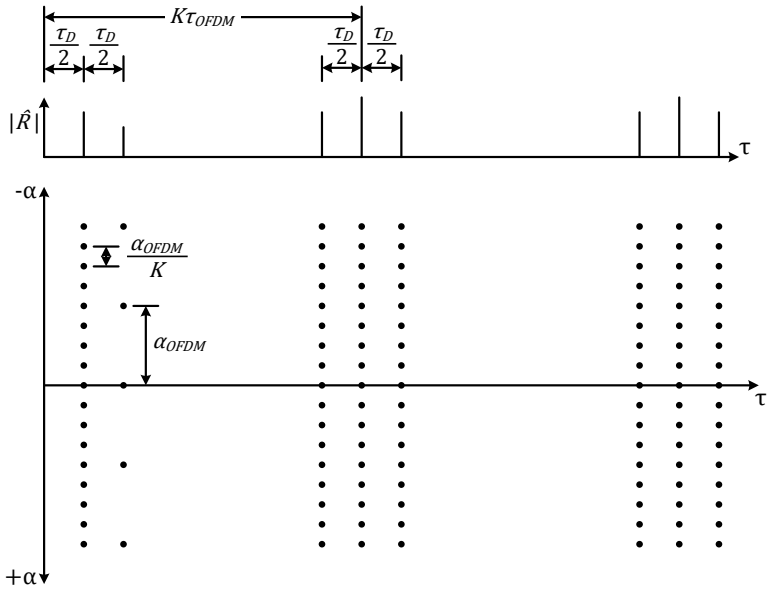

Fig. 32. Ideal projections of the CAF of CP-OFDM with preambles

With this knowledge, if the autocorrelation exhibits periodicity then the signal is considered to contain preambles and the rate at which they occur is considered the normalized frame frequency:

$$\alpha_F = (K\tau_{OFDM})^{-1} \tag{73}$$

With the normalized frequencies and the normalized data duration known, the actual data duration, OFDM symbol duration, and CP duration can be estimated.

$$T_{OFDM} = (\alpha_{OFDM} f_s)^{-1} \tag{74}$$

$$T_D = \tau_D / f_s \tag{75}$$

$$T_{CP} = T_{OFDM} - T_D \tag{76}$$

With the durations estimated, the number of subcarriers can be estimated such that there is a minimum error between the measured OFDM data duration and the OFDM duration computed form the OFDM bandwidth:

$$N = \arg\min_{N} \left| T_D - \frac{N}{B} \right| \tag{77}$$

Finally, with an accurate estimate of the subcarriers and the data duration the signal baud rate can be estimated as $B = N/T_D$, instead of proxying the bandwidth.

4.1.3 Constellation Classification

The constellation classification method utilized in this architecture is the *K*-means algorithm, as described in Sec. 3.2.1.9. Other methods can be employed, but *K*-means provides flexibility with regards to non-uniform distributions and geometric shaping compared to other techniques (e.g. higher-order cumulants).

4.1.4 Demodulation

Using the estimated OFDM parameters, non-data-aided synchronization, serial-to-parallelization, the FFT, blind FD-EQ, and serialization are applied. Finally, demapping is applied using the estimated constellation shape.

4.2 Experimental Setup

A photonic frequency transceiver was employed to up- and down-convert IF waveforms optically for wireless transmission. Fig. 33 displays the core architecture of the frequency transceiver, a more detailed description can be found in Hughes et al. [104]. A 24-GS/s AWG with 10-bit resolution output OFDM waveforms centered on a 3-GHz IF, which were then amplified and optically up-converted. Additional SMF was placed between the optical combiner and the PD to enable photonic remoting of the optical IF and 27-GHz carrier. The 30-GHz RF signal at the output of the PD was amplified and radiated using a 25-40-GHz (K_a-band) horn antenna for wireless transmission over a few meters.

The wireless signal is captured by an identical receive antenna before injection into the down-conversion path of the transceiver. A 3-GHz IF was then output from the transceiver and captured by a real-time scope for offline processing.

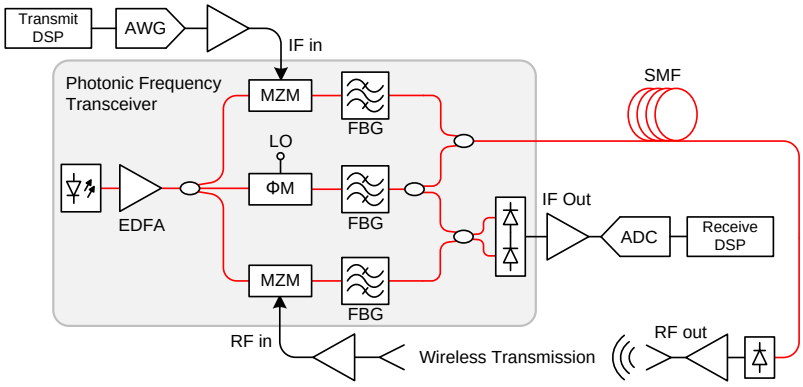

Fig. 33. Experimental setup of wireless photonic link to demonstrate OFDM classification capabilities.

4.3 Experimental Results

OFDM waveforms were generated with a variety of modulation parameters to investigate the performance of the classification DSP for swept values of N, N_{CP}, B, bits/symbol, preamble type, and preamble duty cycle, the performance results of which are shown in Fig. 34 through Fig. 37. The base signal was 3-Gbd CP-OFDM with 256 subcarriers and a CP length of 8, deviations from those modulation parameters were investigated. Fig. 34 shows the probability of correct classification of the number of subcarriers, with N ranging from 16 to 1024. Fewer samples are required to correctly classify lower values of N due to the OFDM symbols being shorter in duration, increasing the number of cyclic prefixes included in the autocorrelation, resulting in better peak estimation.

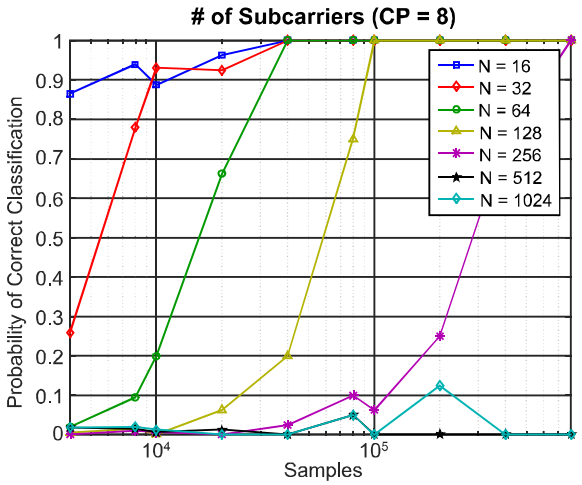

Fig. 34. Probability of correct classification of the number of subcarriers for 3-Gbd QPSK-OFDM with a CP length of 8 symbols

Fig. 35 shows the probability of correct classification for different cyclic prefix lengths, with N_{CP} ranging from 8 to 32. Longer cyclic prefixes increase the number of correlated samples; thus the autocorrelation yields more prominent peaks and higher classification accuracy. Thus, as expected, signals with longer cyclic prefixes demonstrate better classification accuracy with fewer samples.

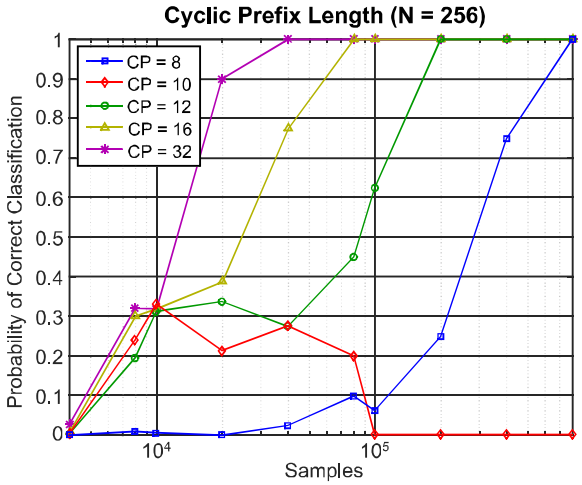

Fig. 35. Probability of correct classification of the cyclic prefix length of 3-Gbd QPSK CP-OFDM waveform with N = 256

Fig. 36 shows the probability of correct baud rate estimation. Performance is relatively equivalent for the baud rates estimated, requiring at least 2×10^6 samples for greater than 50% accuracy.

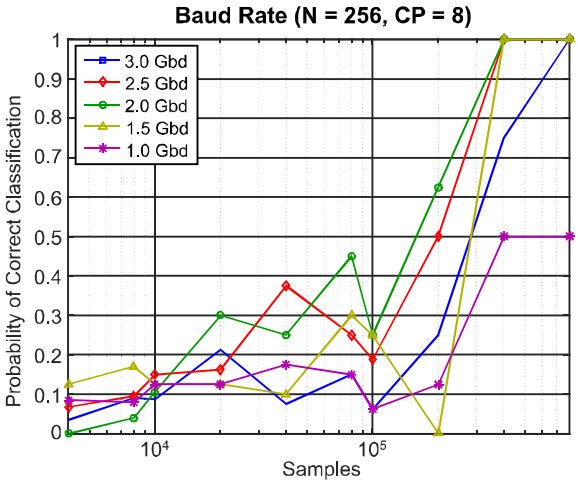

Fig. 36. Probability of correct classification of the baud rate of 3-Gbd QPSK CP-OFDM waveform with N = 256 and N_{CP} = 8

Fig. 37 shows the probability of correct classification of the preamble duty cycle and similarly demonstrates similar performance over different duty cycles. Though, if no preamble is present the architecture perfectly classifies the signal as not containing a preamble over the sample sizes investigated. The magnitude of the CAF for waveforms with the preambles investigated have very similar characteristics, thus the performance of classification is agnostic to preamble type, though this would not be the case if different preambles were used.

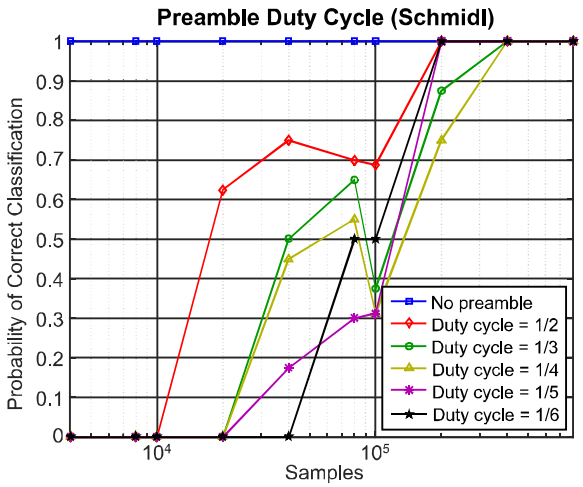

Fig. 37. Probability of correct classification of the preamble duty cycle of 3-Gbd QPSK CP-OFDM waveform with N = 256, N_{CP} = 8, and Schmidl preamble

CHAPTER 5. HIGH-SPEED FIBER-WIRELESS TRANSMISSION

5.1 V-band Fiber-Wireless

5.1.1 Experimental Setup

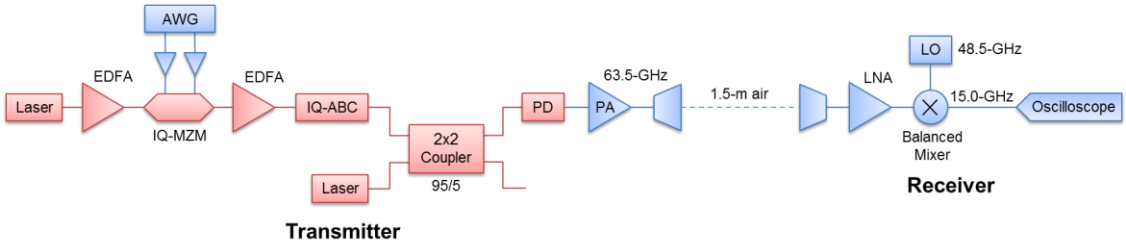

Fig. 38. Block diagram of single-polarization V-band photonic wireless link for OFDM transmission. Red elements are optical components and blue elements are electrical components.

5.1.2 Experimental Results

An investigation was made into the capacity that can be reached for V-band wireless links by multi-carrier modulation. A primary limitation of V-band links is the frequency response of the components employed: for the case of photonic-wireless links, the photodiode can be the primary limiting factor. When operating close to the bandwidth of the components, bit-loading (or entropy-loading) can be applied to yield incrementally more performance. Using the V-band photonic wireless link shown in Fig. 38, bit-loaded 21-Gbd OFDM was transmitted over 1.5-m air, achieving a net data rate of 76.9-Gbps: the highest data rate over a single-polarization/mode V-band photonic wireless link.

Fig. 39 shows the error vector magnitude (EVM) of each of the 256 subcarriers transmitted over the link. The lower numbered subcarriers correspond to higher frequencies and thus have a higher EVM due to the response roll-off of the PD used: to address these low SNR frequencies, QPSK is transmitted on the subcarriers. The other subcarriers are

either 16QAM or 32QAM, depending on the measured subcarrier's EVM. The BER for each format is less than 4×10^{-3}. This architecture can easily be extended to a dual-polarization implementation, doubling the net data rate.

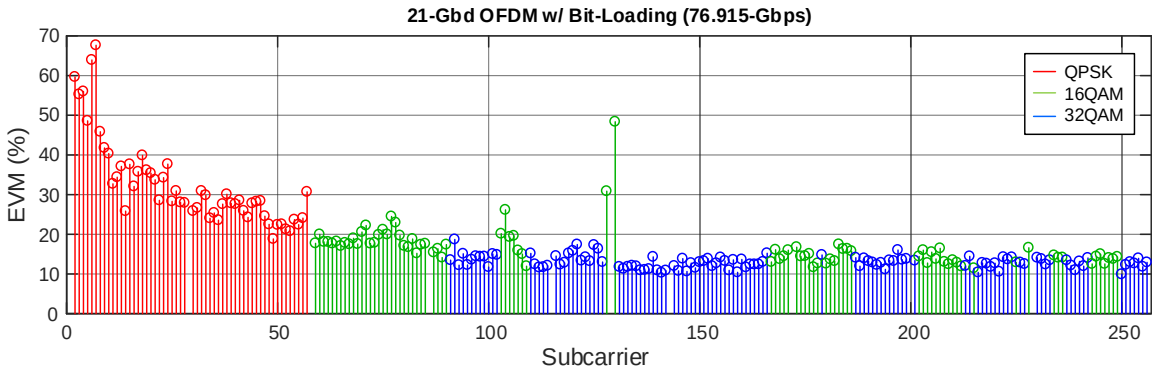

Fig. 39. Performance of bit-loaded 21-Gbd OFDM, for 76.915-Gbps transmission.

5.2 W-band Fiber-Wireless

Though high-speed data transmission can be achieved within the V-band channel, with the component utilized there is a sharp bandwidth cut-off and higher speed cannot be easily achieved. By moving transmission to the W-band the component bandwidth are much larger (up to 45-GHz, ranging from 75- to 110-GHz), which can enable much higher fiber-wireless data rates.

5.2.1 Experimental Setup

The experimental setup for the W-band fiber-wireless link is very similar to the V-band link, though with different components. Most of the optical components can be used for both setups due to their inherently large bandwidths. A 92-GHz separation is applied between both laser sources with one laser modulated with a high-baud rate QAM or OFDM baseband signal, such that a 92-GHz centered signal is generated at the output of the 105-GHz PD. The RF signal is then amplified and transmitted over a 2-to-2.5-m air channel.

An LNA amplifies the received signal before a balanced mixed downcoverts the signal to a 15-GHz IF for digitizing in by a high-speed oscilloscope and subsequent offline DSP.

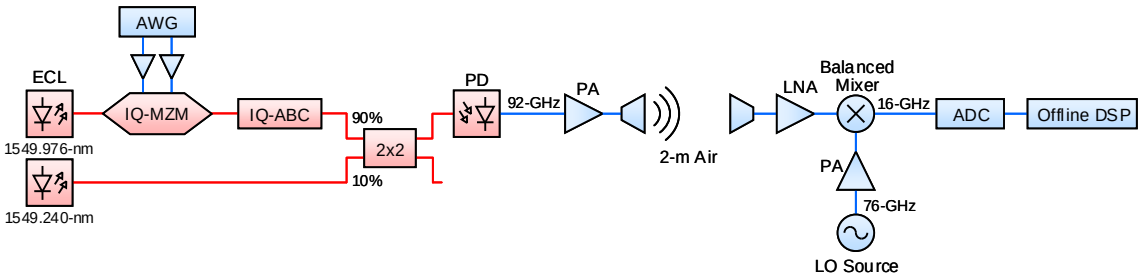

Fig. 40. Experimental of W-band fiber-wireless transmission, with electrical downconversion.

5.2.2 Experimental Results

5.2.2.1 W-band Single-carrier

First, maximum data rates achieved over the channel were determined for single-carrier formats. 24-Gbd QPSK (48-Gbps) was achieved with an EVM of 22.5% and measured BER of 0. A decision-feedback equalizer (DFE) was used but did not yield improved performance over a traditional FFE. The measured spectrum and constellation can be seen in Fig. 41. Harmonics from the balanced mixer can be seen in the spectra that result in a degraded performance. Furthermore, the signal exhibits almost 7-dB fluctuations across the passband. Though there is some flexibility in frequency planning to adjust the placement of the harmonics, this specific orientation provided a trade-off between signal SNR versus in-band interference from LO harmonics.

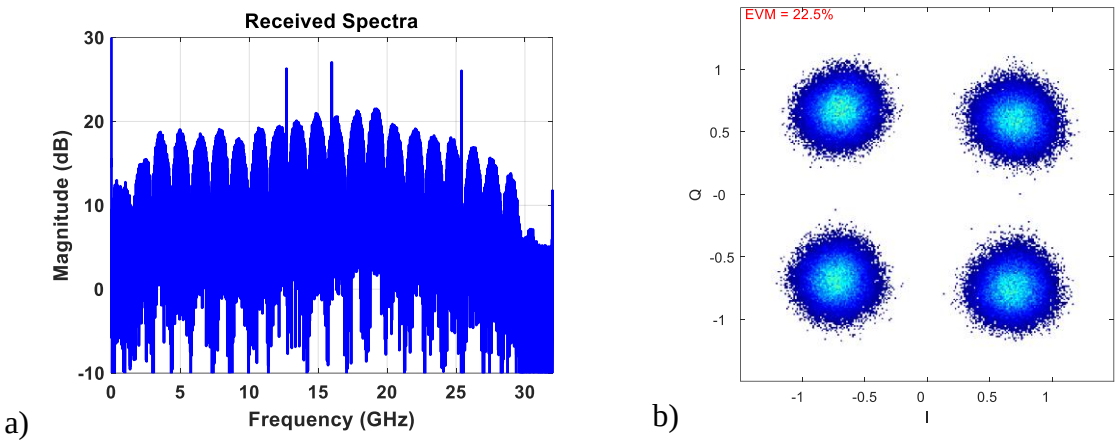

Fig. 41. Measured (a) spectrum and (b) constellation after W-band fiber-wireless transmission of 24-Gbd QPSK.

Because there was sufficient SNR, 16QAM was also transmitted across the link, with the highest speed being 16-Gbd 16QAM (64-Gbps), which yielded an EVM of 22.4% and a measured BER of 1.9×10^{-1}. Similarly, a DFE did not improve performance over the traditional FFE. The measured spectrum and constellation can be seen in Fig. 42. Being over a smaller band than the previously demonstrated QPSK, there is slightly more flexibility in tuning the W-band carrier frequency and the receiver LO frequency. Because of this, a reasonable SNR could be achieved while also having LO harmonics fall outside the passband.

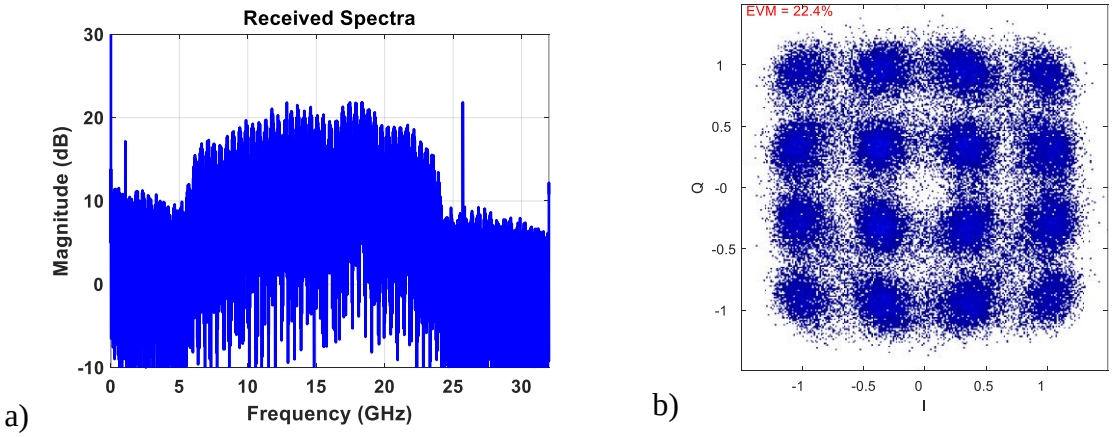

Fig. 42. Measured (a) spectrum and (b) constellation after W-band fiber-wireless transmission of 16-Gbd 16QAM.

5.2.2.2 W-band OFDM

Single-carrier formats are convenient for high-data rate transmission, but multi-carrier formats can enable more flexibility when there is a particularly non-flat channel response or there is strong interference. Because of this, W-band with QPSK, 16QAM, and bit-loading was transmitted across the fiber-wireless link. Table 6 shows the modulation parameters utilized to achieve the high data rate with reasonable BER performance.

Table 6 – Modulation parameters of OFDM waveforms

Format	QPSK	16QAM	Bit-Loaded
Net Rate	43.330-Gbps	57.773-Gbps	73.532-Gbps
OFDM Bandwidth	26-GHz	16-GHz	26-GHz
FFT Length	256	256	256
CP Length	1/32	1/32	1/32
Pilot Carriers	8	8	8
Null Carriers	6	1	6
Preamble Duty Cycle	1/32	1/32	1/32

Fig. 43 shows the EVM by subcarrier and aggregate constellation of 26-Gbd OFDM QPSK which yielded a net data rate of 43.330-Gbps. The average EVM was 18.09% across all subcarriers with an estimated BER of 1.615×10^{-8}. A group of subcarriers were null around the 40^{th} subcarrier to account for interference within the passband. Fig. 44 shows the EVM by subcarrier and aggregate constellation of 16-Gbd OFDM 16QAM which yielded a net data rate of 57.773-Gbps. The average EVM was 17.47% across all subcarriers with an estimated BER of 3.926×10^{-3}.

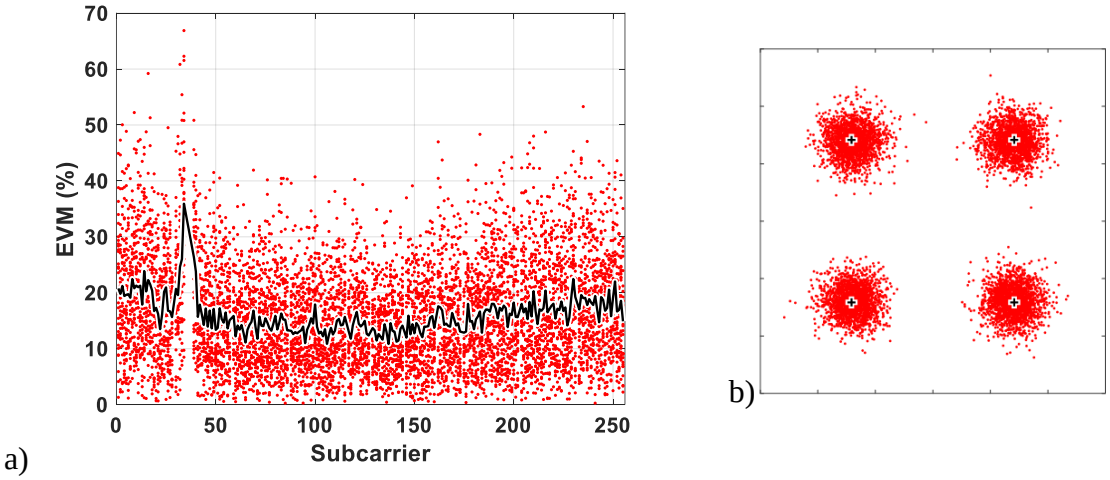

Fig. 43. 26-Gbd OFDM QPSK with net data rate of 43.3-Gbps. a) EVM for each subcarrier and b) aggregate constellation.

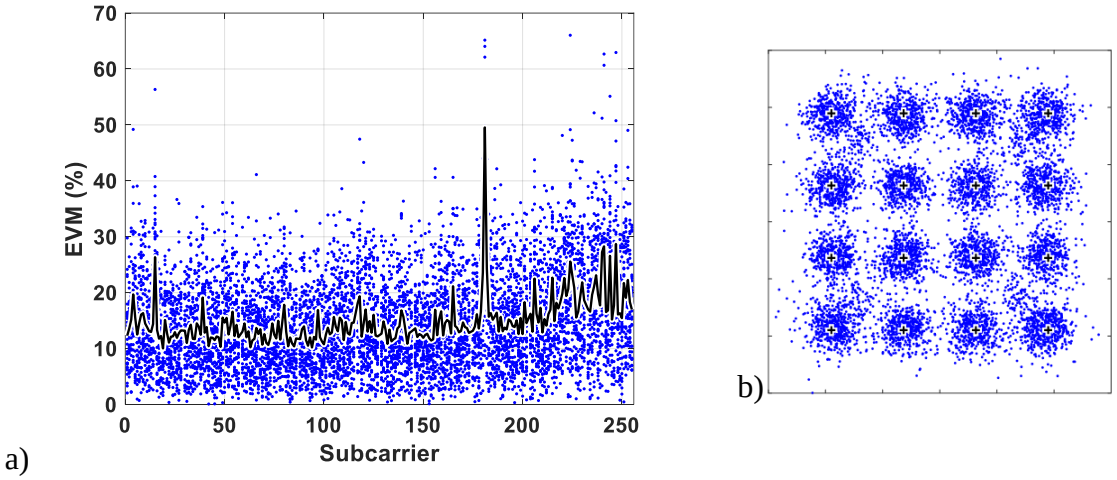

Fig. 44. 16-Gbd OFDM QPSK with net data rate of 57.8-Gbps. a) EVM for each subcarrier and b) aggregate constellation.

To achieve the highest possible data rate with OFDM, bit-loading was utilized for a 26-Gbd OFDM waveform, which yielded a net data rate of 73.532-Gbps. The EVM by subcarriers and aggregate constellations can be seen in Fig. 45. The QPSK subcarriers have an average EVM of 19.55% (corresponding to a BER of 1.558×10^{-7}) and the 16QAM subcarriers have an average EVM of 17.31% (corresponding to a BER of 3.668×10^{-3}).

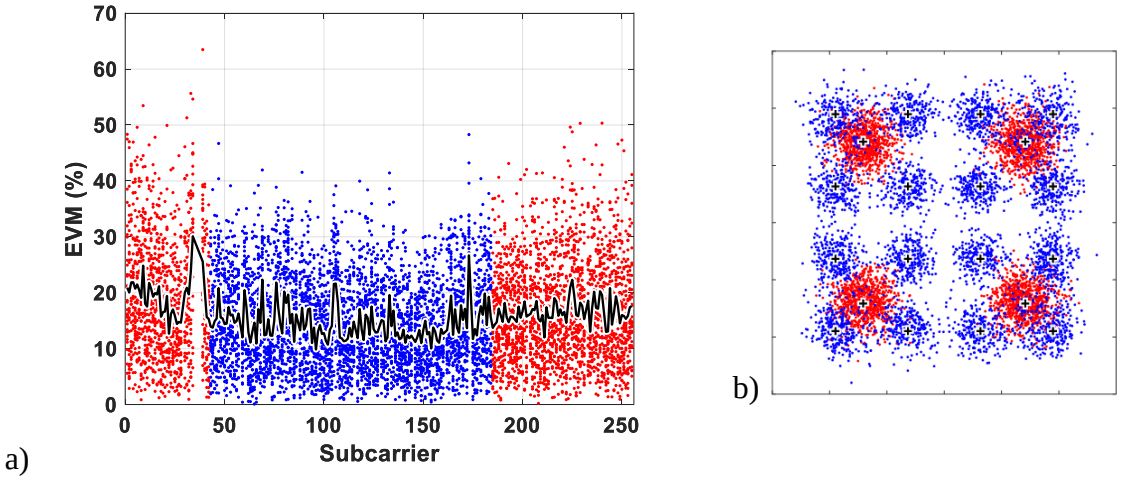

Fig. 45. 26-Gbd bit-loaded OFDM with net data rate of 73.5-Gbps. a) EVM for each subcarrier and b) aggregate constellation.

5.2.3 Discussion

Both V- and W-band transmission was demonstrated for single-polarization fiber-wireless links, both achieving ~75-Gbps using bit-loaded OFDM. Due to the structure of the architecture, dual-polarization transmission can be achieved with minor modifications. The primary limiter of these links the PD bandwidth for the V-band link and the downconversion gain of the balanced mixer in the W-band link. Improved components can enable even higher-speeds for the demonstrated links.

CHAPTER 6. OPTICAL CYCLOSTATIONARY PROCESSOR

A CSP performs signal processing to evaluate the spectral correlation function (SCF) of a received waveform. Typically, this signal processing is applied digitally due to the ease of operation, but the operations necessary for evaluating the SCF are computationally expensive, primarily for the calculation of the Fourier transform at high sample rates. Digital implementations, while relatively straightforward, are incapable of computing the SCF of wideband signals (>10GHz) at high speeds. Using optical signal processing, the digital computation load of a CSP can be reduced. This chapter presents two such optical CSPs (OCSPs) with associated experimental results.

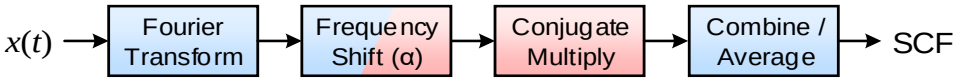

Fig. 46. General structure of a CSP. The CSP implemented in this work has blue blocks performed digitally, red performed optically, and red-blue a combination of the two.

6.1 Optical Conjugate Multiplication Theory

For the CSPs presented in this work, the primary theory to be discussed is related to the conjugate multiplication in the optical domain, there are a few primary methods of doing this.

6.1.1 Conjugate multiplication via Coherent Receiver

The most straight-forward means of conjugate multiplication using single-polarization coherent receiver, wherein two optical signals (E_1 and E_2) are inputs to the coherent receiver (Fig. 47), as opposed to a single optical signal and a single optical LO. If E_1 and E_2 signals modulated independently, but from the same optical source they can be

represented as $E_n(t) = A_n(t)e^{j\omega_0 t}$, where $A_n(t)$ is the signal modulation and ω_0 is the optical carrier angular frequency. The outputs of the 90° hybrid are thus:

$$E_{+1} = e^{j\omega_0 t}[A_1 + A_2] \tag{78}$$

$$E_{-1} = e^{j\omega_0 t}[A_1 - A_2] \tag{79}$$

$$E_{+2} = e^{j\omega_0 t}[A_1 + jA_2] \tag{80}$$

$$E_{-2} = e^{j\omega_0 t}[A_1 - jA_2] \tag{81}$$

The optical power inputs of the BPDs are then:

$$P_{+1} = |A_1|^2 + |A_2|^2 + A_1A_2^* + A_1^*A_2 \tag{82}$$

$$P_{-1} = |A_1|^2 + |A_2|^2 - A_1A_2^* - A_1^*A_2 \tag{83}$$

$$P_{+2} = |A_1|^2 + |A_2|^2 - jA_1A_2^* + jA_1^*A_2 \tag{84}$$

$$P_{-2} = |A_1|^2 + |A_2|^2 + jA_1A_2^* - jA_1^*A_2 \tag{85}$$

The BPD photocurrents are then:

$$I_1 \propto 2A_1A_2^* + 2A_1^*A_2 \tag{86}$$

$$I_2 \propto -2jA_1A_2^* + 2jA_1^*A_2 \tag{87}$$

The digitized photocurrents can then be combined in quadrature to yield the desired conjugate multiplication:

$$I_1(t) + jI_2(t) \propto 4A_1(t)A_2^*(t) \tag{88}$$

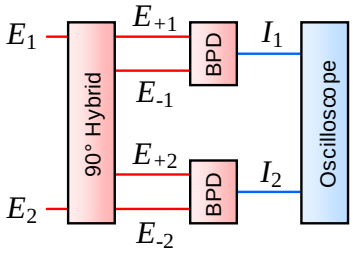

Fig. 47. Single-polarization coherent receiver with intermediate fields and current.

In the context of the CSP, this method of evaluating the conjugate multiplication requires the input fields to be related to the time-shifted Fourier transforms of the signal being investigated. Due to the flexibility of this subsystem, the Fourier transform can be implemented in either the digital or optical domain beforehand.

6.1.2 Conjugate multiplication via Cascaded ModulaTors

The second method that can used is to utilized cascaded IQ-MZMs that apply independent modulation corresponding to the independent signals. Thus, the output of the modulators will be:

$$E_{\mathrm{MZM},1}(t) = A_{\mathrm{MZM},1}(t)e^{j\omega_0 t} \tag{89}$$

$$E_{\mathrm{MZM},2}(t) = A_{\mathrm{MZM},2}(t)A_{\mathrm{MZM},1}(t-\tau)e^{j\omega_0(t-\tau)} \tag{90}$$

where τ is the time-delay between the outputs of the two cascaded modulators.

In the context of the CSP, this method of evaluating the conjugate multiplication requires that the RF inputs to the IQ-MZMs be the Fourier transforms of the signal being investigated, thus the Fourier transform must be computed in the digital domain. Because of this requirement, multiplication using cascaded modulators does not provide a roadmap for full optical CSPs.

6.1.3 Conjugate Multiplication Via Four-Wave Mixing

The third method that can be used for conjugate multiplication in the optical domain is four-wave mixing (FWM). Being a nonlinear interaction, FWM is typically considered an impairment in optical communication links, but for an optical signal processor, it is a tool that can be utilized. The field amplitudes (A_i) of four interacting waves in optical fiber can be described by coupled differential equations [106]:

$$\frac{dA_1}{dz} = j\gamma\left(-A_1|A_1|^2 + 2A_2^* A_3 A_4 e^{j\Delta kz} + 2A_1\sum_i |A_i|^2\right) \tag{91}$$

$$\frac{dA_2}{dz} = j\gamma\left(-A_2|A_2|^2 + 2A_1^* A_3 A_4 e^{j\Delta kz} + 2A_2\sum_i |A_i|^2\right) \tag{92}$$

$$\frac{dA_3}{dz} = j\gamma\left(-A_3|A_3|^2 + 2A_1 A_2 A_4^* e^{-j\Delta kz} + 2A_3\sum_i |A_i|^2\right) \tag{93}$$

$$\frac{dA_4}{dz} = j\gamma\left(-A_4|A_4|^2 + 2A_1 A_2 A_3^* e^{-j\Delta kz} + 2A_4\sum_i |A_i|^2\right) \tag{94}$$

where z is the fiber distance, γ is the fiber nonlinear coefficient, and Δk is the phase mismatch. The fiber nonlinear coefficient can be calculated as:

$$\gamma = \frac{n_2'\omega}{cA_{\text{eff}}} \tag{95}$$

where n_2' is the nonlinear refractive index and A_{eff} is the effective mode-field area. The phase mismatch can be expanded to:

$$\Delta k = \underbrace{-\beta_1 - \beta_2 + \beta_3 + \beta_4}_{\Delta k_d} + \underbrace{\gamma(P_1 + P_2 + P_3 + P_4)}_{\Delta k_{\text{NL}}} \tag{96}$$

where Δk_d is the material dispersion induced phase mismatch, Δk_{NL} is the nonlinearity induced phase mismatch, and P_i is the optical power of the ith interacting wave. The frequencies of the interacting fields must satisfy the condition: $\omega_3 + \omega_4 = \omega_1 + \omega_2$

For conjugate multiplication using FWM, let A_1 be a pump field (effectively constant), A_2 and A_3 be the modulated signals being multiplied, and A_4 be the output FWM term corresponding to the conjugate multiplication. Following Eq. 94, if A_4 is negligible compared to the other interacting amplitudes and A_4 is dominant compared to the other interacting fields, then A_4 will predominantly proportional to the multiplication of A_2 and A_3.

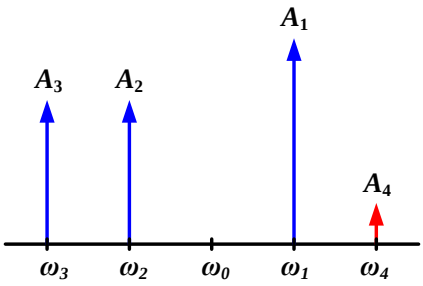

Fig. 48. Cartoon showing the interacting fields of interest when FWM.

In the context of the CSP, the inputs corresponding to the Fourier coefficients can be produced in the digital or optical domain, like conjugate multiplication using a coherent receiver. An advantage the FWM technique has over the coherent detection technique, is the multiplied signals are still in the optical domain and can be further manipulated. For example, if a higher-order spectral correlation is needed, the multiplied optical signals can be captured using a power detector such that the output photocurrent is proportional to $|A_2A_3|^2$, instead of $A_2A_3^*$.

6.2 OCSP with Direct Detection

6.2.1 Architecture and Operation

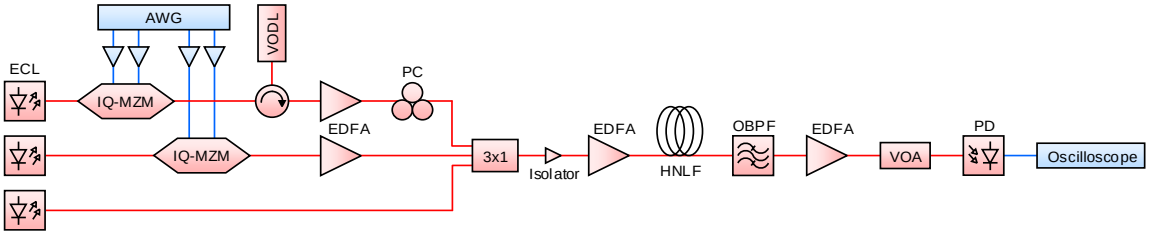

Fig. 49. Block diagram of OCSP-DD.

The first system developed was an OCSP with direct detection (OCSP-DD) that can evaluate the magnitude of the SCF, the architecture can be seen in Fig. 49. Two independent C-band external cavity lasers (ECLs), separated by about 50-GHz, are

separately modulated with I- and Q-phase signals generated by an AWG. The signals generated are time-shifted Fourier transforms of an arbitrary received waveform. In other words, the Fourier coefficients are modulated onto the optical carriers in the time-domain. One modulated signal passes through a variable optical delay line (VODL) to provide additional fine-tuning of the time-delay between the two modulated signals (on top of the time-delay implemented digitally at the AWG).

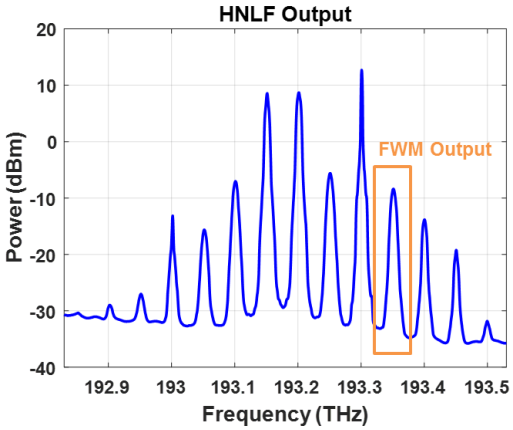

Fig. 50. Experimentally measured optical spectra at output of HNLF.

The modulated signals are amplified by EDFAs before recombination with another independent laser source. All combined signals are amplified to an aggregate optical power of 27-dBm before propagation through 200-m of highly nonlinear fiber (HNLF). Four-wave mixing (FWM) in the HNLF generates various mixing terms, with one being the conjugate multiplication of the input signals as well as not overlapping in frequency with third-order intermodulation terms. An optical demultiplexer selects the FWM term of interest (Fig. 50), which is subsequently amplified before direct detection in photodetector. Due to direct detection, the received signals are the magnitude of the cyclic spectrums squared. The electrical signal is captured by an oscilloscope with subsequent offline

processing that maps the time-domain signals to unique frequencies and cyclic frequencies of the SCF magnitude being evaluated.

6.2.2 Experimental Results

To test the functionality of the OCSP-DD, a 50-Mbd QPSK on a 50-MHz carrier was digitally generated and passed through the whole CS processor system (including DSP before and after the optical processor). The Fourier coefficients of the sample communication waveform were generated, cloned, and shifted in time; these waveforms were then generated by the AWG and passed through the rest of the optical processor. Upon digitization of the OCSP-DD output, the received waveform was averaged and mapped to the square of the SCF (Fig. 51).

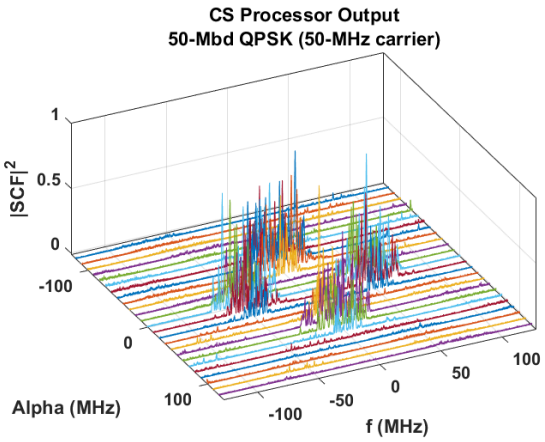

Fig. 51. CS processor output averaged and mapped to generate the square of the SCF. Input signal: 50-Mbd QPSK on a 50-MHz carrier.

6.2.3 Discussion

The OCSP-DD presented demonstrated computation of the power of the SCF using a photonic link, which enables fourth-order cyclic spectral analysis, but it is limited in that only the power can be measured. Because only the power is acquired, averaging of the received waveforms does not operate coherently and does not suppress the noise floor

relative to the cyclic spectra: this motivates the development of an updated CSP employing coherent detection.

6.3 OCSP With Coherent Detection

The OCSP with coherent detection (OCSP-CD) must be capable of capturing the magnitude and phase of the SCF, not just the power of the SCF. This requirement brings forth additional architecture considerations, namely frequency locking of the optical sources, which could be previously ignored in the OCSP-DD architecture. If phase and frequency deviation is present at the receiver, even with magnitude and phase information, there will be no processing gain due to coherent averaging of the received SCFs. The proposed OCSP-CD architecture is discussed below.

6.3.1 Architecture and Operation

6.3.1.1 Hardware Setup

A block diagram of the experimental setup is shown in Fig. 52. Frequency locked optical tones are first generated by modulating a low linewidth (<10-kHz), 1550-nm external cavity laser (ECL) by a phase modulator (PM) driven by a 45-GHz LO signal source. First and second harmonics of both upper and lower sidebands (labelled λ_{+1}, λ_{+2}, λ_{-1}, and λ_{-2}, respectively) are demultiplexed to different fibres using a wavelength selective switch (WSS). The lower sideband tones (λ_{-1}, and λ_{-2}) are amplified and subsequently modulated by two independent IQ Mach Zehnder modulators (IQ-MZMs). A 90-GS/s arbitrary waveform generator (AWG) creates the four signals that drive the MZMs. Polarization controllers (PCs) are inserted throughout the system to ensure efficient modulation and FWM.

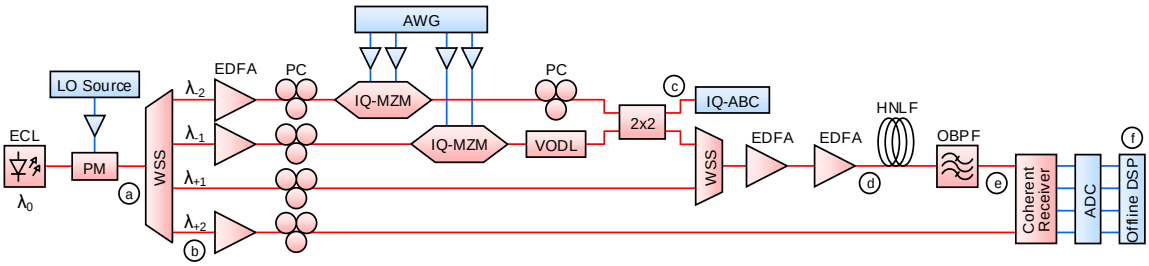

Fig. 52. Block diagram of OCSP-CD.

The two modulated signals are combined by a 3-dB coupler after one passes through a PC and the other a variable optical delay line (VODL). The VODL enables fine adjustment of the timing overlap of the optical signals. One output of the 3-dB coupler is an input to the dual-polarization, IQ, automatic bias controller (ABC), which adaptively sets the bias points of both IQ-MZMs at null. The other output of the 3-dB coupler is input to a second WSS that multiplexes the modulated signals with an unmodulated optical pump tone (λ_{+1}), while also enabling coarse gain equalization between the modulated signals.

The two optical signals and single pump tone are passed through two erbium-doped fibre amplifiers (EDFAs) before propagation through a highly nonlinear fibre (HNLF), with a γ of approximately 12.6-W^{-1}/km. FWM in the fiber generates various terms, with the term of interest located at λ_{+2} (wavelength that yields a conjugate multiplication between the two optical signals and the pump, while also being at a sufficiently distinct wavelength from the third-order intermodulation terms of the two optical signals).

A tuneable optical bandpass filter (OBPF) significantly reduces the power of the input signals and the pump laser (selecting the FWM term of interest) before detection using a coherent receiver. The LO of the coherent receiver is the λ_{+2} optical tone; due to the optical tones being generated from the same laser source, the captured waveform does not require frequency recovery. The outputs of the coherent receiver are digitized by an

oscilloscope before offline processing. Note, a coherent receiver comprised of a 90°-hybrid and two BPDs can be used because only one polarization is necessary, but such a receiver was not available for the experiment.

The bandwidth of the system is limited to the frequency spacing of the optical tones, which are constrained to ~45-GHz due to bandwidth limitations of the electronic amplifier and PM utilized. Because the system implements multiplication of waveforms in the time-domain (convolution in the frequency-domain), the maximum waveform bandwidth that can be analysed using the CSP without interference from optical tones is half the optical tone spacing: ~23-GHz.

Fig. 53 shows the spectra of the optical and electrical signal at different points in the OCSP-CD. Fig. 53.a is the spectra of the optical comb with 45-GHz spacing: the driving source was optimized for maximum tone powers, particularly for the fundamental harmonics. Fig. 53.b is the spectra of the optical comb with the comb line corresponding to the coherent receiver LO filtered out: there are additional comb lines not completely suppressed, but they are more than 25-dB below the LO and do not yield significant beating terms in the coherent receiver. Fig. 53.c is the optical spectra of the combined modulated signals with 16-Gbd QPSK modulation on both comb lines. Fig. 53.d shows the spectra of the combined and amplified waveforms containing the modulated signals and the FWM pump. Note, the second WSS provides additional suppression of the unnecessary comb lines, resulting in a spectra showing only the signals of interest and the noise floor. Fig. 53.e shows the spectra of the filtered FWM output. The spectra is broadened due to the correlation of the modulated signal spectra in the frequency domain. Additional FWM

terms are present, but they coincided in frequency with the signal and pump inputs, as well as IMD3 distortions. Fig. 53.f is the electrical spectrum of the captured signal.

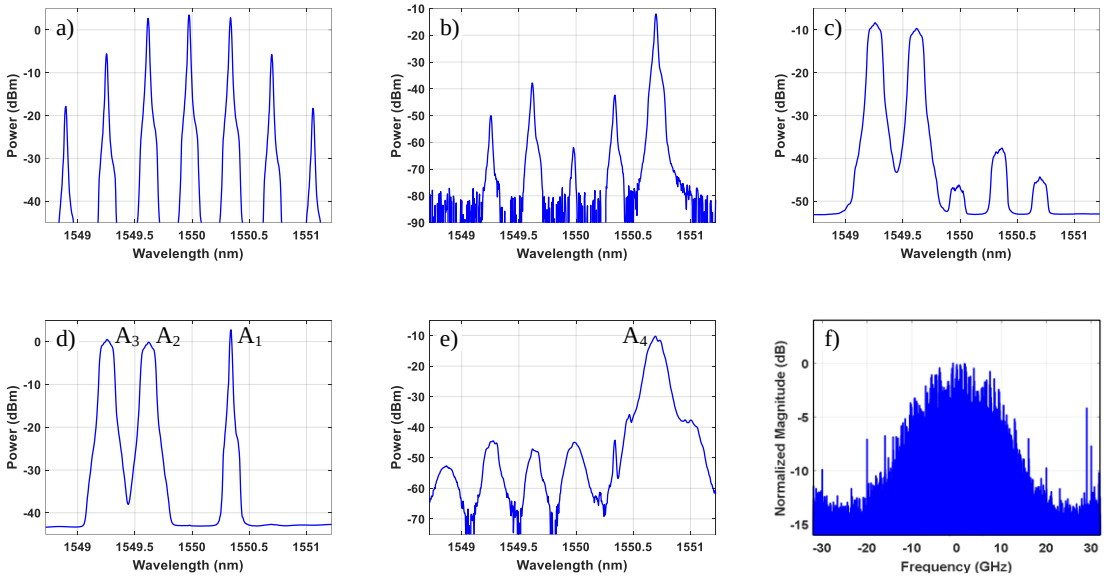

Fig. 53. Measured spectra at different locations in the OCSP-CD. a) Generated tones at output of PM, b) filter PM output used as LO for coherent detection, c) combined modulated signals, d) EDFA tap before input to HNLF, e) FWM term selected by OBPF, and f) digitized signal.

6.3.1.2 Transmitter DSP

The purpose of transmitter DSP is to create the digital waveforms generated by the AWG. An arbitrary communication waveform is created digitally and resampled to match the bandwidth of the CSP. The fast Fourier transform (FFT) of the resampled waveform is computed and two waveforms, padded with zeros, are created by shifting in time the FFT signals, corresponding to the cyclic frequency shifts. Fig. 54 shows the structure of the two signals modulated onto the optical carriers.

Headers comprised of QPSK symbols are appended to the beginning of the generated waveform streams for timing recovery (TR) and pilot tones before each FFT

window (corresponding to different cyclic frequencies) for single-tap phase equalization (EQ).

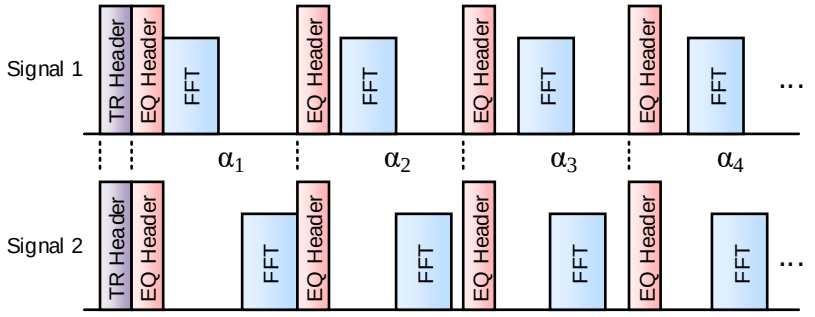

Fig. 54. Structure of signals modulated onto OCSP-CD optical carriers

6.3.1.3 Receiver DSP

The received waveform is correlated with the known result of the multiplied headers to determine the start time of the captured waveform. The channel phase offset of each FFT frame is estimated and corrected for using the EQ pilot. The samples corresponding to the cyclic spectrum are cropped and combined for the different cyclic frequencies and iterations to yield the SCF, following the FFT accumulation method [107].

6.3.2 Experimental Results

To demonstrate functionality of the optical CSP, various communication waveforms were generated digitally and passed through the complete system.

6.3.2.1 Two-Tone Signals

To measure characterize the OCSP-CD, two independent tones at unique frequencies were modulated onto the independent paths, and the mixing magnitude of the mixing frequency was measured on the oscilloscope. Frequencies were chosen such that an integer number of cycles were generated by the DAC and an integer number of cycles of the fundamental mixing term were captured by the oscilloscope: this was done to ensure

the magnitude measurements were not distorted by spectral leakage. Also, transmit frequencies were chosen such that they did not overlap with the fundamental mixing frequency (e.g. f_1 = 3-GHz, f_2 = 5GHz, f_2-f_1 = 2-GHz). Fig. 55 shows the measured magnitudes of the mixing terms over the frequencies investigated. The 3-dB point of the response is between 16- and 18-GHz.

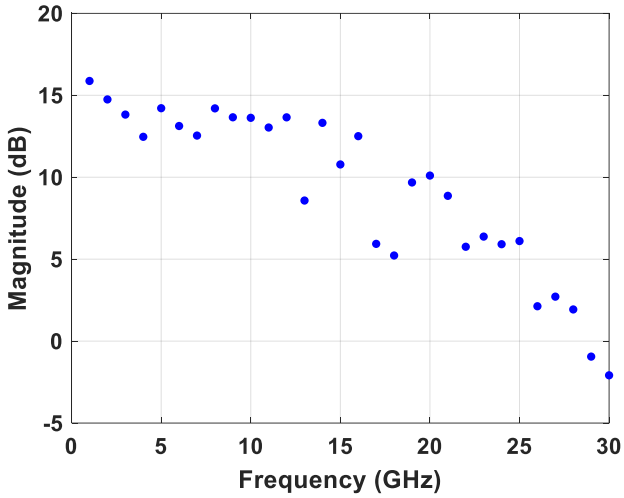

Fig. 55. Two-tone output (measuring the fundamental mixing tone)

6.3.2.2 Wideband Signalling

The practical signal used to test the performance of the OCSP-CD was a 15-Gbd 16QAM signal with RRC 0.5-roll-off pulse shaping. The SCF was evaluated with 256 frequency and cyclic frequency steps each, resulting in a frequency resolution of 0.117-GHz. For each cyclic frequency, 200 cyclic spectra were averaged.

Fig. 56, Fig. 57, and Fig. 58 show the measured cyclic spectrum of the of the wideband waveform at the zero cyclic frequency (the PSD), the baud rate, and slightly off the baud rate, respectively. Each plot displays the magnitude (left) and the phase (right) with different number of averaged waveforms ranging from 1 to 200. From the PSD and the cyclic spectrum at the baud rate, a clear SNR improvement can be seen with coherent

averaging, whereas the cyclic spectrum just off the baud rate simply exhibits a reduction in the noise floor with coherent averaging. A linear phase response can be seen in the cyclic spectrum at the baud rate with a slightly non-zero slope, which is caused by a slight imbalance in the optical powers of the FWM input signals. Though the optical powers were tuned to reduce the slope at the start of measurements, the optical powers drifted slightly over the course of capturing data. Active optical power control would provide improved phase responses.

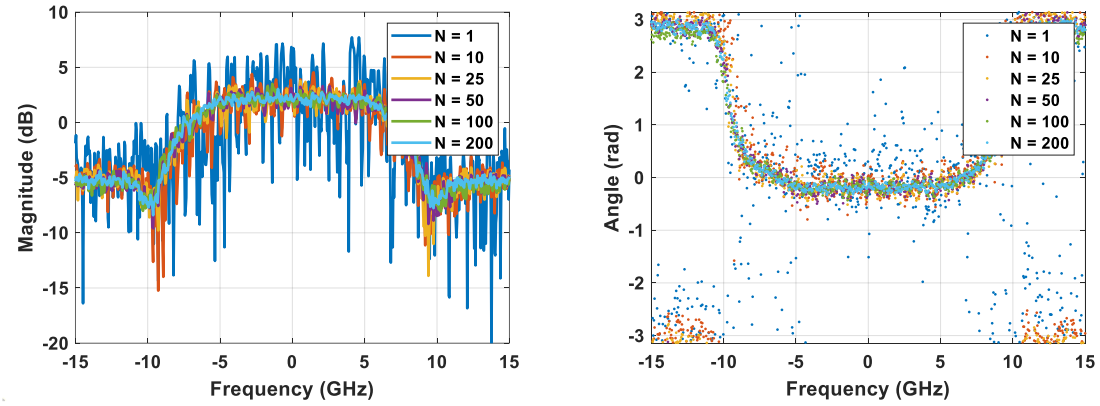

Fig. 56. Measured PSD and phase of 15Gbd 16QAM with RRC 0.5-roll-off pulse shaping, with different number of averaged waveforms

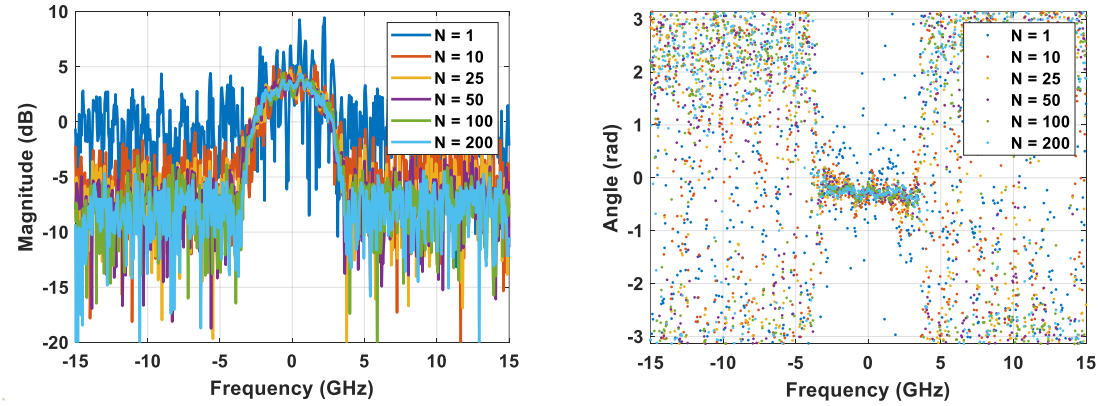

Fig. 57. Measured cyclic spectrum at the baud rate of 15Gbd 16QAM with RRC 0.5-roll-off pulse shaping, with different number of averaged waveforms

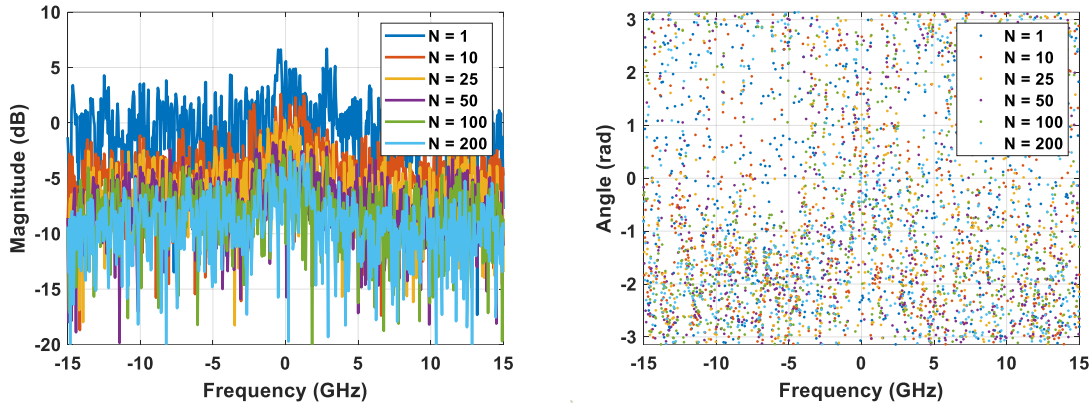

Fig. 58. Measured cyclic spectrum of 15Gbd 16QAM with RRC 0.5-roll-off pulse shaping, with different number of averaged waveforms (with cyclic frequency of 14.766-GHz)

Fig. 59 shows the complex SCF with 200 averaged waveform with the PSD and cyclic spectrum at the baud rate highlighted. The cyclic spectrum due to the communication waveform clock is clearly visible, especially amid coherent averaging, suppressing the noise at other cyclic frequencies.

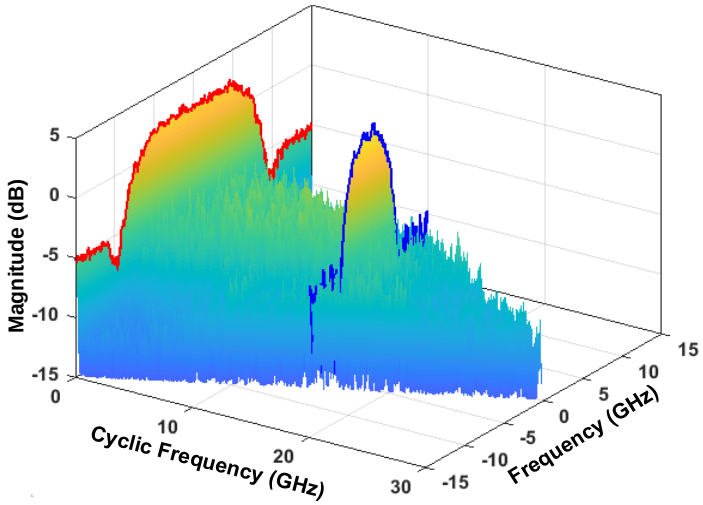

Fig. 59. Measured SCF of 15Gbd 16QAM with RRC 0.5-roll-off pulse shaping

6.3.2.3 Multiple Signals

Multiple frequency division multiplexed (FDM) waveforms were analysed simultaneously to demonstrate the abilities of discriminating signals using the SCF from

the OCSP-CD output. Table 7 lists the modulation parameters of the three signals analysed, each at different carrier frequencies with different pulse shape roll-offs and some at different baud rates. The SCF was evaluated with 256 frequency and cyclic frequency steps each, resulting in a frequency resolution of 0.117-GHz. For each cyclic frequency, 200 cyclic spectra were averaged.

Table 7 – Signal parameters for FDM 16QAM SCF evaluation

	Signal #1	Signal #2	Signal #3
Carrier Frequency (GHz)	-7.5	0	7.5
Baud Rate (Gbd)	7.5	5.625	5.625
RRC Roll-off	0.1	0.3	0.5

Fig. 60 shows the measured SCF of the FDM waveform. Solid traces highlight the PSD and the cyclic spectra evaluated at the two baud rates. The peaks in the SCF corresponding to the baud rate of the signals is clearly highlighted by the blue and purple traces. Note the spectral location of the pulses in the cyclic spectra corresponding to the carrier frequencies of the communication waveforms. Furthermore, each cyclic spectrum exhibits a different pulse width corresponding to the varying levels of roll-off factors.

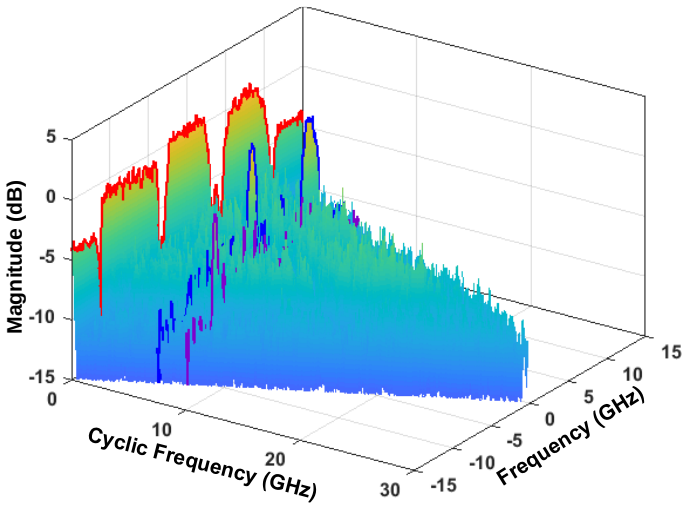

Fig. 60. Measured SCF of FDM 16QAM signals

6.3.2.4 Time-Stretching

Because a digital transmitter is already employed in the OCSP-CD to evaluate the SCF additional DSP can be used to further the capabilities of the processor. One such DSP addition is time-stretching wherein a time-scaling of the computer Fourier coefficients results in a spreading or compression of the spectra in the time-domain, increasing or decreasing the frequency resolution of the computer SCF.

To demonstrate the functionality of time-stretching using the OCSP-CD, a 5G waveform was passed through the system: some of the modulation parameters are shown in Table 8. Using a time-scaling factor of 600, sampling rate of 30-GS/s, and 256 frequency and cyclic frequency steps, the spectral resolution is 195-kHz. The measured SCF (with 200 averaged spectra) is shown in Fig. 61. Because 5G waveforms are comprised of OFDM signals, the SCF is rich in spectral content, though distinct from conventional FDM QAM (Fig. 60).

Table 8 – Signal parameters for 5G waveform SCF evaluation

Modulation Parameter	Value
Channel bandwidth	120-MHz
Number of carriers	2
Subcarrier spacing (SCS)	60-kHz
Number of resource blocks (NRB)	135

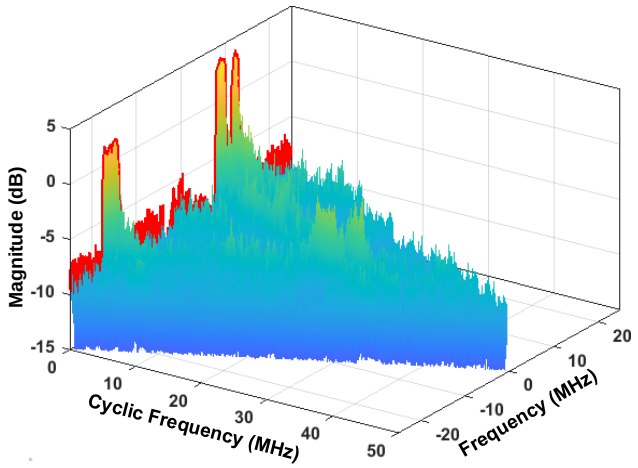

Fig. 61. Measured SCF of 5G signals with time-stretching

6.3.2.5 Baud Rate and Pulse Shape Estimation

The measured SCF from the OCSP-CD was utilized for waveform characterization, particularly baud rate estimation and pulse shape roll-off estimation. Baud rate estimation is based on the method described in Sec. 3.2.1.2 wherein a peak search is applied over all non-zero cyclic frequencies in the average SCF. Fig. 62 shows the magnitude of the SCF spanning the cyclic frequencies measured, with each point corresponding to the averaged SCF values for all measured frequencies. There is a clear peak at zero cyclic frequency corresponding to the PSD and at 15-GHz corresponding to the baud rate of the 15-Gbd

16QAM waveform investigated. The baud rate is perfectly estimated, though estimation accuracy can be reduced when finer cyclic frequency resolutions are utilized.

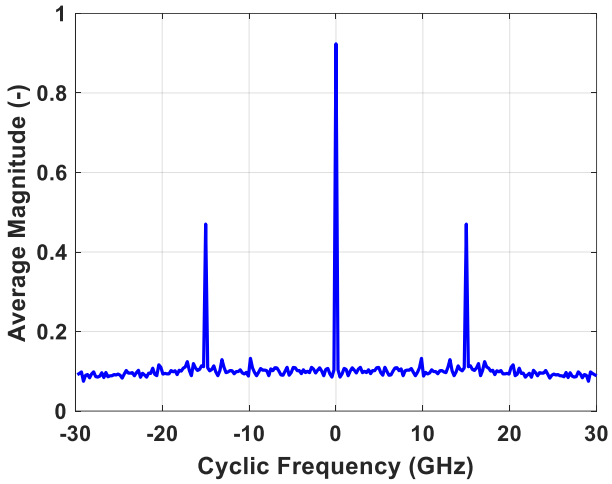

Fig. 62. Average magnitude of SCF, displaying peaks at zero cyclic frequency and baud rate cyclic frequency

Pulse shape roll-off estimation follows the method described in Sec. 3.2.1.3 wherein the magnitude of the normalized SCF is fit (via the Levenberg-Marquardt algorithm) to the theoretical cyclic spectrum of an 0.5-roll-off RRC pulse. The estimated roll-off was 0.492 resulting in an estimation error of 1.058%, which is extremely low, particularly for the purpose of accurate matched filtering of the communication waveform.

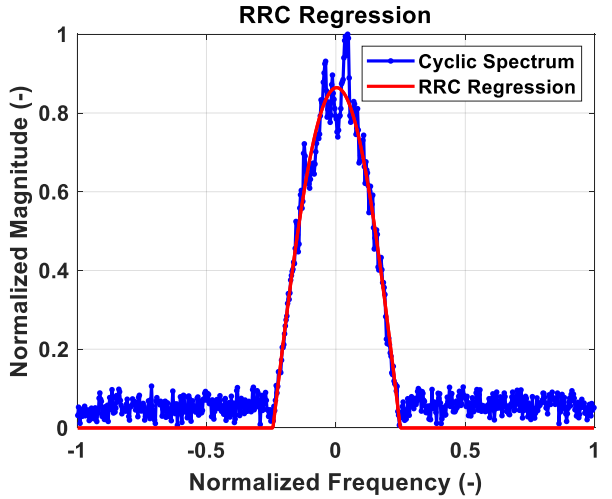

Fig. 63. RRC regression of measured cyclic spectrum

6.3.3 Discussion

The OCSP-CD architecture presented in this section demonstrated capabilities greatly surpassing of the OCSP-DD architecture, particularly with regards to coherent averaging. The system was characterized and demonstrated for a variety of communication waveforms and the output SCF was utilized for waveform characterization. It more fundamentally demonstrates a practical use for the typically non-desirable FWM in optical fiber, which enables the conjugate multiplication of signals in the optical domain.

Though the architecture demonstrated wide bandwidth capabilities, it depends on high bandwidth DSP, primarily in computing the FFT. Future OCSP architectures should be developed to further utilize the wide-bandwidth capabilities of optical components by migrating the computation of the Fourier transform out of the digital domain and into the optical domain, there are various means of doing this with the dispersive Fourier transform being a promising option [108].

CHAPTER 7. CONCLUSIONS

Two blind, single-carrier waveform classification architectures for coherent links were presented. The first architecture utilized higher-order cyclic cumulants paired with a support vector machine to discriminate between QPSK, 16QAM, and 64QAM over different fiber lengths, without the use of timing recovery, which other architectures have depended on. It demonstrated very high classification accuracy for the formats and fiber lengths investigated. The second architecture was developed to provide increased flexibility with regards to constellation shaping and non-uniform symbol distributions, which other classification implementations cannot account for accurately. The architecture uses a modified carrier phase recovery algorithm that acts on the rotational symmetry of detected constellations followed by *k*-means cluster for format classification. It demonstrated good classification accuracy over reasonable OSNRs and fiber distances, for a wide range of modulation parameter combinations (varied constellation shapes and sizes, even with time-domain hybrid modulation formats and probabilistic shaping). A method of estimating the net data rate amid probabilistic shaping was also presented with the architecture.

A blind, multi-carrier classification architecture was presented. It utilized a combination of cyclostationary processing and *k*-means clustering to estimate a variety of OFDM modulation parameters, ranging across the number of subcarriers, size of the cyclic prefix, baud rate, and preamble duty cycle. Performance of the architecture was demonstrated experimentally over a K_a-band fiber-wireless link.

High-speed fiber-wireless transmission was demonstrated experimentally across a V- and W-band channel. Modulation parameters were optimized to transmit over 70-Gbps per polarization across each channel. Bit-loaded OFDM was demonstrated for the V-band link to optimize the spectral efficiency of the transmission in the midst of a steep, photodiode roll-off limiting performance; while it was also demonstrated for the W-band link to counteract an extremely non-flat channel response and strong distortions caused by the RF electronic components.

Two optical cyclostationary processors were presented for the purpose of evaluation the spectral correlation function of wideband signals exploiting four-wave mixing for conjugate multiplication. The first architecture captured the time-domain cyclic spectrum using a direct detection receiver, resulting in the power the cyclic spectrum. The second architecture utilized frequency locked tones and coherent detection to stably capture the magnitude and phase of the cyclic spectrum, enabling coherent averaging for cyclostationary processing gain. Operation was demonstrated for a variety of communication waveforms, including high baud-rate QAM and "low" bandwidth 5G signals. Baud rate and pulse shape roll-off estimation was demonstrated using the measured cyclic spectra at the output of the OCSP-CD.

7.1 Future research topics

Due to the range of topics spanned by this dissertation there are several future research topics worth pursuing. First, though the range of modulation parameters that can be characterized by blind receiver architectures (in this dissertation and the literature), there is limited research when probabilistic shaping is employed in coherent links, and more accurate algorithms would be desirable. Also, with the rise of machine learning more

techniques should be investigated for parameter estimation without depending on conventional demodulation DSP blocks.

Second, investigations should be made to determine wireless transmission distance limitations of the V- and W-band fiber-wireless links, while also extending the architectures to dual-polarization implementations for twice the capacity.

Finally, to become a practical alternative to conventional, digital implementations, the optical cyclostationary processor must be updated to evaluate the Fourier transform in the optical domain, reducing significantly the computation in the digital domain. There are a few paths forward to do this, but the feasibility of these hardware implementations is still to be determined.

REFERENCES

[1] J. G. Proakis and M. Salehi, *Digital Communications, 5th Edition*, New York: McGraw-Hill, 2008.

[2] J. L. Holsinger, "Digital Communication Over Fixed Time-Continuous Channels with Memory – With Special Application to Telephone Channels," *MIT Res. Lab Electron.*, Technical Report 320, Oct. 1964.

[3] R. W. Chang, "Synthesis of Band-Limited Orthogonal Signals for Multichannel Data Transmission," *Bell Syst. Tech. J.*, pp. 1775-1796, Dec. 1966.

[4] J. S. Chow, J. C. Tu, J. M. Cioffi, "A Discrete Multitone Transceiver System for HDSL Applications," *IEEE Photon. Technol. Lett.*, vol. 9, no. 6, pp. 895-908, Aug. 1991.

[5] W. R. Peng, I. Morita, H. Tanaka, "Hybrid QAM Transmission Techniques for Single-Carrier Ultra-Dense WDM Systems," in *Proc. Opto-Electron. Commun. Conf.*, Kaohsiung, pp. 824-825, July 2011.

[6] F. R. Kschischang and S. Pasupathy, "Optimal Nonuniform Signaling for Gaussian Channels*," IEEE Trans. Inf. Theory*, vol. 39, no. 3, pp. 913-929, May 1993.

[7] G. Bocherer, F. Steiner, and P. Schulte, "Bandwidth Efficient and Rate-Matched Low-Density Parity-Check Coded Modulation," *IEEE Trans. Commun.*, vol. 63, no. 12, pp. 4651-4665, Dec. 2015.

[8] R. J. Essiambre, G. Kramer, P. J. Winzer, G. J. Foschini, and B. Goebel, "Capacity Limits of Optical Fiber Networks," *J. Lightw. Technol.*, vol. 28. No. 4, pp. 662-701, Feb. 2010.

[9] A. I. Abd El-Rahman and J. C. Cartledge, "Multidimensional Geometric Shaping for QAM Constellations," in *Proc. Euro. Conf. Opt. Commun.*, Gothenburg, Sep. 2017.

[10] S. Zhang, F. Yaman, E. Mateo, T. Inoue, K. Nakamura, Y. Inada, "A Generalized Pairwise Optimization for Designing Multi-Dimensional Modulation Formats," in *Proc. Opt. Fiber Commun. Conf. Exhib.*, Los Angeles, paper W4A.6, Mar. 2017.

[11] F. Jardel, T. A. Eriksson, F. Buchali, W. Idler, A. Ghazisaeidi, C. Measson, J. J. Boutros, "Experimental Comparison of 64-QAM and Combined Geometric-Probabilistic Shaped 64-QAM," in *Proc. Euro. Conf. Opt. Commun.*, Gothenburg, Sep. 2017.

[12] T. Liu, I. B. Djordjevic, T. Wang, "Optimal Signal Constellation Design for Ultra-High-Speed Optical Transport in the Presence of Phase Noise," in *Proc. Conf. Lasers Electro-Opt.*, San Jose, paper STu3J.7, June 2014.

[13] S. Varughese, V. A. Thomas, P. Isautier, J. Langston, M. Alfiad, S. Tibuleac, S. E. Ralph, "ENoB Requirements for Non-Square 64-QAM," in *Proc. IEEE Photon. Conf.,* Waikoloa, paper MB1.4, Oct. 2016.

[14] R. Ramaswami, K. N. Sivarajan, and G. H. Sasaki, *Optical Networks: A Practical Perspective, 3rd Edition*, Burlington: Morgan Kaufmann, 2010.

[15] P. J. Winzer, D. T. Neilson, and A. R. Chraplyvy, "Fiber-optic transmission and networking: the previous 20 and the next 20 years [Invited]," *Opt. Express*, vol. 26, no. 18, pp. 24190-24239, Sep. 2018.

[16] X. Chen, S. Chandrasekhar, G. Raybon, S. Olsson, J. Cho, A. Adamiecki, and P. Winzer, "Generation and Intradyne Detection of Single-Wavelength 1.61-Tb/s Using an All-Electronic Digital Band Interleaved Transmitter," in *Proc. Opt. Fiber Commun. Conf. Exhib.*, San Diego, paper Th4C.1, pp. 1-3, Mar. 2018.

[17] K. Schuh, F. Buchali, W. Idler, T. A. Eriksson, L. Schmalen, W. Templ, L. Altenhain, U. Dümler, R. Schmidl, M. Möller, and K. Engenhardt, "Single Carrier 1.2 Tbit/s Transmission over 300 km with PM-64 QAM at 100 GBaud," in *Proc. Opt. Fiber Commun. Conf. Exhib.*, Los Angeles, paper Th5B.5, pp. 1-3, Mar. 2017.

[18] X. Li, X. Xiao, Y. Xu, K. Wang, L. Zhao, J. Xiao, and J. Yu, "Real-Time Demonstration of over 20Gbps V- and W-Band Wireless Transmission Capacity in on OFDM-RoF System," in *Proc. Opt. Fiber Commun. Conf. Exhib.*, Los Angeles, paper M3E.3, pp. 1-3, Mar. 2017.

[19] S.-C. Chiang, C.-H. Li, C.-T. Lin, H.-T. Huang, C.-H. Lin, and B.-J. Lin, "V-band Gapless OFDM RoF System with Power Detector Down-conversion and Novel Volterra Nonlinear Compensation," in *Proc. Opt. Fiber Commun. Conf. Exhib.*, Anaheim, paper W1G.6, pp. 1-3, Mar. 2016.

[20] X. Li, Y. Xu, and J. Yu, "Over 100-Gb/s V-Band Single-Carrier PDM-64QAM Fiber-Wireless-Integration System," *IEEE Photon. J.*, vol. 8, no. 5, pp. 7906907, Oct. 2016.

[21] M. Jenkins, E. Soto, and R. DeSalvo, "144 Gb/s Dual-Polarization Photonic Wireless Link Operating in the V-Band," in *Proc. IEEE Photon. Conf.,* Orlando, pp. 149-150, Oct. 2017.

[22] S. Haykin, "Signal Processing: where physics and mathematics meet," in *IEEE Signal Process.*, vol. 18, no. 4, pp. 6-7, Jul. 2001.

[23] J. A. Buck, *Fundamentals of Fiber Optics*, Hoboken: Wiley, 2004.

[24] J. Zhang, J. Yu, N. Chi, Z. Dong, X. Li, and G. K. Chang, "Multichannel 120-Gb/s Data Transmission Over 2 × 2 MIMO Fiber-Wireless Link at W-Band," *IEEE Photon. Technol. Lett.*, vol. 25, no. 8, pp. 780-783, Apr. 2013.

[25] X. Li, J. Yu, J. Zhang, F. Li and J. Xiao, "Antenna polarization diversity for 146Gb/s polarization multiplexing QPSK wireless signal delivery at W-band," in *Proc. Opt. Fiber Commun. Conf. Exhib.*, San Francisco, pp. 1-3, Mar. 2014.

[26] J. Yu, X. Li, J. Zhang, J. Xiao, "432-Gb/s PDM-16QAM Signal Wireless Delivery at W-band Using Optical and Antenna Polarization Multiplexing," in *Proc. Euro. Conf. Opt. Commun.*, Cannes, pp. 1-3, Sept. 2014.

[27] F. Li, X. Li, J. Zhang, J. Yu, and Z. Cao, "Fiber-Wirless-Fiber Link for DFT-Spread OFDM Signal Transmission at W-band," *IEEE Photon. Technol. Lett.*, vol. 23, no. 12, pp. 1273-1276, June 2015.

[28] G. New, *Introduction to Nonlinear Optics*, Cambridge: Cambridge, 2011.

[29] L. F. Mollenauer, R. H. Stolen, and J. P. Gordon, "Experimental Observation of Picosecond Pulse Narrowing and Solitons in Optical Fibre," *Phys. Rev. Lett.*, vol. 45, no. 13, p. 1085, Sep. 1980.

[30] K. Kikuchi, "Characterization of semiconductor-laser phase noise and estimation of bit-error rate performance with low-speed offline digital coherent receivers," *Opt. Exp.*, vol. 20, no. 5, pp. 5291-5302, Feb. 2012.

[31] "IEEE standard for terminology and test methods of digital-to-analog converter devices," IEEE Std. 1658-2011.

[32] C. R. S. Fludger, T. Duthel, D. V. D. Borne, C. Schulien, E. D. Schmidt, T. Wulth, J. Geyer, E. D. Man, G. D. Khoe, H. D. Waardt, "Coherent Equalization and POLMUX-RZ-DQPSK for Robust 100-GE Transmission," *J. Lightw. Technol.*, vol. 26, no. 1, pp. 64-72, Jan. 2008.

[33] I. Fatadin, D. Ives, and S. J. Savory, "Blind Equalization and Carrier Phase Recovery in a 16-QAM Optical Coherent System," *J. Lightw. Technol.*, vol. 27, no. 15, pp. 3042-3049, Aug. 2009.

[34] A. M. Vengsarkar, "Dispersion compensating fibers," in *Proc. Opt. Fiber Commun. Conf. Exhib.*, Dallas, paper ThA2, pp. 233-234, Feb. 1997.

[35] M. G. Taylor, "Coherent Detection Method Using DSP for Demodulation of Signal and Subsequent Equalization of Propagation Impairments," *IEEE Photon. Technol. Lett.*, vol. 16, no. 2, Feb. 2004.

[36] S. J. Savory, "Digital filters for coherent optical receivers," *Opt. Express*, vol. 16, no. 2, pp. 804-817, Jan. 2008.

[37] R. Kudo, T. Kobayashi, K. Ishihara, Y. Takatori, A. Sano, Y. Miyamoto, "Coherent Optical Single Carrier Transmission Using Overlap Frequency Domain Equalization for Long-Haul Optical Systems," *J. Lightw. Technol.*, vol. 27, no. 16, pp. 3721-3728, Aug. 2009.

[38] F. N. Hauske, C. Xie, C. Li, L. Li, and Q. Xiong, "Frequency Domain Chromatic Dispersion Estimation," in *Proc. OFC 2010*, paper JThA11, Mar. 2010.

[39] F. N. Hauske, Z. Zhang, C. Li, C. Xie, and Q. Xiong, "Precise, Robust and Least Complexity CD estimation," in *Proc. OFC 2011*, paper JWA32, Mar. 2011.

[40] D. Wang, C. Lu, A. P. T. Lau, and S. He, "Adaptive Chromatic Dispersion Compensation for Coherent Communication Systems Using Delay-Tap Sampling Technique," in *IEEE Photon. Technol. Lett.*, vol. 23, no. 4, Jul. 2011.

[41] J. C. M. Diniz, S. M. Ranzini, V. B. Ribeiro, E. C. Magalhaes, E. S. Rosa, V. E. S. Parahyba, L. V. Franz, E. E. Ferreira, and J. C. R. F. Oliveira, "Hardware-Efficient Chromatic Dispersion Estimator based on Parallel Gardner Timing Error Detector," in *Proc. OFC 2013*, paper OTh3C.6, Mar. 2013.

[42] F. N. Hauske, M. Kuschnerov, B. Spinnler, and B. Lankle, "Optical Performance Monitoring in Digital Coherent Receivers," in *J. Lightw. Technol.*, vol. 27, no. 16, pp. 3623-3631, Aug. 2009.

[43] M. Oerder and H. Meyr, "Digital Filter and Square Timing Recovery," *IEEE Trans. Commun.*, vol. 36, no. 5, pp. 605-612, May 1988.

[44] F. M. Gardner, "A BPSK/QPSK Timing-Error Detector for Sampled Receivers," *IEEE Trans. on Commun.*, vol. COM-34, no. 5, pp. 423-429, May 1986.

[45] S. Tsukamoto, Y. Ischikawa, and K. Kikuchi, "Optical Homodyne Receiver Comprising Phase and Polarization Diversities with Digital Signal Processing," in *Proc. Euro. Conf. Opt. Commun.*, Cannes, Sep. 2006.

[46] D. N. Godard, "Self-Recovering Equalization and Carrier Tracking in Two-Dimensional Data Communication Systems," *IEEE Trans. Commun.*, vol. 28, no. 11, pp. 1867-1875, Nov. 1980.

[47] S. J. Savory, V. Mikhailov, R. I. Killey, and P. Bayvel, "Digital Coherent Receivers for Uncompensated 42.8Gbit/s Transmission over High PMD Fibre," in *Proc. Euro. Conf. Opt. Commun.*, Berlin, Sep. 2007.

[48] C. Yuxin, H. Guijun, Y. Li, Z. Ling, L. Li, "Mode demultiplexing based on multimodulus blind equalization algorithm," *Opt. Commun.*, vol. 324, pp. 311-317, Apr. 2014.

[49] K. Kikuchi, "Performance analyses of polarization demultiplexing based on constant-modulus algorithm in digital coherent optical receivers," *Opt. Exp.*, vol. 19, no. 10, pp. 9868-9880, May 2011.

[50] L. Liu et al., "Initial Tap Setup of Constant Modulus Algorithm for Polarization Demultiplexing in Optical Coherent Receivers," in *Proc. OFC 2009*, paper OMT2, 2009.

[51] C. Xie and S. Chandrasekhar, "Two-Stage Constant Modulus Algorithm Equalizer for Singularity Free Operation and Optical Performance Monitoring in Optical Coherent Receiver," in *Proc. OFC 2010*, paper OMK3, Mar. 2010.

[52] H. Zhang et al., "Polarization Demultiplexing Based on Independent Component Analysis in Optical Coherent Receivers," in *Proc. ECOC 2008*, paper Mo.3.D.5, Sep. 2008.

[53] X. Xie et al., "Polarization Demultiplexing by Independent Component Analysis," *IEEE Photon. Technol. Lett.*, vol. 22, no. 11, pp. 805-807, Jun. 2010.

[54] P. Johannisson, H. Wymeersch, M. Sjodin, A. S. Tan, E. Agrell, P. A. Andrekson, and M. Karlsson, "Convergence Comparison of the CMA and ICA for Blind Polarization Demultiplexing," *J. Opt. Commun. Netw.*, vol. 3, no. 6, pp. 493-501, May 2011.

[55] B. Szafraniec et al., "Polarization demultiplexing in Stokes space," *Opt. Exp.*, vol. 18, no. 17, pp. 17928-17939, Aug. 2010.

[56] N. J. Muga and A. N. Pinto, "Adaptive 3-D Stokes Space-Based Polarization Demultiplexing Algorithm," *J. Lightw. Technol.*, vol. 32, no. 19, pp. 3290-3298, Oct. 2014.

[57] M. Visintin et al., "Adaptive Digital Equalization in Optical Coherent Receivers With Stokes-Space Update Algorithm," *J. Lightw. Technol.*, vol. 32, no. 24, pp. 4759-4767, Dec. 2014.

[58] R. Noe, "Phase Noise-Tolerant Synchronous QPSK/BPSK Baseband-Type Intradyne Receiver Concept With Feedforward Carrier Recovery," *J. Lightw. Technol.*, vol. 23, no. 2, pp. 802-808, Feb. 2005.

[59] A. J. Viterbi and A. M. Viterbi, "Nonlinear Estimation of PSK-Modulated Carrier Phase with Application to Burst Digital Transmission," *IEEE Trans. Inf. Theory*, vol. 29, no. 4, pp. 543-551, Jul. 1983.

[60] G. Picchi and G. Prati, "Blind Equalization and Carrier Recovery Using a "Stop-and-Go" Decision-Directed Algorithm," *IEEE Trans. Commun.*, vol. 35, no. 9, pp. 877-887, Sep. 1987.

[61] A. Tarighat, R. C. J. Hsu, A. H. Sayed, and B. Jalali, "Digital Adaptive Phase Noise Reduction in Coherent Optical Link," in *J. Lightw. Technol.*, vol. 24, no. 3, pp. 1269-1276, Mar. 2006.

[62] B. Widrow, J. McCool, and M. Ball, "The Complex LMS Algorithm," *Proc. IEEE*, vol. 63, no. 4, pp. 719-720, Apr. 1975.

[63] F. N. Khan, K. Zhong, X. Zhou, W. H. Al-Arashi, C. Yu, C. Lu, and A. P. T. Lau, "Joint OSNR monitoring and modulation format identification in digital coherent

receivers using deep neural networks," *Opt. Express*, vol. 25, no. 15, pp. 17767-17776, Jul. 2017.

[64] R. Borkowski, D. Zibar, A. Caballero, V. Arlunno, and I. T. Monroy, "Stokes Space-Based Optical Modulation Format Recognition for Digital Coherent Receivers," *IEEE Photon. Technol. Lett.*, vol. 25, no. 21, pp. 2129-2132, Nov. 2013.

[65] P. Isautier, J. Pan, R. DeSalvo, and S. E. Ralph, "Stokes Space-Based Modulation Format Recognition for Autonomous Optical Receivers," *J. Lightw. Technol.*, vol. 33, no. 24, pp. 5157-5163, Dec. 2015.

[66] M. Hao, L. Yan, A. Yi, L. Jiang, Y. Pan, W. Pan, and B. Luo, "Stokes Space Modulation Format Identification for Optical Signals Using Probabilistic Neural Network," *IEEE Photon. J.*, vol. 10, no. 3, Jun. 2018.

[67] A. Al-Habashna, O. A. Dobre, R. Venkatesan, and D. C. Popescu, "Second-Order Cyclostationarity of Mobile WiMAX and LTE OFDM Signals and Application to Spectrum Awareness in Cognitive Radio Systems," *IEEE J. Sel. Topics Signal Process.*, vol. 6, no. 1, pp. 26-42, Feb. 2012.

[68] Z. Sun, R. Liu, and W. Wang, "Joint time-frequency domain cyclostationarity-based approach to blind estimation of OFDM transmission parameters," *EURASIP J. Wireless Commun. Netw.*, vol. 117, 2013.

[69] P. Isautier, J. Langston, J. Pan, S. E. Ralph, "Agnostic software-defined coherent optical receiver performing time-domain hybrid modulation format recognition," in *Proc. Opt. Fiber Commun. Conf. Exhib.*, Los Angeles, paper Th2A.21, Mar. 2015.

[70] M. Xiang, Q. Zhuge, M. Qiu, X. Zhou, F. Zhang, M. Tang, D. Liu, S. Fu, D. V. Plant, "Modulation format identification aided hitless flexible coherent transceiver," *Opt. Express*, vol. 24, no. 14, pp. 15642-15655, July 2016.

[71] W. A. Gardner, "The Spectral Correlation Theory of Cyclostationary Time-Series," *Signal Process.*, vol. 11, issue 1, pp. 13-36, July 1986.

[72] A. Napolitano, "Cyclostationarity: New Trends and applications," *Elsevier B.V. Signal Process.*, vol. 120, pp. 385-408, Sep. 2015.

[73] A. V. Dandawate and G. B. Giannakis, "Statistical tests for presence of cyclostationarity," *IEEE Trans. Signal Process.*, vol. 42, no. 9, pp. 2355-2369, Sept. 1994.

[74] D. J. Esman, V. Ataie, B. P. Kuo, E. Temprana, N. Alic and S. Radic, "Comb-Assisted Cyclostationary Analysis of Wideband RF Signals," *J. Lightw. Technol.*, vol. 35, no. 17, pp. 3705-3712, Sept. 2017.

[75] F. Shalihah, A. Mitchell, and L. Bui, “Optical Correlation Using Four Wave Mixing in a Highly Nonlinear Fibre for Real-Time Serialized Ultrafast Systems,” *Int. J. Electron. Telecommun.*, vol. 59, no. 3, pp. 207-212, Aug. 2013.

[76] B. M. Sadler, “Acousto-optic cyclostationary signal processing,” *Appl. Opt.*, vol. 34, no. 23, pp. 5091-5099, 1995.

[77] M. Ionescu, M. Sato, and B. Thomsen, “Cyclostationarity-based joint monitoring of symbol-rate, frequency offset, CD and OSNR for Nyquist WDM superchannels,” *Opt. Express*, vol. 23, no. 20, pp. 25762-25772, Sep. 2015.

[78] L. Mazet and P. Loubaton, "Cyclic correlation based symbol rate estimation," in *Proc. Asilomar Conf. Signals Syst. Comput.*, Pacific Grove, vol. 2, pp. 1008-1012, Oct. 1999.

[79] R. A. Soriano, F. B. Hauske, N. G. Gonzalez, Z. Zhang, Y. Ye, and I. T. Monroy, “Chromatic Dispersion Estimation in Digital Coherent Receivers,” in *J. Lightw. Technol.*, vol. 29, no. 11, pp. 1627-1637, Jun. 2011.

[80] B. Hui, X. Tang, N. Gau, W. Zhang, and X. Zhang, “High order modulation format identification based on compressed sensing in optical fiber communication system: in *Chinese Opt. Lett.*, vol. 14, no. 11, pp. 110602-1-110602-5, Nov. 2016.

[81] V. D. Orlic and M. L. Dukic, “Automatic Modulation Classification: Sixth-order Cumulant Features as a Solution for Real-world Challenges,” in *Proc. TELFOR 2012*, Belgrade, Serbia, pp. 392-399, Nov. 2012.

[82] “The Future of Coherent Optical Networking,” Ciena, White Paper, 2019. [Online]. Available: https://media.ciena.com/documents/The-Future-of-Coherent-Optical-Networking-Vision-WP.pdf

[83] “Technology Options for 400G Implementation,” OIF, Implementation Agreement, 2015. [Online]. Available: https://www.oiforum.com/wp-content/uploads/2019/01/OIF-Tech-Options-400G-01.0-2.pdf

[84] F. Rosenblatt, *Principles of neurodynamics. perceptrons and theory of brain mechanisms*. no. VG-1196-G-8. Cornell Aeronautical Lab Inc., Buffalo, 1961.

[85] T. Calinski and J. Harabasz, “A dendrite method for cluster analysis,” in *Commun. Stat.*, vol. 3, no. 1, pp. 1-27, Jan. 1974.

[86] G. D. Forney Jr., R. G. Gallager, G. R. Lang, F. M. Longstaff, S. U. Qureshi, “Efficient Modulation for Band-Limited Channels,” in *IEEE J. Sel. Areas Commun.*, vol. 2, no. 5, Sep. 1984.

[87] J. MacQueen, “Some methods for classification and analysis of multivariate observations,” in *Proc. 5th Berkeley Symp. Math. Stat. Prob.,* Univ. of California Press, vol. 1, pp. 281-297, 1967.

[88] A. P. Dempster, N. M. Laird, D. B. Rubin, “Maximum Likelihood form Incomplete Data via the EM Algorithm,” in *J. Royal Stat. Soc., Series B,* vol. 39, no. 1, pp. 1-38, 1977.

[89] T. M. Cover and J. A. Thomas, *Elements of Information Theory,* 2nd ed. Hoboken: Wiley, 2006.

[90] H. Yang, L. Zhu, and T. Wu, “The effects of mismatched roll-off factor on the receiving performance of QAM signals,” in *Proc. Int. Conf. Commun., Circuits, Syst.*, Milpitas, CA, pp. 86-90, Jul. 2009.

[91] D. D. Falconer, “Adaptive Equalization of Channel Nonlinearities in QAM Data Transmission Systems,” in *Bell Syst. Tech. J.,* vol. 57, no. 7, pp. 2589-2611, Sep. 1978.

[92] A. Napoli, M. M. Mezghanni, D. Rafique, V. A. J. M. Sleiffer, B. Spinnler, and M. Bohn, “Novel digital pre-distortion techniques for low-extinction ratio Mach-Zehnder modulators,” in *Proc. OFC 2015*, paper Th3G.1, Mar. 2015.

[93] N. Kikuchi, R. Hirai, and Y. Wakayama, “High-Speed Optical 64QAM Signal Generation Using InP-based Semiconductor IQ Modulator,” in *Proc. OFC 2014*, paper M2A.2, Mar. 2014.

[94] T. Inoue and S. Namiki, “Adaptive adjustment of reference constellation for demodulating 16QAM signal with intrinsic distortion due to imperfect modulation,” in *Opt. Exp.*, vol. 21, no. 24, pp. 29120-29128, Nov. 2013.

[95] E. Ip and J. M. Kahn, “Compensation of Dispersion and Nonlinear Impairments Using Digital Backpropagation,” in *J. Lightw. Technol.,* vol. 26, no. 20, pp. 3416-3425, Oct. 2008.

[96] F. P. Guiomar, J. D. Reis, A. L. Teixeira, and A. N. Pinto, “Digital Postcompensation Using Volterra Series Transfer Function,” in *IEEE Photon. Technol. Lett.,* vol. 23, no. 19, pp. 1412-1414, Oct. 2011.

[97] K. Levenberg, “A Method for the Solution of Certain Non-Linear Problems in Least Squares,” *Quart. Appl. Math.*, vol. 2, no. 2, pp. 164-168, 1944.

[98] H. Adbi and L. J. Williams, “Principal component analysis,” *John Wiley & Sons*, vol. 2, pp. 433-459, July 2010.

[99] H. Hotelling, “Analysis of a Complex of Statistical Variables into Principal Components,” *J. Educ. Psychol.*, vol. 24, issue 7, pp. 498-520, Sept. 1933.

[100] J. Langston, M. D. Merrit, A. J. Stark, R. DeSalvo and S. E. Ralph, "Cyclostationarity-based classification of OFDM waveforms over photonic-assisted wireless links," in *Proc. IEEE Avionics Veh. Fiber-Opt. Photon. Conf.*, Long Beach, pp. 199-200, 2016.

[101] J. Johnson, “Four-wave mixing in O-band for 100G EPON,” *IEEE802.3ca*, Jul. 2016.

[102] V. Hegde, C. Radhakrishnan, D. Krusienski, and W. K. Jenkins, “Series-Cascade Nonlinear Adaptive Filters,” in *Proc. MWSCAS*, vol. 3, pp. 219-222, 2002.

[103] F. Schaich and T. Wild, “Waveform contenders for 5G – OFDM vs. FBMC vs. UFMC,” in *Proc. 2014 6th Int. Symp. Commun. Control and Signal Process.*, Athens, May 2014.

[104] S. Hughes, J. Langston, R. DeSalvo, C. Middleton, E. Grafer, S. E. Ralph, and A. J. Stark, "Agile micro- and millimeter-wave communication using photonic frequency conversion," in *Proc. Opt. Fiber Commun. Conf. Exhib.*, Anaheim, Mar. 2016.

[105] P. Isautier and S. E. Ralph, “Autonomous Identification and Detection for Multi-Gigabit Photonic Assisted Wireless Links,” in *Proc. 2015 Int. Topical MWP*, Paphos, Oct. 2015.

[106] G. Agrawal, *Nonlinear Fiber Optics, 5th edition*, Oxford: Academic Press, 2013.

[107] R. S. Roberts, W. A. Brown, and H. H. Loomis, “Computationally Efficient Algorithms for Cyclic Spectral Analysis,” in *IEEE SP Magazine*, vol. 8, no. 2, pp. 38-49, Apr. 1991.

[108] C. Wang, “Dispersive Fourier Transformation for Versatile Microwave Photonics Applications,” in *Photonics*, vol. 1, pp. 586-612, Dec. 2014.